DESIGN AND SYNTHESIS OF ENZYME-MOF (METAL-ORGANIC FRAMEWORK) COMPOSITES FOR LONG-PERSISTENT BIOMEDICAL APPLICATIONS

A Dissertation

by

XIZHEN LIAN

Submitted to the Office of Graduate and Professional Studies of

Texas A&M University

in partial fulfilment of the requirements for the degree of

DOCTOR OF PHILOSOPHY

Chair of Committee,	Hong-Cai Zhou
Committee Members,	Lei Fang
	Oleg Ozerov
	Sreeram Vaddiraju
Head of Department,	Simon W. North

August 2018

Major Subject: Chemistry

ABSTRACT

Metal-organic framework (MOF) is a type of emerging porous material that demonstrates promising potentials in energy, sensing, conversion, separation, and more recently, enzyme encapsulation. However, the research of enzyme-MOF composites mainly focuses on the synthetic strategy, and practical applications of enzyme-MOF composites have yet been mentioned in the literature. In this dissertation, the performance of enzyme-MOF composites in biomedical applications will be discussed in detail.

The chemical stability of MOFs in aqueous solutions is a prerequisite for enzyme immobilization. Bearing this in mind, a novel reductive labilization strategy for the preparation of an ultrastable Cr(III)-MOF from Fe(III)-MOF is discovered, which might be useful for the improvement of material stability in aqueous media. The resulting Cr(III)-MOF shows much broader pH tolerance in aqueous solutions and can be used to incorporate polyethylenimine (PEI) for carbon dioxide capture.

Most of the current enzyme-MOF composites only carry single enzymatic function, while multi-enzyme immobilized materials may be superior in complex systems. To achieve this goal, a novel mesoporous MOF, PCN-888, is rationally designed to accommodate two enzymes, glucose oxidase (GOx) and horseradish peroxidase (HRP), *via* a stepwise encapsulation manner. This bienzymatic MOF nanoreactor persists enzymatic activities very well and is resistant to trypsin digestion.

Based on the above-mentioned stepwise encapsulation strategy, a nanoscale bienzymatic nanofactory is prepared based on PCN-333. This nanofactory can be endocytosed by living cells, accumulated in lysosomes, and exert protective effect to cells against oxidative damage. More importantly, because of the preservation of enzyme

structure and function by the MOF material, the enzymatic activity of enzyme-MOF nanofactory can last as long as one week after the nanofactory is internalized.

Inspired by the long-lasting performances of enzyme-PCN-333 nanofactory, a therapeutic enzyme-PCN-333 nanoreactor is developed to activate a nontoxic prodrug in cancer cells. In this case, tyrosinase (TYR) is encapsulated and can convert innocent paracetamol to cytotoxic *o*-quinone species in cancer cells. This prodrug activation process can effectively kill multiple types of cancer cells, including a drug resistant cell line. The effectiveness of this strategy is further proved on *in vivo* models bearing human tumor xenograft.

DEDICATION

To my beloved family for their continuous support

To all my friends who helped me during my study in the U.S.

ACKNOWLEDGEMENTS

I would like to express my appreciation to my committee chair Dr. Hong-Cai Zhou, and my committee members, Drs. Lei Fang, Oleg Ozerov and Sreeram Vaddiraju for their supports throughout the past five years. Special thanks to my collaborator, Dr. Jean-Philippe Pellois, for introducing me into the fantastic research world of cell biology.

I would like to acknowledge the Zhou group members from the past and present. Special thanks to Drs. Dawei Feng, Tian-Fu Liu, Xuan Wang, Yu Fang, and Yanyan Huang for their mentorship and professional suggestions. I would also like to acknowledge the Pellois group members, especially Drs. Alfredo Erazo-Oliveras, Ting-Yi Wang and Kristina Najjar, Mrs. Dakota Brock and Jason Allen, and Ms. Helena Kondow for their help in cell biology techniques and fruitful discussion.

I want to express my greatest appreciation to my parents, my wife and my parents-in-law for their support and endless love. They have encouraged me a lot when I was facing obstacles.

CONTRIBUTORS AND FUNDING SOURCES

Contributors

This work was supported by a dissertation committee consisting of Professor Hong-Cai Zhou, Lei Fang and Oleg Ozerov of the Department of Chemistry and Professor Sreeram Vaddiraju of the Department of Mechanical Engineering.

The in vivo experiment and data analysis in Chapter V was conducted in part by Yuanyuan Zhu of the Key Laboratory of Analytical Chemistry for Living Biosystems, Institute of Chemistry, Chinese Academy of Sciences, and was published in 2018 in an article listed in the appendix.

All other work conducted for the dissertation was completed by the student independently.

Funding Sources

Graduate study was supported by a scholarship from Dow Chemical Company. This work was made possible in part by Center for Gas Separations Relevant to Clean Energy Technologies, an Energy Frontier Research Center (EFRC) funded by U.S. Department of Energy (DOE), Office of Science, Office of Basic Energy Sciences under award no. DE-SC0001015, by a Robert A. Welch Chair in Chemistry under award no. A-0030, by the NSF grant DBI-0116835, the VP for Research Office, and the TX Eng. Exp. Station, by the U.S. DOE under contract no. DE-AC02-06CH11357, by the Office of Naval Research under award no. N00014-13-1-0753, the Methane Opportunities for Vehicular Energy (MOVE) Program, an ARPA-e project under award no. DE-AR0000249, by the Welch Foundation under award no. A-1725, by a grant from the

National Institutes of Health under award no. R01GM110137, and by a Strategic Transformative Research Program, Texas A&M University.

Its contents are solely the responsibility of the authors and do not necessarily represent the official views of the funding offices.

TABLE OF CONTENTS

Page

LIST OF FIGURES

Page

LIST OF TABLES

Page

CHAPTER I

INTRODUCTION TO METAL-ORGANIC FRAMEWORKS AND ENZYME IMMOBILIZATION[1]

1.1 Introduction to metal-organic frameworks

Metal-organic framework (MOF) is a type of coordination material that is composed of metal containing clusters and organic ligands. The key chemical feature of MOF is coordination bond.[1] In most MOF materials, the metal ion adopts a coordination environment that is very similar to that of small molecular mononuclear or multinuclear coordination compounds. The organic ligand connects the individual coordination clusters and results in long-range order of unit cells.

Porosity is one of the most intriguing features of MOF materials. Compared with other porous materials, such as activated carbon, silica materials, zeolites, and polymer materials, MOFs possess unprecedented surface area and porosity.[2] This is attributed to the crystalline nature of MOF materials, whereas most of the other materials are amorphous and do not possess intrinsic porosity. The size of MOF cavity can also be tuned into microporous (<2 nm), mesoporous (2-50 nm), and macroporous (>50 nm).[3] The tunability of MOF pore size renders that substrates with different sizes, ranging from gas molecules (N_2, O_2, CO_2, CH_4, etc.) to macromolecules (proteins, coordination cages, heteropolyacids, etc.), can be adsorbed, encapsulated, or diffused through the MOF cavities, which indicates that MOFs have application potentials in energy, catalysis, sensing, or biomedical aspects.[4-68]

---

[1] Part of this chapter is reproduced with permission from "Enzyme-MOF (metal-organic framework) Composite" by Lian, X.; Fang, Y.; Joseph, E.; Wang, Q.; Li, J.; Banerjee, S.; Lollar, C.; Wang, X.; Zhou, H.-C. *Chem. Soc. Rev.*, **2017**, *46*, 3386-3401, copyright 2017 by Royal Society of Chemistry.

1.2 Synthetic approaches of stable MOFs

The stability of MOFs in aqueous conditions is a prerequisite for MOF applications in biomedical researches. Given that carboxylate ligand is the most extensively used ligand for MOF synthesis, the preparation procedures of stable carboxylate-based MOF materials will be introduced. Based on the Hard and Soft Acid and Base (HSAB) theory, since oxygen is hard Lewis base, hard Lewis acid species should be employed in the preparation of stable MOFs.[69] Therefore, high valent metal species, such as Zr(IV), Hf(IV), Fe(III), Al(III), Cr(III), are the most extensively studied metal sources because they tend to form stronger coordination bonds with carboxylate ligands than mono- or di-valent metal species.[16]

The key factor to gain crystalline MOFs other than amorphous products in solvothermal reactions is to control the equilibrium of the formation and dissociation of the coordination bond between metal ions and ligands. The formation of coordination bonds between M(III)/M(IV) with oxygen is thermodynamically favourable, however, the dissociation is typically not, even under elevated temperatures. This imbalance can result in the formation of undesirable amorphous products. To establish the formation-dissociation equilibrium between high valent metal species and ligands, modulating reagents are generally utilized in the stable MOF synthesis, including non-coordinating acid (e.g. HCl, HNO_3, HBF_4, etc.) to slow down the deprotonation of the carboxylic acid, or coordinating acid (e.g. acetic acid, trifluoracetic acid, benzoic acid, etc.) to slow down the bond formation between metal species and the ligands.[16, 70-77] Herein some well-known stable MOFs constructed with high valent metal species and carboxylate ligands will be introduced in detail.

UiO-66, developed by in 2008, consists of 12-connected $Zr_6O_4(OH)_4$ metal cluster and benzenedicarboxylic acid (BDC) ligand (Figure I-1).[73] In the structure, the metal clusters are expanded versions of cubic close packed (CPP) structure. The inner cavity of UiO-66 can be accessed through the triangular window openings. UiO-66 demonstrates a Langmuir surface area of 1187 m^2/g. It shows chemical stability in a number of solvents (water, DMF, benzene, and acetone) and thermal stability up to 540°C, which is among the highest values for all MOF materials. Replacing the BDC ligand with BPDC or TPDC ligand generates UiO-67 and UiO-68 structures, respectively, with increased surface area of the materials (3000 and 4170 m^2/g for UiO-67 and -68, respectively), whereas the chemical stability of the material does not compromise with the increase of ligand length. UiO MOFs with decorated functionalities are also achievable through one-pot synthesis or post-synthetic modifications.

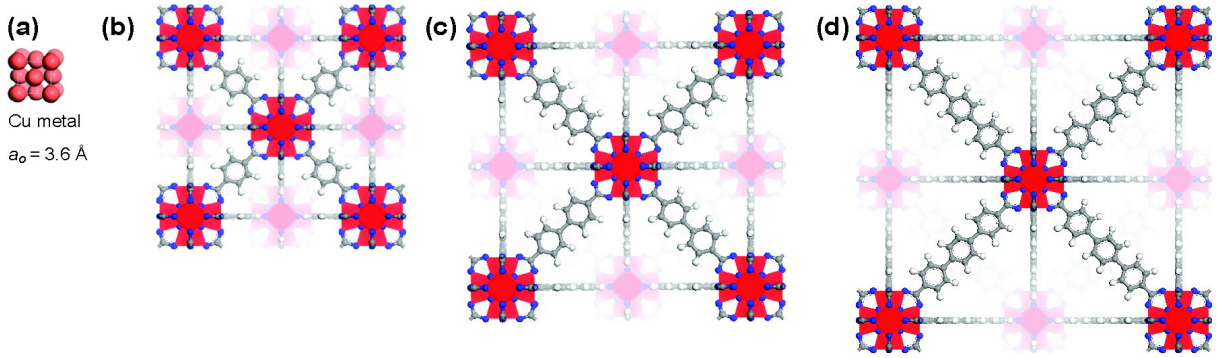

Figure I-1. Structure of UiO-66~68. (a) One unit cell of copper drawn to scale with: (b) Zr MOF with 1,4-benzene-dicarboxylate (BDC) as linker, UiO-66, (c) Zr MOF with 4,4′ biphenyl-dicarboxylate (BPDC) as linker, UiO-67, (d) Zr MOF with terphenyl dicarboxylate (TPDC) as linker, UiO-68. Zirconium, oxygen, carbon, and hydrogen atoms are red, blue, gray, and white, respectively. Reprinted with permission from Ref. 73, copyright © 2008 American Chemical Society.

A series of Zr-porphyrinic MOFs with exceptional stability are reported by Zhou et al, with the name of PCN-22X (X = 1~5).[74-78] All PCN-22X MOFs are composed of TCPP ligand. PCN-221 is composed of Zr_8/Hf_8 cluster, which is unprecedented in molecular chemistry (Figure I-2).[76] The Zr_8/Hf_8 cluster is connected by 12 carboxylate groups with O_h symmetry. Therefore, such a connectivity leads to a very rare (4,12)-connected **ftw** topology. Metalloporphyrinic ligand can also be incorporated in PCN-221 and Zr-PCN-221(Fe) demonstrates very high catalytic activity in the cyclohexane oxidation by tert-butyl hydroperoxide (TBHP) at 65°C. Cyclohexanone is the main product with an 86.9% yield whereas a small amount of cyclohexanol (5.4%) is produced as a side product.

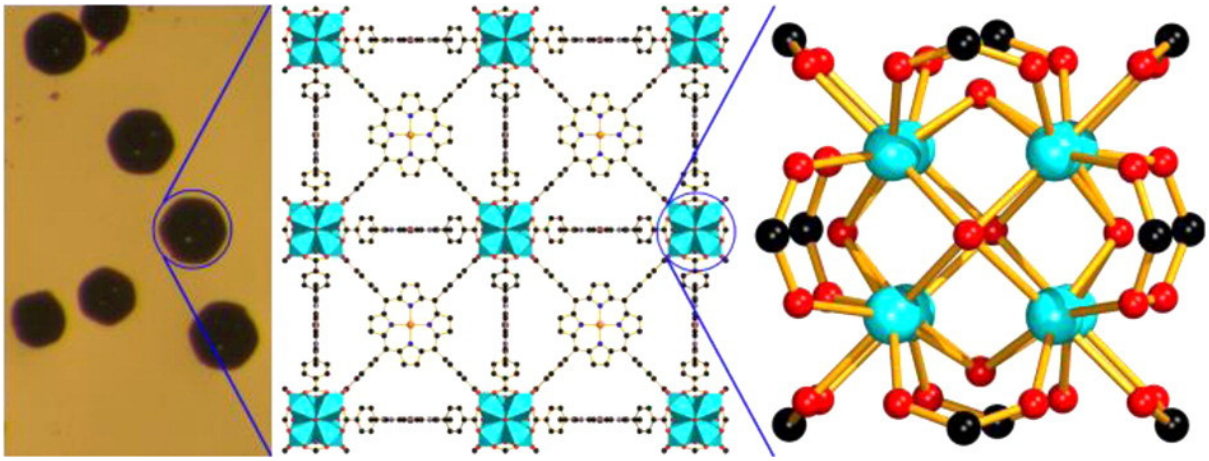

Figure I-2. Optical image of PCN-221(Fe) (left), structure of PCN-221(Fe) (middle), and Zr_8 cluster (right). Reprinted with permission from Ref. 76, copyright © 2013 American Chemical Society.

PCN-222 is composed of an 8-connected Zr_6 cluster and TCPP ligand (free acid form and metallated form) (Figure I-3).[74] PCN-222 contains one of the largest 1D channels with a diameter of up to 3.7 nm. The Brunauer-Emmett-Teller (BET) surface area of PCN-222(Fe) after activation is 2200 m^2/g. PCN-222(Fe) demonstrates exceptional chemical stability relative to all known MOFs. It survives concentrated HCl 24 h treatment as illustrated by the almost unchanged PXRD pattern and N_2 isotherm before and after treatment. The high porosity as well as the extraordinary stability of PCN-222(Fe) suggests that it can be a biomimetic heterogenous catalysis based on the activity of the metalloporphyrin centers. Model reactions (H_2O_2 oxidation of pyrogallol, 3,3,5,5, -tetramethylbenzidine, *o*-phenylenediamine catalysed by PCN-222(Fe)) demonstrates that PCN-222(Fe) has superior activities than hemin and can be regarded as an example of enzyme-mimic catalyst.

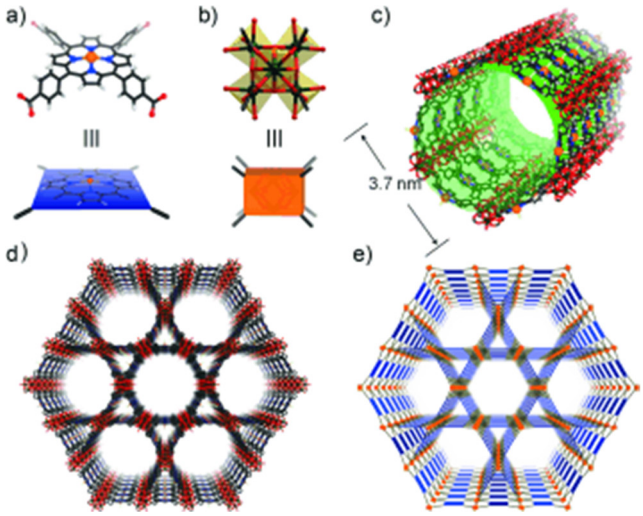

Figure I-3. Crystal structure and underlying network topology of PCN-222(Fe). The Fe-TCPP (a; blue square) is connected to four 8-connected Zr_6 clusters (b; light orange cuboid) with a twisted angle to generate a 3D network in Kagome-like topology (d,e) with 1D large channels (c; green pillar). Zr black spheres, C gray, O red, N blue, Fe orange. H atoms were omitted for clarity. Reprinted with permission from Ref. 74, copyright © 2012 John Wiley and Sons.

PCN-223 is constructed from a rare 12-connected Zr_6 cluster and TCPP (free-base or Fe-coordinated) ligand (Figure I-4).[78] The 12-connected cluster demonstrates D_{6h} symmetry and overall gives rise to the first **shp-a** topology among all reported MOFs. PCN-223 possesses uniform triangular 1D channels of 1.2 nm. Because of the very high connection number of Zr_6 cluster, PCN-223 exhibits extraordinary stability in aqueous solutions with pH value ranging from 0 to 10. Moreover, the high concentration of porphyrinic active sites in PCN-223 results in exceptional catalytic activity in hDa reaction.

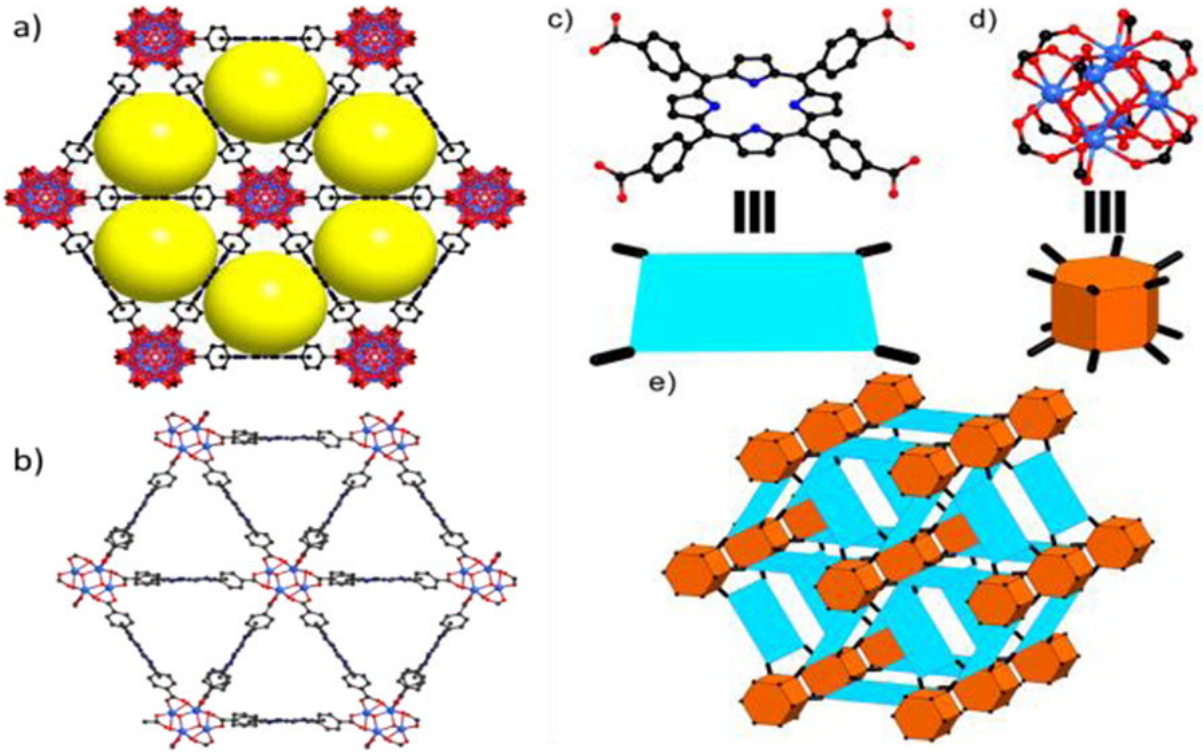

Figure I-4. Structure of PCN-223. (a, b) Views of PCN-223 along the c axis (a) with uniform triangular 1D channels observed in the structure and (b) after removal of disorder. (c–e) Topology analysis of PCN-223. Reprinted with permission from Ref. 78, copyright © 2014 American Chemical Society.

PCN-224 is composed of a 6-connected D_{3d} Zr_6 cluster and TCPP (free base, Ni, Fe, Co) ligand (Figure I-5).[75] Owing to the reduced connection number of metal cluster compared with PCN-222 (8-connected) or PCN-223 (12-connected), PCN-224 demonstrates very high BET surface area (2600 m^2/g). On the other hand, the reduced connection number does not lead to decrease in chemical stability. PCN-224 is stable in aqueous solutions with pH ranging from 0 to 11. Therefore, PCN-224 can be an excellent platform for heterogenous catalysis. PCN-224(Co) mediates the production of cyclic carbonates from CO2 and epoxides with very high turnover frequency (TOF) and exceptional recycling performances.

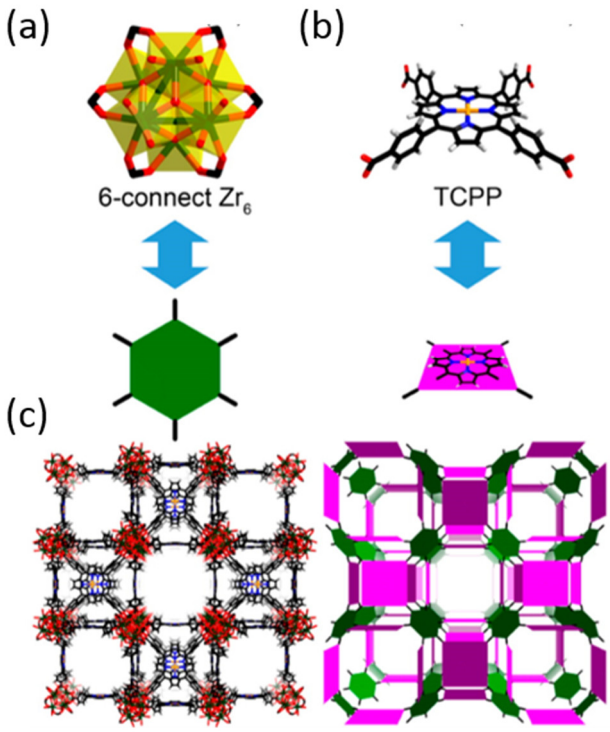

Figure I-5. Crystal structure, structural components, and underlying network topology of PCN-224(Ni). (a) the 6-connected D_{3d} symmetric Zr_6 in PCN-224. (b) Tetratopic TCPP ligands (violet square) with twisted dihedral angles generate a framework with 3-D nanochannels (c). Color scheme: Zr, green spheres; C, gray; O, red; N, blue; Ni, orange; and H, white. Reprinted with permission from Ref. 75, copyright © 2013 American Chemical Society.

PCN-225 constructs from 8-connected Zr_6 cluster and TCPP (free base or Zn).[77] Unlike PCN-222 in which the 8-connected Zr_6 cluster is D_{4h} symmetry, the cluster in PCN-225 adopts D_{2d} symmetry which further reduces the overall symmetry of the framework (Figure I-6). PCN-225 represent the first MOFs with (4,8)-connected **sqc** topology. PCN-225 has two types of channels: 0.8 × 1.5 nm^2 in quadrangle shape and 0.9 × 2.2 nm^2 pear-like shape. PCN-225 remains structural intactness in aqueous solutions with pH = 1-11 as well as boiling water. By taking advantage of the wide pH tolerance of PCN-225, the deprotonation of the porphyrin results in fluorescence change, therefore, PCN-225 is used as a novel fluorescent pH indicator.

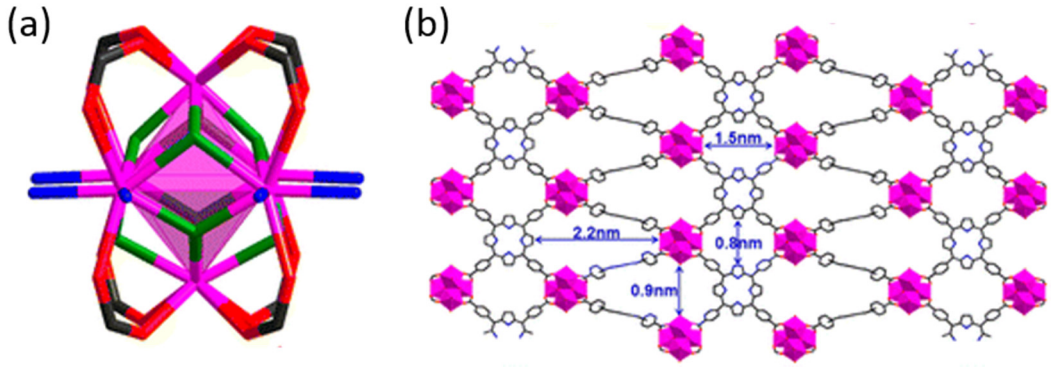

Figure I-6. Structure of PCN-225. (a) $Zr_6(\mu_3\text{-}O)_4(\mu_3\text{-}OH)_4(OH)_4(H_2O)_4(COO)_8$ cluster. The oxygen atoms from μ_3-OH/-O, OH/H_2O and COO groups are shown in green, blue and red, respectively. (b) View of the structure of PCN-225 along the b-axis with two types of channels. The Zr, O, C, N atoms are shown in pink, red, gray and blue, respectively. H atoms are omitted for clarity. Reprinted with permission from Ref. 77, copyright © 2013 American Chemical Society.

MIL-53 is synthesized by hydrothermal reaction of chromium(III) nitrate and BDC ligand with the presence of hydrofluoric acid.[70] It is composed of 1D Cr-O infinite chain bridged by BDC ligand (Figure I-7). The as-synthesized MIL-53 has 1D channel containing unreacted BDC ligand, which can be removed by thermal treatment at 300ºC, yielding MIL-53ht. MIL-53ht possesses uniform 13.04 × 16.83 $Å^2$ 1D channel. MIL-53ht adsorbs moisture in air, yielding MIL-53lt, and the pore dimension changes to 7.85 × 19.69 $Å^2$. This hydration-dehydration induced breathing effect can be ascribed to two conjugated phenomena. First, the water molecule forms strong hydrogen bonds with the hydrophilic parts of the pore. Second, the π-π interaction between the benzyl groups are feasible due to the short ring separation distance (d(C-C) ≈ 3.9-4.5 Å). Remarkably, this large breathing phenomenon is fully reversible.

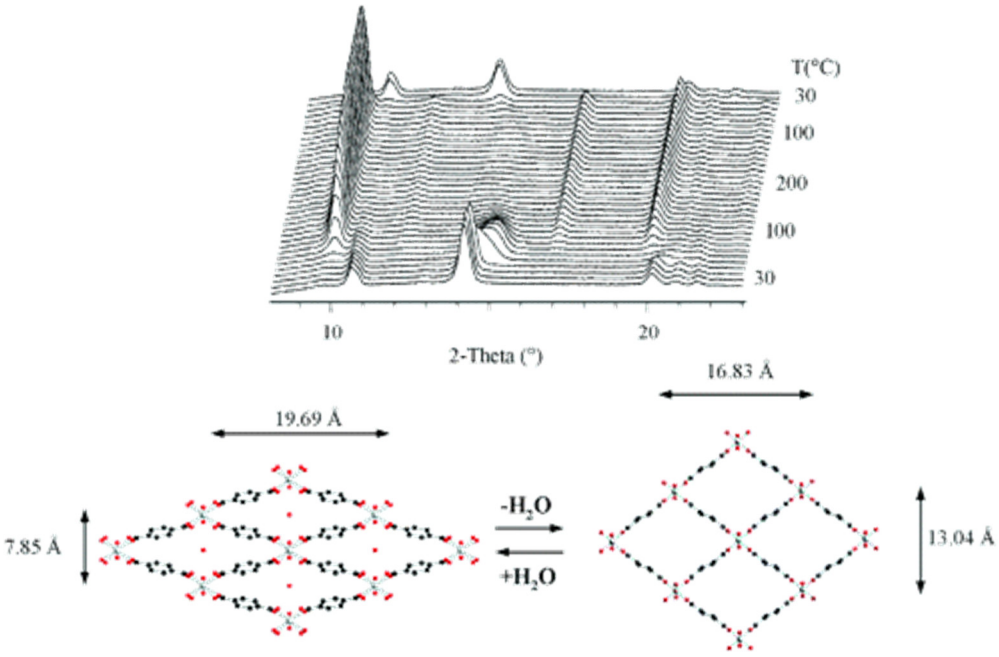

Figure I-7. Temperature variability of MIL-53. (top) Schematic representation of the reversible hydration dehydration of MIL-53lt and MIL-53ht. (bottom) X-ray thermodiffractogram of MIL-53lt under air; for a better understanding, a 2θ offset is applied for each pattern. Reprinted with permission from Ref. 70, copyright © 2002 American Chemical Society.

MIL-100 is prepared from metallic chromium and 1,3,5-benezenetricarboxylic acid (BTC) with the presence of hydrofluoric acid.[71] MIL-100 is composed of trimeric-oxo cluster $Cr_3(\mu_3O)$ connected with BTC ligand, which generates a supertetrahedron (STH) with metal cluster on the corner and BTC ligand on the face (Figure I-8). STH then connects with each other on a vertex sharing manner to generate MIL-100 structure. There are three types of porosities in MIL-100: one microporous cavity (Ø ≈ 6.5 Å), and two mesoporous cavities (Ø ≈ 25-30 Å). The smaller mesoporous cavity has a diameter of 25 Å and is composed of 20 STHs, whereas the larger mesoporous cavity has a diameter of 29 Å and is composed of 28 STHs.

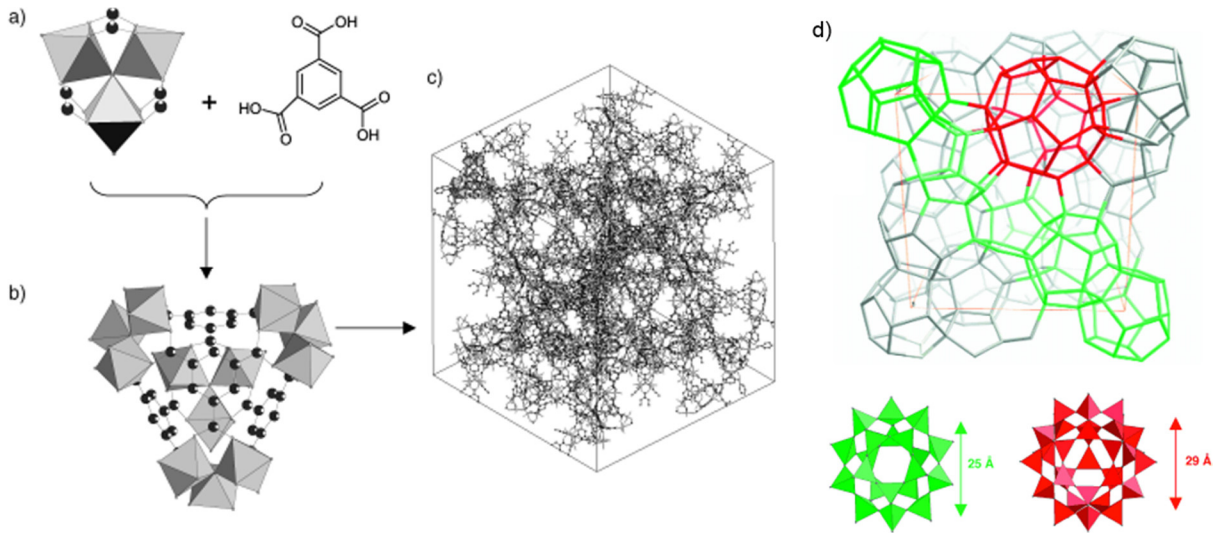

Figure I-8. Structure and topology of MIL-100. a) The original building block with a trimer of metal octahedra chelated by three carboxylic functions. b) The STH formed by using trimesic acid, which occupies the faces of STH. c) Ball-and-stick view of a unit cell of **MIL-100**. Free water molecules have been omitted for clarity. d) Top: Schematic view of the 3D organization of the structure of **MIL-100**with the medium (green) and large (red) cages delimited by the vertex sharing of the STH (the vertices represent the centers of each STH). Bottom: View and dimensions of the two different cages (green, 20 STH; red, 28 STH). The medium cages share faces and form interconnected rods (in green) in the interstices of which are located the large cages. Reprinted with permission from Ref. 71, copyright © 2004 John Wiley and Sons.

A similar MOF to MIL-100, MIL-101, is composed of $Cr_3(\mu_3O)$ cluster and BDC ligand.[72] Similarly, the connection between metal cluster and BDC ligand generates STH with cluster on the corner and ligand on the edge (Figure I-9). MIL-101 contains two types of mesoporous cavities: the smaller one with diameter of 29 Å with exclusive pentagonal windows (Ø ≈ 12 Å), whereas the larger one with diameter of 34 Å with not only pentagonal windows but also hexagonal windows (Ø ≈ 15 Å). MIL-101 has one of the highest surface areas and pore volume. Owing to its exceptional porosity, large guest molecules, such as Keggin polyanions, can be incorporated into the cavity of MIL-101.

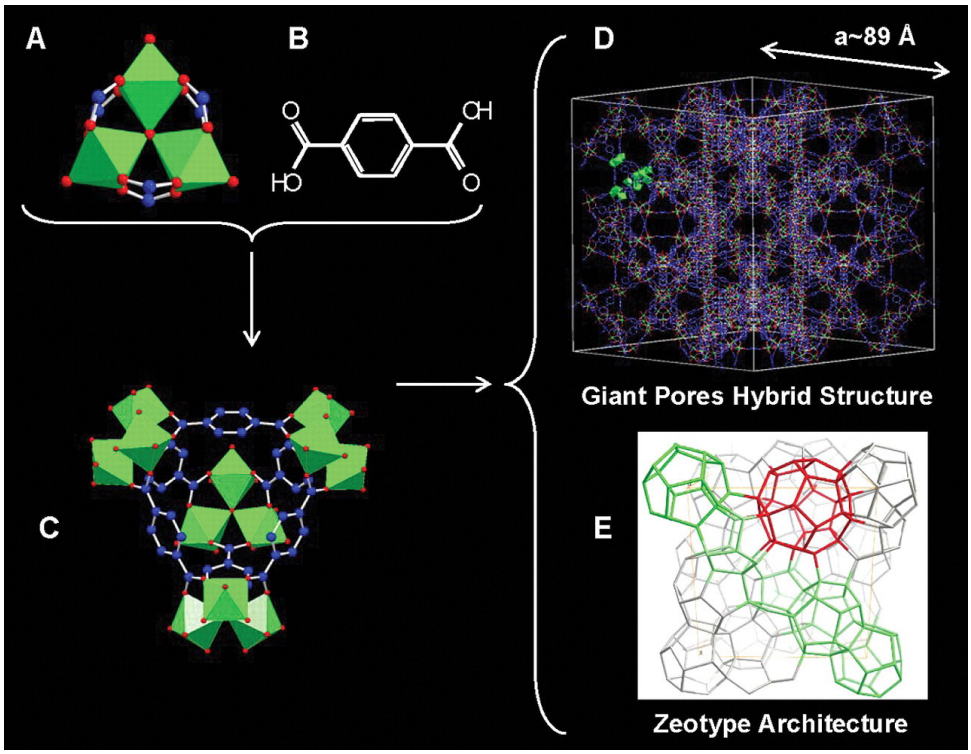

Figure I-9. Structure and topology of MIL-101. (**A**) The computationnally designed trimeric building block chelated by three carboxylic functions. The ST was constructed with (**B**) terephthalic acid, which lies (**C**) on the edges of the ST. (**D**) Ball-and-stick representation of one unit cell, highlighting one ST drawn in a polyhedron mode. (**E**) Schematic 3D representation of the MTN zeotype architecture (the vertices represent the centers of each ST) with the medium (in green, with 20 tetrahedra) and large (in red with 28 tetrahedra) cages delimited by the vertex sharing of the ST. Chromium octahedra, oxygen, fluorine and carbon atoms are in green, red, and blue, respectively. Reprinted with permission from Ref. 72, copyright © 2005 American Association for the Advancement of Science.

1.3 Enzyme immobilization: principles and applications

Enzymes are indisputably one of the most important biomacromolecules for life, far exceeding artificial catalysts in their ability to efficiently catalyse life-sustaining biological transformations.[79] Consequently, applying *in vivo* enzymatic transformations to industrial processes is an attractive strategy in order to circumvent the existing laborious design and synthesis of artificial catalysts.[80] However, such practical applications are hindered by enzymes' fragile nature, such as low thermal stabilities, narrow optimum pH ranges, low stabilities towards extreme pH values, low tolerances to most organic solvents and many metal ions, etc. Moreover, enzymes themselves are a source of contamination in the desired product, resulting in inevitable purification and separation steps. Therefore, instead of using enzymes homogeneously, employing heterogeneous immobilized enzymes is one of the key strategies for improving the practical performances of enzymes.[81-83]

The term "immobilized enzymes" refers to "enzymes physically confined or localized in a certain defined region of space with retention of their catalytic activities, and which can be used repeatedly and continuously".[84] Immobilizing enzymes on solid support offers more effective control of the reaction processes and enhanced enzyme stability in storage and operational conditions.[85] Moreover, the heterogeneous nature of the immobilized enzymes provides more facile separation from the product, minimizing contamination from the enzymes.[86-88] The immobilized enzymes can be recycled to reduce the cost of the production processes.[86, 89, 90] Besides the potential benefits brought by enzyme immobilization, it is important to recognize that the chemical and physical properties of an enzyme can suffer changes upon immobilization depending on the choice

of immobilization matrix and method.[91] Therefore, it is imperative to identify an immobilization matrix and technique that cause the smallest loss of enzymatic activity.

1.3.1 Synthesis of enzyme immobilization materials

Generally, there are three enzyme immobilization categories: adsorption, covalent bonding, and entrapment (Figure I-10).[92] The details of each immobilization method will be introduced below.

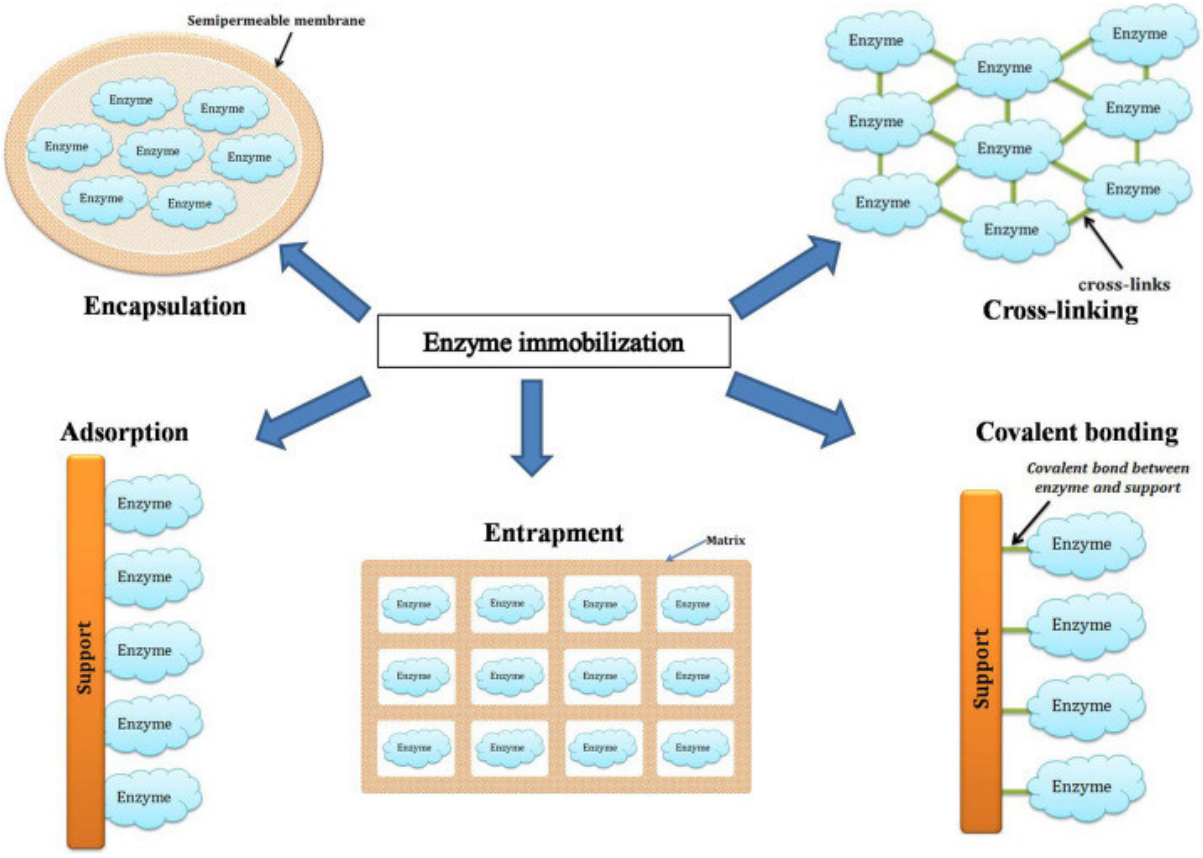

Figure I-10. Various methods of enzyme immobilization. Reprinted with permission from Ref. 92, copyright 2016 © Elsevier Inc.

1.3.1.1 Adsorption

In this method, enzymes adhere to the surface of the matrix by weak interactions (hydrogen bonding, hydrophobic interactions, etc.) with the lack of covalent/coordination bond formation. Typically, this process involves suspending immobilization matrix in enzyme solutions or electrical deposition of enzymes on the electrode surface. Water soluble materials, such as polysaccharide derivatives, glass, coconut fibers, kaolin, polymers, and cellulose materials, are the commonly used immobilization matrices.[93] The adsorbed enzymes are usually resistant to proteolytic digestion and self-aggregation because of the hydrophobic interaction with the interfaces.[94]

Persson et al reported lipase enzyme adsorption on polypropylene-based hydrophobic granules/Accurel EP-100.[95] They found that reducing the particle size of Accurel significantly increased the enantiomeric ratio and reaction rates of immobilized lipase. *Yarrowia lipolytica* lipase immobilized on octyl-agaros and octadecyl-sepa beads demonstrated greater stability, higher enzymatic conversion yields, better process control, and improved economic effects compared with free lipase.[96] This can be attributed to the hydrophobic interaction between lipase and the beads. *Candida rugosa* lipase adsorbed on poly(3-hydroxybutyrate-co-hydroxyvalerate) expressed 94% activity even after treating for 4 h at 50^{o}C and reusing till 12 cycles.[97] Urease enzymes adsorbed on 1,4-butenediol diglycidyl ether-activated byssus threads demonstrated increased pH stability and activity retaining under dried conditions.[98]

1.3.1.2 Covalent binding

This method depends on the formation of covalent bond between the enzyme and the immobilization matrices. Side chain amino acids, such as histidine, arginine, aspartic

acid, may form bonds with matrices. Typically, bond formation takes place when activators are present (e.g. carbodiimide compounds).[99, 100] When immobilization matrices are decorated with peptide on the surface, higher specific activity and stability with controlled protein orientation can be achieved.[99] Enhanced enzyme stability can also be achieved by covalently binding of enzymes onto silica gel carriers that unreacted aldehyde groups have been removed beforehand.[101]

Cross-linking of the enzyme with immobilization matrices stands for another manner of covalent enzyme binding. Glutaraldehyde is a popular cross-linking agent owing to its solubility in aqueous solvents and its ability to form inter- or intra-subunit covalent bonds. Moreover, cross-linking of enzymes shows improved residual activity because of the increased porosity and surface area.[102] Zhao et al demonstrated that alcohol dehydrogenase enzyme covalently immobilized on attapulgite nanofibers had higher thermal tolerance.[103]

1.3.1.3 Entrapment

This method is to non-covalently encapsulate enzymes within a network that protect the enzyme while at the same time, the enzyme is accessible to substrates.[104] Experimentally the enzyme encapsulation can be achieved by three strategies: (1) inclusion of enzyme within a cross-linked polymer matrix; (2) dissolution of enzyme in a nonaqueous phase; (3) separation of enzyme from bulk solution by semipermeable micro-capsule. Encapsulation with alginate-gelatin-calcium hybrid carriers has been reported to increase mechanical stability and prevent enzyme leaching.[105] A simultaneous encapsulation of lipase and magnetic nanoparticles into biomimetic silica significantly increased enzyme activity under various silane additives.[106] Lipase encapsulated in κ-

carrageenan showed high tolerance to organic solvents and heat shock.[107] Moreover, electrospun nanofibers based enzymatic hybrid materials have shown application potentials in biomedicine, biofuel, chemistry, biosensors, etc.[108]

1.3.2 Enzyme immobilization matrices

The materials used for enzyme immobilization, called immobilization matrices, should include the following properties. (1) They should be tolerant to the enzyme immobilization operational conditions. (2) They should have high enzyme immobilization capacity. (3) Any undesirable denaturation induced by the immobilization matrices should be excluded.[109] Commonly used immobilization matrices are divided into two categories: inorganic matrices and organic matrices.

1.3.2.1 Inorganic matrices

This category includes glass, silica gel, carbon materials, and metal oxides, by taking advantage of their thermal and mechanical resistance.[110] Moreover, they are resistant to microbial growth and they can provide rigidity and porosity. Details of typical materials will be introduced below.

1.3.2.1.1 Silica

Silica-based inorganic enzyme immobilization support includes silicon dioxide, silicon tetraoxide and zeolite. Silica materials have both hydrophilic and hydrophobic sites. They are chemically inert and they need modification and proper activation. A typical procedure is to treat silica materials with aminoalkyl triethoxysilanes to introduce amino groups to the surface. Penicillin G amidase conjugated with dextran was immobilized on amino-modified silica gel and showed increased thermal stability.[111] Another example is lignin peroxidase and horseradish peroxidase immobilized on

activated silica support could remove chlorolignins effectively from eucalyptus kraft effluent.[112]

1.3.2.1.2 Metal oxide

Metal oxide, including Al_2O_3, TiO_2, ZrO_2, and SnO_2, is another type of inorganic support because of its porous nature. *Candida Antarctica* lipase enzyme immobilized on metal oxide membrane could carry out hydrolytic and synthetic reactions by restraining feedback inhibition.[113] Switching membrane to foam support could increase the specific surface area and decrease diffusion rates.[113]

1.3.2.1.3 Glass

Glass is highly viscous in nature and has been used as enzyme immobilization support. Phthaloyl chloride-containing amino group functionalized glass beads showed sustained enzymatic activity when α-amylase was immobilized.[92] Urease immobilized on glass pH-electrodes served as effective biosensor for blood urea, demonstrating a detection level down to 52 mg/mL.[114]

1.3.2.1.4 Carbon materials

This type includes charcoal and activated carbon. Charcoal has been used to immobilize amyloglucosidase without cross-linking agents for starch hydrolysis.[115] Activated carbon, typically possessing high surface area and pore volume, has been used to immobilize acid protease and acidic lipase that the catalytic activity was well maintained even after 21 reusing cycles.[116]

1.3.2.2 Organic matrices

This type of matrix is mainly composed of water-insoluble polysaccharides because they are chemically inert and they can bind proteins in reversible and irreversible

manners. Alginate is a sulphated polysaccharide obtained from brown algal cell wall. Immobilized enzyme gained extra stability when alginate cross-linked with divalent ions and glutaraldehyde.[117] Chitosan has been widely investigated as enzyme immobilization matrix. Enzyme coated with chitosan has less leaching effect compared with immobilization on alginate owing to its ionic and physical interactions with the enzyme.[118] Cellulose is one of the most commonly used enzyme immobilization matrix due to its commercially availability. Enzyme immobilized on ionic liquid-cellulose film activated with glutaraldehyde showed increased tolerance and feasibility.[119] Collagen can be a good immobilization platform because it forms covalent bond with enzyme, thereby strongly confine the enzyme with the matrix. Catalase immobilized on Fe^{3+}-collagen fibers remained activity even after 26 reuses.[120]

1.3.3 Applications of immobilized enzymes

1.3.3.1 Biosensors

The electrical, chemical, optical, or mechanical devices which can detect biological species are called biosensors. An ideal biosensor should be able to detect low concentration of a specific analyte in complex samples with quick response time and high selectivity. Biosensors based on enzyme immobilization typically possess the above-mentioned features and can be easily used in stationary or in flow system. A number of enzyme immobilized sensors could detect heavy metals in aqueous solutions.[121-124] In another case, acetylcholinesterase A (AchE) immobilized biosensors could detect toxic pesticides.[125]

1.3.3.2 Waste water treatment

The effluents of a number of industries contain carcinogenic dyes.[126] Enzymes catalysing redox reactions can play an important role in dye degradations. But due to the harsh operational conditions, free enzymes can lose activities very fast. Therefore, immobilization can be an ideal strategy. For example, immobilized laccase can degrade various dyes, such as anthracinoid dye, lancet blue, etc.[127]

1.3.3.3 Biodiesel production

Biodiesel is a liquid fuel produced by triglycerides and esterification of alcohol in the presence of catalyst. However, the production of traditional catalyst consumes huge energy. Using enzyme immobilized catalyst can reduce the energy consumption, as demonstrated in a case which immobilized lipase was involved.[128]

1.4 Enzyme immobilization on MOFs: advantage over free enzyme

Owing to the exceptional tunability of MOF structure, pore size, shape and environment, enzyme immobilization on MOFs have received extensive attention in the past decade. Typical preparation methods of enzyme-MOF composites include surface attachment, pore encapsulation, covalent linkage, and one-pot coprecipitation/biomineralization. Many of these are very similar to Section 1.3.1. Examples of enzyme-MOF composites are summarized in recent reviews.[129] Below only the advantage of MOF-immobilized enzymes over their free counterparts will be introduced.

1.4.1 Reusability

One of the greatest advantages immobilized enzymes have over free enzymes is their recyclability, which significantly reduces costs. Moreover, immobilized enzymes

show a significantly lower proportion of impurities resulting from product contamination when compared to free enzymes. Enzymes anchored by robust covalent bonds to MOF matrices, such as trypsin–MIL-88B, are able to maintain their catalytic performances, showing a negligible activity loss even after 4 cycles.[130] Besides covalent linkages between enzymes and MOFs, weak interactions also considerably improve the reusability of the immobilized enzymes.

As evidenced in the case of BSL2@HKUST-1, MOF–enzyme host–guest interactions improve the reusability of immobilized enzymes.[131] Substrate conversion after 10 cycles did not demonstrate any substantial drop, which indicates that BSL2 was stabilized by the planar BTC ligand of the MOF through hydrophobic interactions.

In many pore encapsulation cases, using MOFs with pore windows smaller than the size of the enzyme prevents leaching of the enzyme, which significantly contributes to the exceptional reusability of the composite. In composites made with Tb-meso-MOFs, MP-11@Tb-mesoMOF maintained its activity over 6 cycles, while Mb@Tb-mesoMOF maintained activity over 15 cycles without a significant drop.[132, 133] In another case, at

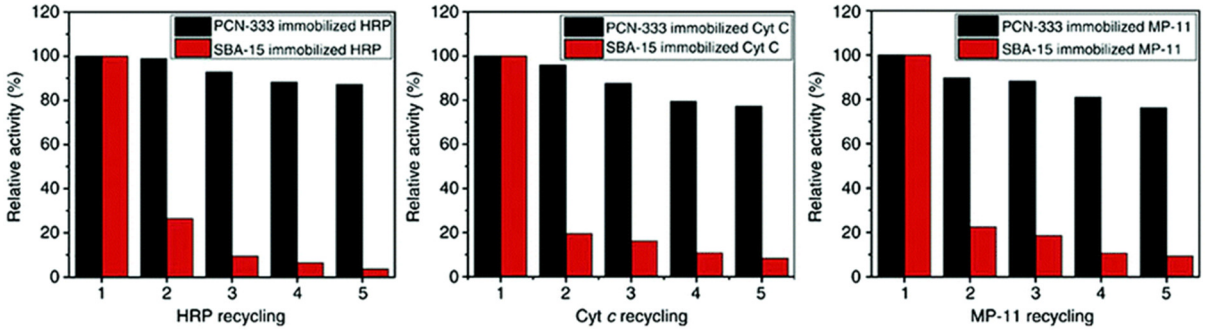

Figure I-11. Catalytic activity of immobilized enzymes in each recycle test. Reprinted with permission from Ref. 129, copyright 2017 © Royal Chemical Society.

least 80% activity of HRP was retained within 5 cycles when it was immobilized on a mesoporous MOF, PCN-333. On the contrary, HRP immobilized on SBA-15 lost more than 70% activity in the first cycle (Figure I-10).[134]

Dye tagging on enzymes can also improve the reusability of the immobilized enzymes. Trypsin–FITC@CYCU-4 maintained more than 80% activity after 3 to 5 cycles. The recyclability can be attributed to the specific host–guest interactions between FITC and CYCU-4's micropores and the confinement of trypsin within CYCU-4's mesopores.[135] In contrast, unmodified trypsin immobilized on CYCU-4 demonstrated a significant drop in activity after the first cycle. Moreover, size matching of the dye molecule and the MOF cavity significantly improves the reusability of dye tagged MOF–enzyme composite. As an illustration, trypsin–NBD@UiO-66 demonstrated almost 100%

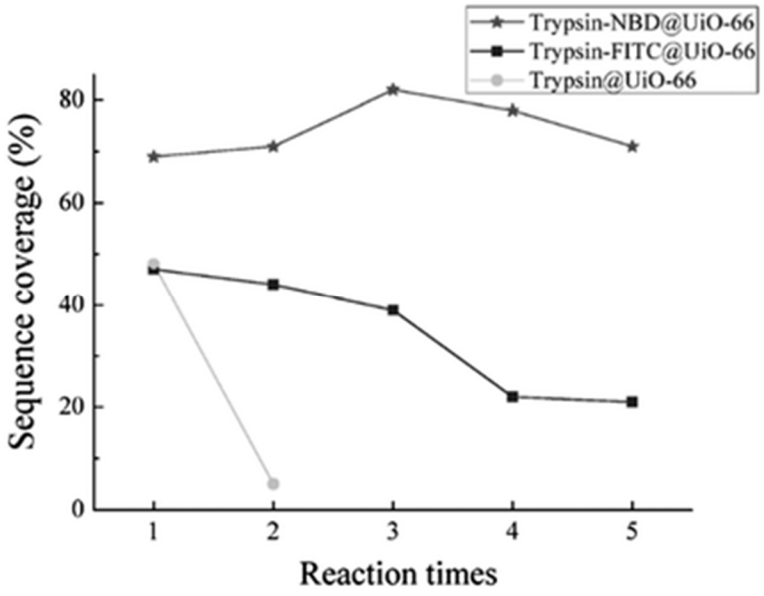

Figure I-12. BSA proteolytic efficiency of trypsin–NBD@UiO-66, trypsin–FITC@UiO-66 and trypsin@UiO-66. Reprinted with permission from Ref. 129, copyright 2017 © Royal Chemical Society.

activity after 5 cycles of BSA digestion due to the size compatibility of NBD molecule with the microporous cavities of UiO-66, whereas trypsin–FITC@UiO-66 lost more than half of its activity by the 5th cycle, a result of the incompatible size interaction between the small MOF pore and the large FITC molecule (Figure I-11).

1.4.2 Catalytic activity

Many MOF–enzyme composites demonstrate enhanced catalytic activities when compared with the free enzymes. This is evidenced by improved conversion rates and percentages, which are typically ascribed to: (1) single enzymes are confined by MOF cavities; (2) functional groups on the MOF backbones are actively involved in the catalytic processes. Additionally, the size of the pore opening can render unusual size selectivity to MOF immobilized enzymes.

In many cases, immobilization prevents undesirable enzyme self-aggregation, which usually results in slow conversion rates or poor yields. In MP-11, the aggregation significantly reduces the accessibility of the heme moiety, thus adversely affects its activity. Upon immobilization on Cu–MOF and Tb-mesoMOF, MP-11 demonstrated increased conversion percentages of 10 and 4 times respectively. The same effect was observed for BSL2@HKUST-1, whose initial rate was 18 times that of the free BSL2.[131]

The functionalities of MOFs can affect the activities of immobilized enzymes through hydrophilic/hydrophobic interactions. For example, the conversion percentage of PPL@UiO-66-NH_2 demonstrated 11% lower than PPL@UiO-66, whereas PPL immobilized on carbonized MIL-53(Al) demonstrated a 5% activity enhancement compared to PPL@MIL-53(Al).[136] This result indicates that the hydrophobicity of UiO-66 and carbonized MIL-53(Al) are favourable for the adsorption of the hydrophobic

lipase onto the MOF's surface, thus leading to higher activity. In another case the BSA hydrolysis activity of trypsin immobilized MIL-88B-NH_2 was 2 times more than that of trypsin immobilized MIL-88 or MIL-101. The authors claimed that the hydrophilic amino groups on the surface of MIL-88B-NH_2 reduced undesired non-specific BSA–MOF interaction and enhanced the interaction between BSA and immobilized trypsin through hydrogen bonding.

Furthermore, the size incompatibility of large substrates with relatively small apertures of MOFs can result in restricted substrate diffusion into the MOF cavity, allowing for substrate selectivity in the immobilized enzymes. The first size selective catalysis for Mb was achieved by Mb@Tb-mesoMOF.[133] The initial rate for THB was almost 6 times faster than that for ABTS in Mb@Tb-mesoMOF mediated conversions, and was more than double the rate of catalysis by free Mb and Mb@SBA-15. The large ABTS molecule, with dimensions of 1.01 × 1.73 nm^2, was unable to enter the small pore (0.9 nm) of Mb@Tb-mesoMOF. However, the small THB molecule (0.57 × 0.58 nm^2) could feasibly approach immobilized Mb *via* diffusion through the pores.

1.4.3 Stability

Enzyme denaturation occurs when enzymes are exposed to extreme pH, extreme temperature, or organic solvents. These external stresses can alter the conformation of enzymes, which results in the loss of enzymatic activity due to the deformation of the active site. The physical immobilization of enzymes on MOFs minimizes the loss of enzymatic conformation under these conditions, thus enhancing the enzymes' tolerance to denaturation conditions. A covalently immobilized SEH–MOF composite, SEH@UiO-66-NH_2, demonstrated an activity enhancement of 60% at pH 8.5 and 75% at 45 °C

compared with free SEH. This is most likely owing to the stabilization of the enzymes provided by cross-linking with MOF supports. In OPAA@PCN-128y, its activity could be retained after treatment at 70 °C or 3 days dry storage, while free OPAA could only survive at 45 °C or 1 day after lyophilisation.[137] A HRP@ZIF-8 composite could maintain 85% activity under boiling water or boiling DMF treatment. This result is unprecedented in enzyme immobilization on other materials (Figure I-12).[138] Lipase entrapped in ZIF-8 demonstrated exceptional stability under various denaturation conditions.[139] The activity

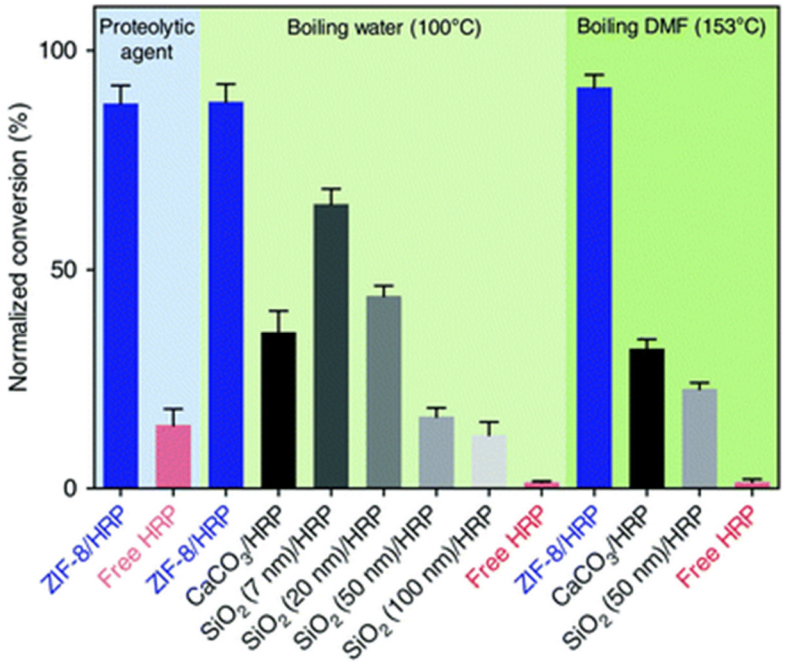

Figure I-13. The resistance of free or immobilized enzymes towards perturbations. Product conversion of free HRP, the biomimetically mineralized ZIF-8 using HRP (ZIF-8/HRP), HRP protected by calcium carbonate ($CaCO_3$/HRP) and HRP protected by mesoporous silica (SiO_2/HRP, SiO_2 with average pore size of 7, 20, 50 and 100 nm) in the presence of proteolytic agent, trypsin, after treatment in boiling water for 1 h, and after treatment in boiling DMF for 1 h at 153 °C, respectively. Data were normalized against free HRP activity at room temperature. Error bars represent the s.d. of three independent experiments. Reprinted with permission from Ref. 129, copyright 2017 © Royal Chemical Society.

enhancement of the composite over free enzyme was more than 40% with 1 mM Zn^{2+} treatment, 30% at 85 °C, and 60% at 50 °C treated for 50 minutes.

Trypsin digestion is another important denaturation route for *in cellulo* or *in vivo* enzyme applications. The small apertures of MOFs can prevent the entry of trypsin and avoid undesired digestion, which is important to the preservation of enzymatic activity. A bi-enzyme immobilized ZIF-8 composite maintained more than 90% of its activity after treated with 1 mg mL ^{1} trypsin for 30 minutes at 37 °C while the free enzymes lost more than 50% of its activity under the same treatment.[140] A similar protective effect was observed for a mesoporous MOF, PCN-888, with almost all activity maintained after 60 minutes of trypsin treatment.[141]

1.5 Summary

Enzyme immobilization has attracted extensive attention owing to the improved performances, especially in harsh *ex vivo* conditions, compared with free enzymes. Traditional matrices, although demonstrating promising performances in some cases, are hindered by intrinsic shortcomings. For example, sol–gel matrices are intrinsically porous and can prevent enzyme leaching due to entrapment. However, the entry of bulky substrates into these pores is sometimes restricted.[142] Moreover, enzyme immobilization takes place during sol–gel synthesis which may lead to enzyme denaturation. Enzymes immobilized in hydrogels or organic microparticles suffer from leaching (owing to the swelling or degradation of the matrices), enzyme denaturation, and restricted mass transfer.[143-145] Mesoporous silica, bearing large surface area and pore volume, have attracted much attention.[146-148] However, the challenges of rational structural design, leaching of enzymes from the support, and surface charges that promote enzyme

denaturation or reduction of enzyme loading hinder the use of mesoporous silica as an enzyme support. MOFs can be novel platforms for enzyme immobilization owing to (1) extraordinary tunability in structure, pore size, shape, and environment; (2) permanent porosity that allows for substrate and product diffusion; (3) feasible modification on the surface to achieve selective accumulation in in vivo applications; (4) robustness in aqueous conditions that protect vulnerable enzymes against perturbation.

Besides the numerous works that have demonstrated the enzyme encapsulation capability of MOF matrices, operating MOF–enzyme composites in biomedical conditions has been rarely reported. As this could lead to novel strategy for life-sustaining technologies, such as enzyme replacement therapy or enzyme supplement therapy, it is highly desirable to study the performance of MOF-enzyme composites in cell culture and animal model level before taking into account of pre-clinical applications and clinical trials. Several MOF–enzyme composites demonstrate retention of enzymatic activities under trypsin digestive pressure, indicating that they might be able to serve as transportation vehicles for enzyme replacement therapy *in vivo*, as free enzymes are rapidly eliminated from the circulatory system.[149] The enantiomeric selectivity demonstrated by MOF–enzyme composites also prove beneficial to the pharmaceutical industry, where selectivity is vital due to significant differences in biological activities of enantiomers. More application-based studies need to be conducted in order to optimize the MOF–enzyme composites for more specific functions. In addition, the facile post-synthetic modification amenability of MOFs allows for the development of highly targeted systems.[150, 151] Overall, although only proof-of-concept studies are accomplished

on this novel composite, the development of MOF–enzyme composites has shown huge potential, providing a springboard for further development.

CHAPTER II

THE PREPARATION OF AN ULTRASTABLE MESOPOROUS CR(III)-MOF VIA REDUCTIVE LABILIZATION[2]

2.1 Introduction

Bearing the high surface area, large pore size and volume as well as the tunability of pore environments and functionalities, metal-organic frameworks (MOFs) have demonstrated promising applications in storage, separation, catalysis, guest moiety immobilization, drug delivery and sensing.[38, 152-154] Many of these applications include the use of metal nodes, or secondary building units (SBUs), as active sites. SBUs are always explored as Lewis acid species, while their redox properties have been studied in only a few reports.[155, 156] One of experimental demonstrations is the reduction of high valence Fe(III) to generate low valence Fe(II) in MIL-100-Fe(III) by carbon monoxide, indicating the possibility of tuning the chemical robustness of the framework by redox reaction.[155]

Based on the Hard and Soft Acid and Base (HSAB) Theory,[69] chemically robust MOFs can be constructed with carboxylate ligand, defined as a hard Lewis base, and high valence metal ions, such as Fe(III), Cr(III) or Zr(IV), categorized as hard Lewis acids. Compared with MOFs composed of divalent species, many of these high valence metal containing MOFs can survive in water, or even acid or base solutions. This phenomenon has been exclusively demonstrated in MIL series, UiO series and PCN-22X series.[16, 72, 73, 78, 157-163]A recent example is an iron based mesoporous MOF, PCN-333-Fe(III), which is stable in both acidic and basic aqueous solutions despite its ultrahigh porosity.[134]

---

[2] Reproduced with permission from "The preparation of an ultrastable mesoporous Cr(III)-MOF *via* reductive labilization" by Lian, X.; Feng, D.; Chen, Y.-P.; Liu, T.-F.; Wang, X.; Zhou, H.-C. *Chem. Sci*., **2015**, *6*, 7044-7048, copyright 2015 by Royal Society of Chemistry.

However, MOFs constructed with high valence metal ions may suffer from structure breakdown in some specific environments, for instance, PCN-333-Fe(III) totally loses its crystallinity and porosity in alkylamine solution. Incorporation of kinetically inert metal ions, for example, Cr(III), into the framework backbone could generate MOFs with exceptional stability.[72, 164]

Nevertheless, obtaining crystalline Cr(III)-MOFs with carboxylate ligands are extremely difficult due to the inertness of Cr(III). Hydrothermal conditions are exclusive adopted in the synthesis of crystalline Cr(III)-MOFs, but these conditions might be unfeasible for larger organic ligands as they are extremely hydrophobic. Synthetic attempts of PCN-333-Cr(III) by either hydrothermal or solvothermal conditions with temperature as high as 220ºC failed to generate any crystalline products. An alternative synthetic pathway is post synthetic metathesis of metal clusters from a template MOF with a known structure. Fe(III)-MOFs can serve as practical structural templates because iron resembles chromium in both coordination geometry and valence. Disappointingly, metathesis of PCN-333-Fe(III) with $CrCl_3$ for 24 hours only yielded partially metathesized MOF. The incompleteness of the above metathesis is not surprising since in several reports demonstrating the feasibility of metal metathesis for thermodynamically inert MOFs, complete metal metathesis has never been achieved.[162] This is mainly contribute to two reasons: (a) the dissociation of high valence metal ions from framework is thermodynamically unfavorable; (b) the dissociation rate of high valence ions is much slower than that of the divalent species due to the much higher activation energy. Therefore, long reaction time or elevated reaction temperature is required in order to

achieve complete metathesis. However, under these scenarios, framework decomposition is usually inevitable due to the acidic environments generated by high valence species.[165]

Herein, we report a reductive labilization-metathesis route for the synthesis of PCN-333-Cr(III) with PCN-333-Fe(III) as the template, wherein redox chemistry has contributed to the generation of labile metathesis intermediates. PCN-333-Cr(III) demonstrated broader range of applications than PCN-333-Fe(III) in consequence of its improved chemical sustainability. The alkylamine incorporated PCN-333-Cr(III) demonstrated significant CO_2 adsorption capacity under low pressure whereas PCN-333-Fe(III) barely shows any CO_2 adsorption capacity due to structural decomposition in alkylamine solution.

2.2 Experimental Section

2.2.1 Materials and Instrumentation

Materials

Iron(III) chloride anhydrous ($FeCl_3$), anhydrous $AlCl_3$, cyanuric chloride, $MgSO_4$, chromium(II) chloride anhydrous ($CrCl_2$), chromium trioxide, sulfuric acid, acetic acid, acetic anhydride, toluene, chloroform, N,N-dimethylformamide (DMF), N,N-diethylformamide (DEF), methanol, trifluoroacetic acid (TFA) were purchased from Alfa Aesor. All commercial chemicals were used without further purification.

Instrumentation

Powder X-ray di raction (PXRD) was carried out with a BRUKER D8-Focus Bragg Brentano X-ray powder di ractometer equipped with a Cu sealed tube (λ = 1.54178Å) at 40 kV and 40 mA. Thermogravimetric analyses (TGA) were conducted on a

TGA-50 (SHIMADZU) thermogravimetric analyzer. Gas sorption measurements were conducted using a Micrometritics ASAP 2420 system at various temperatures. Inductively Coupled Plasma Emission - Mass Spectrometry (Laser Ablation) was carried out by Perkin Elmer DRCII ICP-MS with both solution and laser ablation capabilities.

2.2.2 Ligand Synthesis

Step 1. Synthesis of 2,4,6-tri-*p*-tolyl-1,3,5-triazine

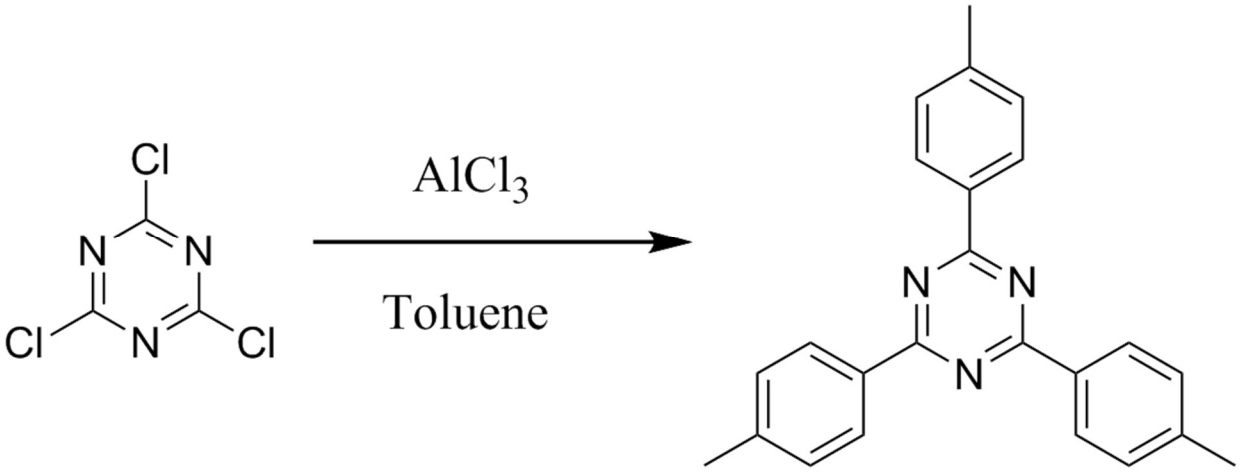

Scheme II-1 Synthesis of 2,4,6-tri-*p*-tolyl-1,3,5-triazine

20 g anhydrous $AlCl_3$ was added into a 250 mL three-connected flask containing 50 mL dry toluene. The temperature is increased to 60^oC under inert atmosphere. 8.3 g cyanuric chloride was added in three portions and the mixture was allowed to stir for 1 hour. The resulting red sticky oil was then cooled down and poured into 500 mL ice water mixture to terminate the reaction. The aqueous phase was extracted with chloroform for three times. The organic phases were combined and dried with $MgSO_4$. Methanol was added into the organic phase and the mixture was allowed to stay in 4oC fridge for overnight. The resulting solid was collected by filtration and was recrystalized from

refluxing toluene to afford white needle-like crystalline product. ^{1}H NMR (300 MHz, CDCl3): δ = 2.46 (s, 9 H), 7.35 (d, 6 H), 8.64 (d, 6 H).

Step 2. Synthesis of H_3TATB

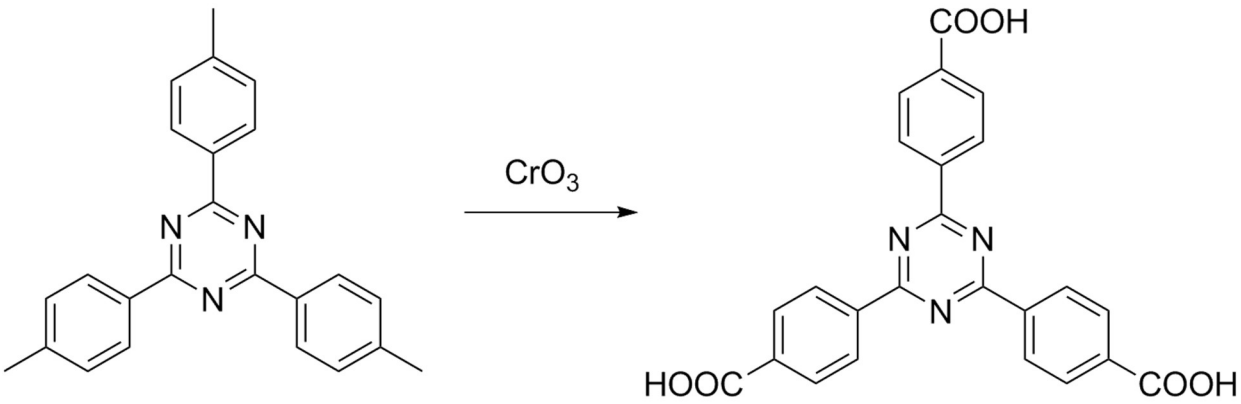

Scheme II-2 Synthesis of H_3TATB

2.78 g 2,4,6-tri-p-tolyl-1,3,5-triazine was dissolved in 70 mL acetic acid. Then 4.4 mL concentrated sulfuric acid and 4.8 mL acetic anhydride was added and the mixture was stirred at 0^{o}C. 7.2 g chromium trioxide was added and the mixture was stirred at room temperature for 12 h. 300 mL ice cold water was added to quench the reaction and the solid was filtrated. The solid was dissolved in 200 mL 2M NaOH solution. The unreacted material was removed by filtration. The clear greenish solution was then acidified with 10% HCl solution to give white crude product (until pH<3). The crude product was filtered, dried, and purified by recrystallization from reflux DMF. The pure product was a white crystalline solid. ^{1}H NMR (300 MHz, DMSO): δ = 8.20 (d, 6 H), 8.85 (d, 6 H), 13.35 (s, 3 H).

Step 3. Synthesis and activation of PCN-333-Cr(III)

$FeCl_3$ (60 mg), H_3TATB (60 mg), DEF (10 mL) and TFA (0.5 mL) were mixed in a 20 mL vial. The solids were supersonically dissolved and the vial was heated at 150ºC for 12 hours. The resulting solid was centrifuged and washed with anhydrous DMF for several times. 10 mL of anhydrous DMF was added into the vial and the mixture was degassed with nitrogen for 2 hours. 120 mg $CrCl_2$ was added into the vial in a glove box. Then the vial was heated at 85ºC for about 30 minutes until all of the solids turned green. Then the vial was centrifuged and transferred into the glove box to discard the mother liquor followed by rinsing with anhydrous DMF for three times. The vial was taken out of the glove box and rinsed with DMF twice in the air. For sample activation, the sample was rinsed with acetone twice, dried at 85ºC and activated at 150ºC for 5 hours.

Step 4. Stability test

60 mg solid was suspended in 10 mL aqueous solution at different pH values for 24 hours under room temperature. The solid was collected by centrifuge and was rinsed by acetone three times, dried at 85 ºC, and activated at 150 ºC for 5 hours.

Step 5. Preparation of PEI-incorporated PCN-333-Cr(III) and PEI-incorporated PCN-333-Fe(III)

60 mg activated PCN-333-Cr(III) was suspended in anhydrous dichloromethane (5mL) and 300 mg PEI was slowly added in the slurry. The mixture was well mixed by gentle shaking for 20 minutes. The solid was separated by centrifuge and the excess PEI was washed by dichloromethane. The sample was first dried under vacuum and activated at 80 ºC for 1 hour. PEI-incorporated PCN-333-Fe(III) was obtained in the same manner as PEI-incorporated PCN-333-Cr(III).

2.3 Results and Discussion

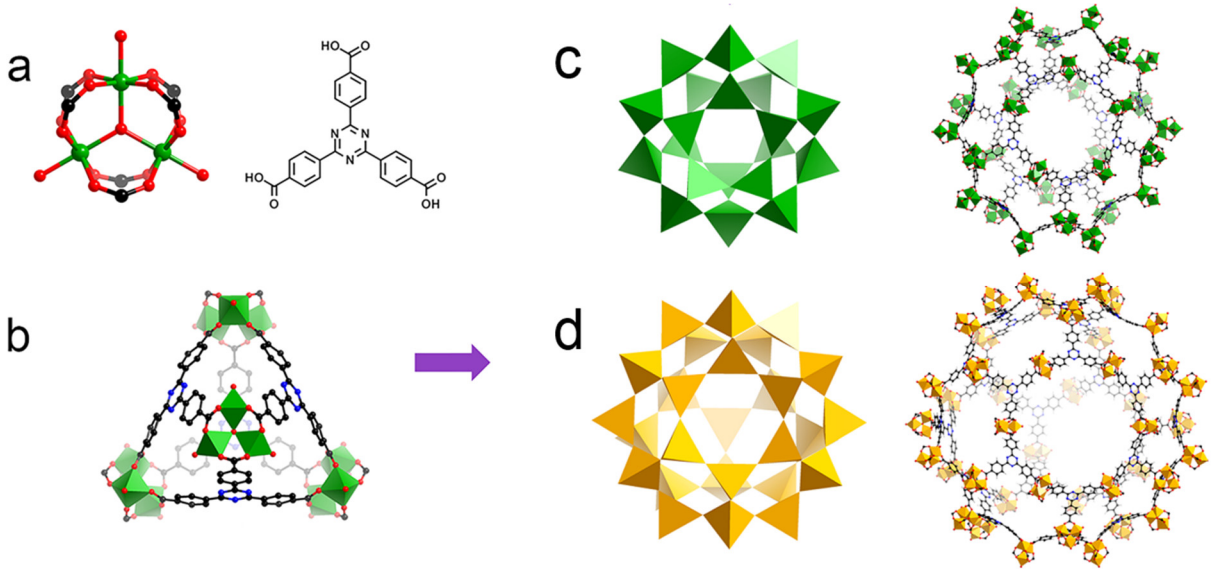

Figure II-1. Structure and cavity of PCN-333. (a) PCN-333 is composed of trimeric clusters and TATB ligands with (b) supertetrahedron as supermolecular building blocks. (c) The small cage with diameter of 4.2 mm and (d) the large cage with diameter of 5.5 nm.

MOFs constructed with divalent metal ions have been demonstrated to be good templates for complete metal metathesis due to the thermodynamic and kinetic lability of their coordination bonds.[10, 165-171] The reduction of high valence metal in SBUs can labilize the robust MOF, which will provide possibility for complete metathesis with a robust MOF template. There are several prerequisites for this process to take place: (1) the metal ions of the framework are in their high oxidation state and can be readily reduced under mild condition; (2) the reductant will not cause harsh conditions after oxidation (for example, very low/high pH values); (3) the oxidation potential of the oxidant is much higher than the reduction potential of the reductant, resulting in an irreversible redox reaction. In the practical case, PCN-333-Fe(III) is composed of

oxidative Fe(III) species while $CrCl_2$ matches the prerequisites to be a suitable reductant. The M^{3+}/M^{2+} redox potentials for Fe and Cr in aqueous solutions are: 0.77V (Fe), -0.42V (Cr).[172] The large potential difference indicates that redox reaction can irreversibly take place between Fe(III) and Cr(II) as indicated in eq. (1):

$$\mathbf{Fe^{3+} + Cr^{2+} \rightarrow Fe^{2+} + Cr^{3+}} \qquad (1)$$

Driven by the concentration gradient, the metal metathesis between Fe(II) in the intermediate framework and Cr(II) in the solution is thermodynamically and kinetically favorable.

Freshly prepared PCN-333-Fe(III) was dispersed in a solution of $CrCl_2$ in dry N,N-dimethylformamide (DMF) at 85°C under the protection of N_2. The color of the solid turned gradually from reddish brown to deep green (Figure II-2). The complete metathesis of Fe by Cr was obtained after 30 minutes as confirmed by inductive coupled plasma mass spectroscopy (ICP-MS) and energy-dispersive X-ray spectroscopy (EDS) (Figure II-

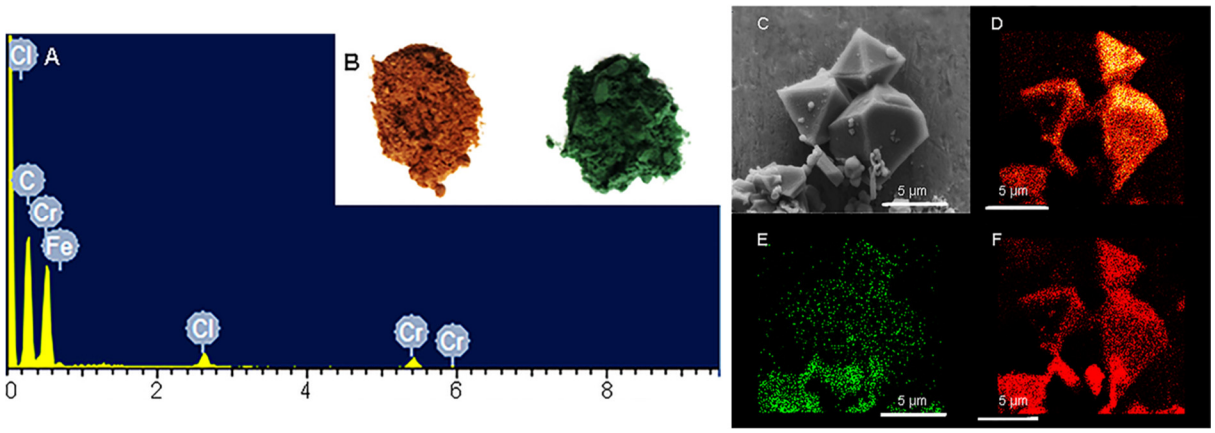

Figure II-2. SEM-EDS analysis of PCN-333-Cr(III). (A) The EDS spectrum of PCN-333-Cr(III); (B) PCN-333-Fe(III) on the left and PCN-333-Cr(III) on the right; (C) SEM images of PCN-333-Cr(III); elemental mappings of (D) C, (E) Cr, and (F) O from EDS analysis on PCN-333-Cr(III).

2, Table II-1). The SEM-EDS mapping with 4,000,000 counts results indicated that Cr, C, O and Cl were uniformly distributed on the crystal surface (Figure II-2). After that, the solids were washed with DMF three times in the air exposure to guarantee that all of the Cr(II) ions in the framework were oxidized to Cr(III), which was verified by X-ray photoelectron spectroscopy (XPS). The crystallinity of the metathesized product was maintained and recognized to be isostructural with PCN-333-Fe(III) as shown in the powder X-ray diffraction patterns (Figure II-3). The surface area and porosity of the metathesized product was also preserved based on the isotherms of N_2 adsorption measurements (Figure II-3). This reaction condition is optimum since higher or lower temperature with longer or shorter reaction time will either yield partially metathesized material or cause structure decomposition and porosity loss.

The reductive labilization-metathesis process was facilitated in the PCN-333 system for several structural characteristics. First, the microcrystalline and mesoporous nature of PCN-333 allows the metal ions to diffuse efficiently into the inner cavity of the framework. Besides, the trimeric clusters in PCN-333 are able to accommodate both di- and trivalent metal ions by varying charges of the terminal ligands, the bridging oxygen atoms, and/or the number of counterions.[162] Furthermore, the usage of the anhydrous reaction solvent decelerated the hydrolysis of Cr(III) species. The absence of acidic

condition contributes to the structural intactness of the intermediate MOF composed of fragile Cr(II)-O bond.

Table II-1. ICP-MS results of each metathesis.

Metal salt	Template	Temperature /ºC	Reaction time (h)	M1 : M2
$CrCl_2$	PCN-333(Fe)	85ºC	0.5	Cr : Fe 12: 1
$CrCl_3$	PCN-333(Fe)	150ºC	12	Cr : Fe 3.44: 1
$CrCl_2$	PCN-333(Sc)	85ºC	12	Cr : Sc 1 : 2.26

In order to exclude the possibility that the metathesis of PCN-333-Fe(III) with $CrCl_2$ circumvented the reductive labilization mechanism, a redox inert isostructural framework PCN-333-Sc was synthesized as a template to metathesize with $CrCl_2$. If the Cr(II) species were hypothesized to metathesize with Fe(III) ions in the framework directly without undergoing redox reaction, complete metal metathesis should also be observed in the system of PCN-333-Sc and Cr(II) since the Sc(III)-O coordination bond is not as robust as the Fe(III)-O bond. The mixture of PCN-333-Sc and $CrCl_2$ in dry DMF was heated at 85ºC for 30 minutes. The EDS results showed that only one fifth of the scandium in the framework was exchanged with chromium (Table II-1). This observation suggests that the metathesis between PCN-333-Fe(III) and $CrCl_2$ should undergo reductive labilization-metathesis manner since a thermodynamically more labile

framework failed to generate complete metathesized product without reductive labilization.

According to Marcus Theory and some calculation results, the electron transfer between Fe(III) and Cr(II) in this case should undergo outer-sphere mechanism although the experimental evidence of this mechanism is still pursuing in our group. First of all, inner-sphere mechanism requires the dissociation of axial ligands from Fe(III) whereas outer-sphere mechanism does not include coordination bond dissociation. Since the dissociation of Fe(III)-ligand bond is thermodynamically and kinetically unfavorable, outer-sphere electron transfer mechanism is more reasonable. Moreover, based on calculations, the rate constant of the cross redox reaction between Fe(III) and Cr(II) in aqueous solution is nearly 3×10^7 M^{-1} S^{-1}, which is close to the rate constant of the well-known outer-sphere redox couples, for example, $[Fe(phen)_3]^{2/3+}$ (1.5×10^7 M^{-1} S^{-1}), and

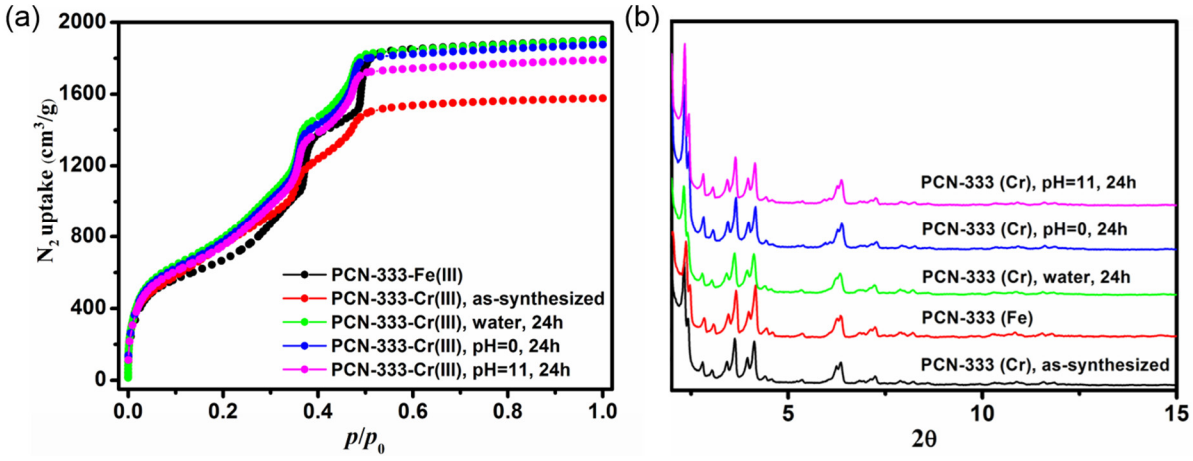

Figure II-3. N_2 isotherms (top) and PXRD patterns (bottom) of PCN-333-Fe(III), PCN-333-Cr(III), PCN-333-Cr(III) treated with water, pH = 0 and pH = 11.0 aqueous solutions for 24 hours.

much larger than the well-known inner-sphere redox couples, for example, $[Cr(H_2O)_6]^{2+}$+$[Co(NH_3)_5Cl]^{2+}$ (1.46×10^{-2} M^{-1} S^{-1}).[173] The metal ions are still in high-spin electronic configurations and their coordination field splittings in the framework or in the DMF solutions are similar to those in aqueous solutions which indicates that outer-sphere electron transfer is expected between these two metal ions. The calculation details are listed below:

$$k_{AB} = (k_{AA}k_{BB}K_{AB}f_{AB})^{1/2} \qquad _{AB} = \frac{(\log K_{AB})^2}{4\log\frac{k_{AA}k_{BB}}{Z^2}} \approx 1$$

k_{AB} = rate of cross reaction; k_{AA}, k_{BB} = self-exchange rates; K_{AB} = equilibrium constant of reaction; Z = collision frequency for hypothetical uncharged complex (10^{11}-10^{13} $M^{-1}s^{-1}$).

$$k_{AB} \approx (k_{AA}k_{BB}K_{AB})^{1/2}$$

$$Fe^{3+} + Cr^{2+} \rightarrow Fe^{2+} + Cr^{3+}$$

$$Fe^{3+} + e^- \rightarrow Fe^{2+} \qquad ^0 = 0.77\ V$$

$$Cr^{3+} + e^- \rightarrow Cr^{2+} \qquad ^0 = -0.40\ V$$

$$Fe^{3+} + Fe^{2+} \rightarrow Fe^{2+} + Fe^{3+} \qquad _{AA} = 4.5\ M^{-1}s^{-1}$$

$$Cr^{3+} + Cr^{2+} \rightarrow Cr^{2+} + Cr^{3+} \qquad _{BB} = 1 \times 10^{-5}\ M^{-1}s^{-1}$$

$$G^0 = -RT\ln K$$

$$G^0 = -nF\ E^0$$

$$RT\ln K = nF\ E^0 \qquad K = e^{\frac{nF\ E^0}{RT}}$$

$$K_{AB} = e^{38.94(0.77+0.40)} = 1.92 \times 10^{19}$$

$$k_{AB} = (1.92 \times 10^{19} \times 4.5 \times 1 \times 10^{-5})^{1/2} = 2.94 \times 10^{7}\ M^{-1}s^{-1}$$

As expected, the chemical stability of PCN-333-Cr(III) was much enhanced compared with PCN-333-Fe(III). Suspended in water, HCl aqueous solution (pH = 0) and NaOH aqueous solution (pH = 11.0) at room temperature for 24 hours, PCN-333-Cr(III) maintained structural integrity without appreciable loss of crystallinity as confirmed by PXRD measurements (Figure II-3). In contrast, PCN-333-Fe(III) was only stable in aqueous solutions at pH ranging from 3.0 to 9.0. To demonstrate the intactness of porosity, N_2 isotherms were conducted before and after each treatment. The results indicated that the void volume accessibility, the characteristic mesoporous adsorption patterns and the pore size distributions of PCN-333-Cr(III) after each treatment was unequivocally preserved. Remarkably the samples after each treatment even showed higher total adsorption amount than the as-prepared PCN-333-Cr(III). That is probably because some insoluble Cr(III) compounds, generated during metal metathesis and trapped in the pores, were removed upon the above-mentioned treatments.

The above results have clearly demonstrated that employing kinetically inert metal ions is an efficient strategy for constructing ultrastable MOFs with high porosity. Since the association-dissociation equilibrium of metal-ligand coordination bond always exists, coordination bonds in a MOF also undergo association-dissociation process. In the aqueous solution, carboxylate ligand substitution around metal ions with other ligands

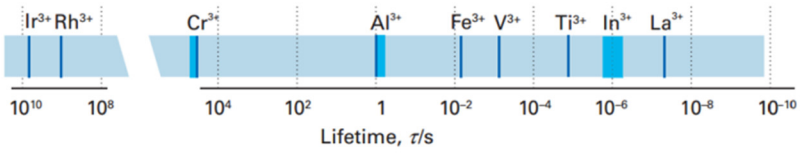

Scheme II-3. Characteristic lifetimes for exchange of water molecules in trivalent aqua complexes.

from the solution, for example, water or hydroxyl group, may take place, which could lead to the breakdown of MOF structure. For two metal ions with the same valence, ligand substitution rate of the kinetically inert species is far slower than that of the labile counterpart.[172] As shown in Scheme II-3, the ligand exchange rate of Cr(III) in aqueous solutions is more than 10^{10} times slower than that of Fe(III) species, which is believed to be the key factor that contribute to the superior chemical stability of Cr(III)-MOFs compared with other MOFs based on trivalent species. Meanwhile, the slow Cr-ligand dissociation rate also decreases the hydrolysis rate of the carboxylate ligand which also contributes to the improvement of MOF stability.

By taking advantage of the superior chemical stability of PCN-333-Cr(III), alkylamine was incorporated in PCN-333-Cr(III) aiming to improve the CO_2 adsorption capacity. Branched polyethylenimine (PEI, Mw = 800) was selected for the high density

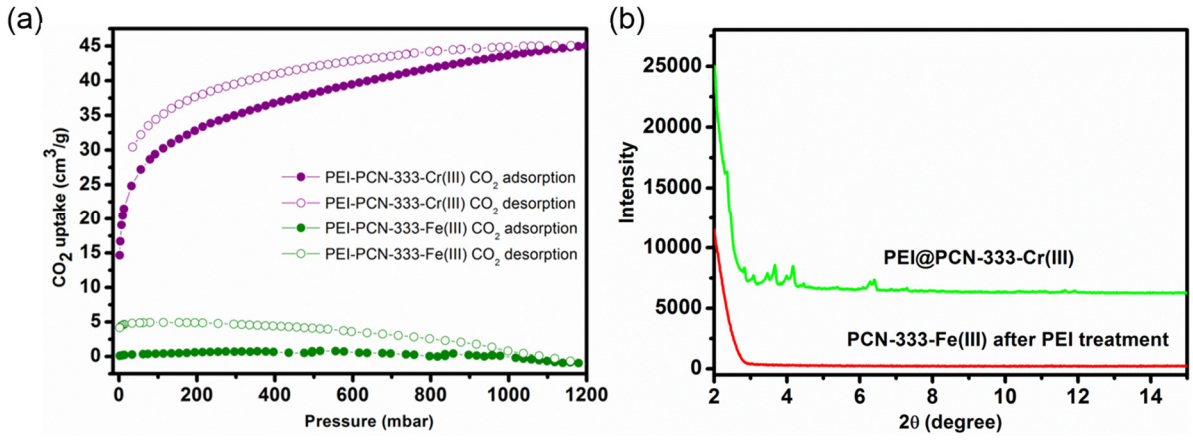

Figure II-4. (a) CO_2 adsorptions of PEI-incorporated PCN-333-Cr(III) and PEI-incorporated PCN-333-Fe(III). (b) PXRD patterns of PEI-incorporated PCN-333-Cr(III) and PEI-incorporated PCN-333-Fe(III).

of amine groups on each molecule. After PEI treatment the solid maintained its crystallinity with CO_2 adsorption capacity of 8.4 wt% at 1 bar (Figure II-4). In contrast, PCN-333-Fe(III) completely lost its crystallinity and porosity after PEI treatment according to the PXRD pattern and N_2 adsorption measurement (Figure II-4).

2.4 Conclusion

In conclusion, we reported a reductive labilization-metathesis route for the construction of an ultrastable mesoporous Cr(III)-MOF from a robust iron-based MOF template. The involvement of redox chemistry has switched a thermodynamically and kinetically forbidden process into a feasible one. The whole process includes (1) reduction of Fe(III) on the framework backbone to Fe(II); (2) metal metathesis between Fe(II) and Cr(II); (3) oxidation of Cr(II) in the framework to Cr(III). The presence of Fe(II) intermediate was proved by incomplete metathesis of PCN-333-Sc exchanged with $CrCl_2$. After metathesis, PCN-333-Cr(III) has demonstrated unprecedented chemical stability in aqueous solutions at pH 0 to 11.0 whereas PCN-333-Fe(III) can only survive in solution at pH 3.0 to 9.0. Significantly, PCN-333-Cr(III) is robust enough to bear the harsh condition of alkylamine solution, displaying high CO_2 adsorption capacity after PEI incorporation. Overall, the method we represent here demonstrated a new platform to synthesize ultrastable MOFs with high porosity for practical applications.

CHAPTER III

COUPLING TWO ENZYMES INTO A TANDEM NANOREACTOR UTILIZING A HIERARCHICALLY STRUCTURED MOF[3]

3.1 Introduction

During the course of evolution, nature has developed an ingenious series of multi-enzymatic systems to catalyze cascade reactions in the microenvironment of a cell.[174] In mitochondria, for instance, eight enzymes are involved in the citric acid cycle, catalyzing a controlled metabolism of sugars, fats and proteins and a highly effective production of ATP with minimal consumption of energy.[174-176] Inspired by the biosynthetic efficiencies of nature and in the search for more sustainable alternatives to today's ways of producing chemicals, scientists have tried to couple multiple enzymes for synthesis in a cascade manner.[174, 177] Specifically, in order to prevent the fragile enzymatic catalytic processes from undesired or toxic conditions, various enzymatic cascade nanoreactors have been developed based on porous materials such as phospholipid liposomes, polymersomes and mesoporous silica.[178-182] Although they demonstrated enzymatic reactivity, their catalytic performances were still far from satisfactory for any real applications. A major problem is that a high enzyme encapsulation capacity, which is critical to fulfill their desired functions, is not achievable in these materials.[179] Furthermore, the weak mechanical stability of liposomes, the poor permeability of the polymersome membrane and the severe enzyme leaching from mesoporous silica materials in cyclic uses are limiting

[3] Reproduced with permission from "Coupling two enzymes into a tandem nanoreactor utilizing a hierarchically structured MOF" by Lian, X.; Chen, Y.-P.; Liu, T.-F.; Zhou, H.-C. *Chem. Sci*., **2016**, *7*, 6969-6973, copyright 2016 by Royal Society of Chemistry.

factors due to the nature of the materials.[134, 181] Therefore, searching for more promising materials for enzyme encapsulation and coupling is highly desirable.

Metal–organic frameworks (MOFs) are an emerging class of porous materials with a vast application potential.[38, 133, 153, 156, 183, 184] It has been established that cage-containing MOFs (cageMOFs) always act as efficient molecular traps affording strong interactions between the framework and the encapsulated moieties;[132, 138, 154, 185-192] especially in one case single enzyme encapsulation was achieved in a hierarchical mesoporous MOF, leading to a record high enzyme encapsulation capacity and excellent catalytic performances.[134] In this work the same design approach is applied to deal with a much more sophisticated problem—coupling two enzymes in a tandem manner with a precise control of the distribution of each enzyme in the nanoreactor. To achieve this aim, a novel hierarchical mesoporous MOF, PCN-888, which contains three types of cages with different sizes, is rationally designed and synthesized. The largest cage of PCN-888 accommodates one GOx while the medium cage accommodates one HRP. A stepwise encapsulation with a specific encapsulation order (GOx first, then HRP) is a key operation to achieve the bi-enzyme coupling in PCN-888. The smallest cage is too compact for either enzyme, thus it is left empty as a diffusion pathway for substrates and products. PCN-888 demonstrates not only a very high enzyme loading but also a negligible enzyme leaching, whereas the catalytic activity of the encapsulated enzymes is well maintained. Moreover, this nanoreactor shows a convincing reusability and outstanding stability against the digestion of trypsin, indicating its potential applications for *in vitro* or *in vivo* studies.

3.2 Experimental Section

3.2.1 Materials and Instrumentation

Aluminum chloride hexahydrate ($AlCl_3 \cdot 6H_2O$), anhydrous aluminum chloride, chromium(VI) oxide (CrO_3), 2,2'-azino-bis(3-ethylbenzothiazoline-6-sulphonic acid) diammonium salt (ABTS) and N,N-diethylformamide (DEF) is purchased from Alfa Aesar. Phosphorous pentachloride (PCl_5), phosphorous oxochloride ($POCl_3$), glucose and horseradish peroxidase (HRP) is purchased from Sigma Aldrich. Glucose oxidase and trypsin is purchased from MP biomedicals. Synchrotron powder X-ray diffraction (PXRD) was carried out on a Bruker D8-Discover diffractometer equipped with a Mo sealed tube ($\lambda = 0.72768$Å) on the beamline 17-BM at the Advanced Photon Source, Argonne National Laboratory. Nuclear magnetic resonance (NMR) data were collected on a Mercury 300 spectrometer. Low pressure gas adsorption measurements were performed on an ASAP 2020 with the extra-pure quality gases. The UV-Vis absorption spectra were recorded on a Shimadzu UV-2450 spectrophotometer.

3.2.2 Ligand Synthesis

Step 1. Synthesis of heptazine-2,5,8-triamine polymer

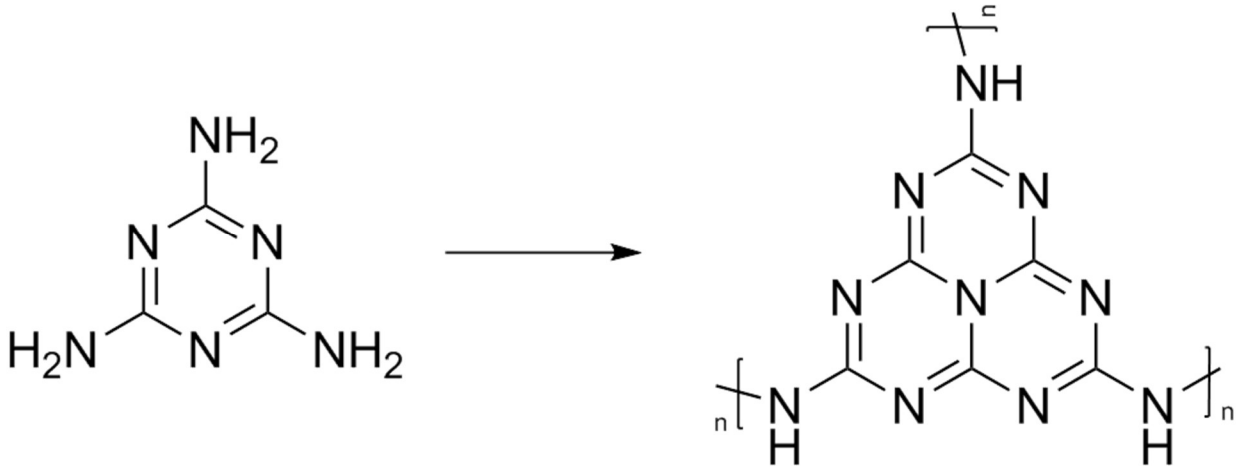

Scheme III-1. Thermo-polymerization of heptazine-2,5,8-triamine.

50 g of melamine was heated at 300^{o}C for 6 h. Then the temperature was raised to 450^{o}C and kept for another 2 h. The light-yellow solid was washed with 100 mL 10% KOH and boiled with concentrated HCl for 10 minutes. The solid was filtered and dried in air.

Step 2. Synthesis of potassium cyamelurate

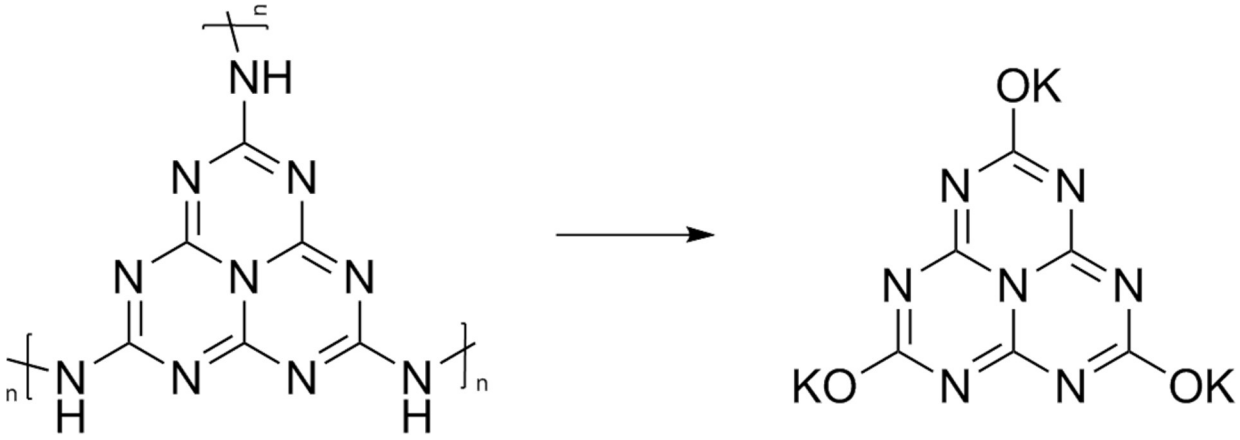

Scheme III-2. Synthesis of potassium cyamelurate.

25 g poly(heptazine-2,5,8-triamine) was refluxed with 500 mL 2.5 M KOH until all the solid were dissolved. Then the solution was concentrated to about 200 mL. The solution was cooled in ice bath and the solid was filtered. The filtration was concentrated again and another batch of product was collected by filtration. The product was combined and dried in air.

Step 3. Synthesis of heptazine-2,5,8-trichloride

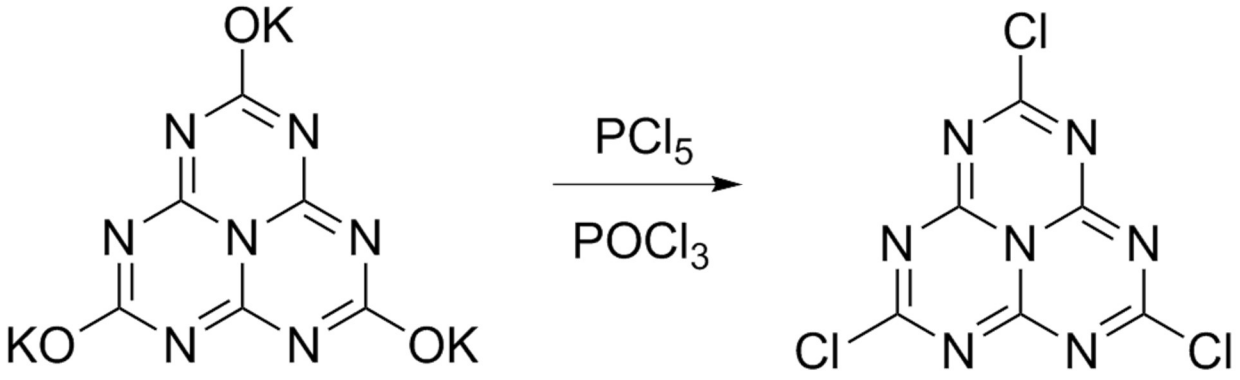

Scheme III-3. Synthesis of heptazine-2,5,8-trichloride.

3.87 g potassium cyamelurate and 8.64 g PCl_5 was charged in a Schlenk bottle. The mixture was heated at 130^{o}C under vacuum overnight. 70 mL $POCl_3$ was added to the solid mixture and refluxed for 6 hours. The color of the reaction slurry turned from white to yellow. The solvent was removed and the residue solid was washed with minimal amount of cold water. The yellow solid was dried in air.

Step 4. Synthesis of 2,5,8-p-tolyl-s-heptazine

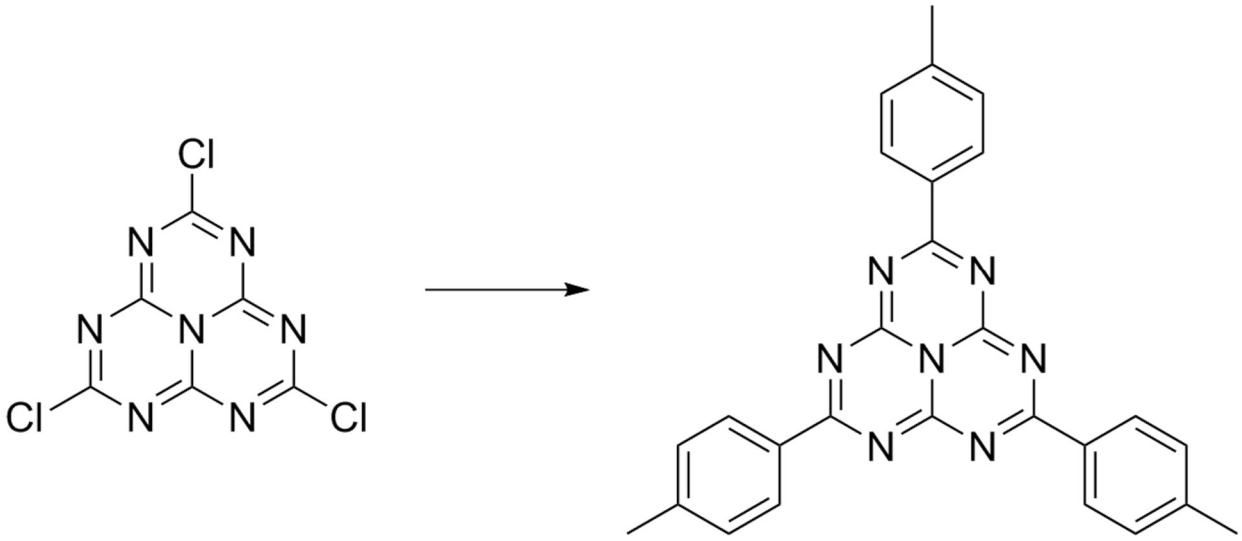

Scheme III-3. Synthesis of 2,5,8-p-tolyl-s-heptazine.

In a 100 mL Schlenk flask was charged 8 g anhydrous $AlCl_3$ and 20 mL anhydrous toluene. The mixture was heated to 60 ^{o}C under stirring. 3.2 g heptazine-2,5,8-trichloride was added to the flask in small portions over 20 minutes. The reaction mixture changed from yellow-green to dark red and white gas was generated. The reaction was kept at 60 ^{o}C for 30 minutes and it was cooled down to room temperature. The mixture was poured into ice water with rigorous stirring. The resulting yellow solid was filtered and washed

with water and cold THF. Yield: 1.5 g. ^{1}H NMR (300 Hz, Benzene), 2.017 (s, 3H), 7.024 (d, 2H), 8.854 (d, 2H).

Step 5. Synthesis of HTB ligand

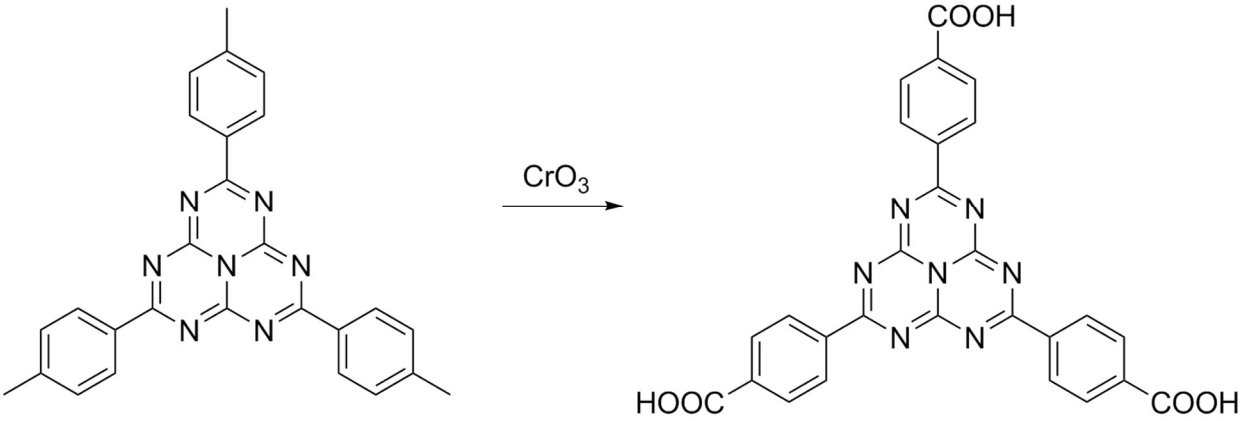

Scheme III-4. Synthesis of HTB ligand.

1 g 2,5,8-p-tolyl-s-heptazine, 20.5 g HOAc, and 1.23 mL H_2SO_4 was added in a 100 mL flask in ice bath. 2.03 g CrO_3 was added slowly to the flask. Then 1.35 g Ac_2O was added in. The flask was kept at 0ºC for 10 minutes and it was allowed to stay at room temperature overnight. The reaction mixture was poured into 300 mL deionized water and stirred for 1 hour. The solid was collected by centrifuge and washed with water for three times. The product was dissolved with 2.5 M KOH aqueous solution and the residue solid was removed by centrifuge. To the clear solution was added 6 M HCl until pH = 1. The product was collected by filtration and purified by recrystallization from DMF. Yield: 0.5 g, yellow solid. 1H NMR (300MHz, DMSO): 8.14 (d, 2H), 8.50 (d, 2H).

3.2.3 Synthesis of PCN-888

$AlCl_3$ $6H_2O$ (20 mg), HTB (10 mg) and TFA (0.1 mL) was dissolved in 2 mL DEF in a 4 mL Pyrex vial. The mixture was kept in a 135ºC oven for 10 hours. The yellow solid was collected by centrifuge. Yield: 4 mg.

3.2.4 Enzyme immobilization of PCN-888

12 mg glucose oxidase (GOx) was dissolved in 2 mL water. 20 mg horseradish peroxidase (HRP) was dissolved in 2 mL water. 4 mg as-synthesized PCN-888 was washed with water twice and dispersed in 1 mL water. 1 mL GOx solution was added to the MOF slurry and incubated at room temperature for 50 minutes. The solid was collected by centrifuge and washed with DI water twice. The MOF was dispersed in 1 mL water. 1mL HRP solution was added to the MOF slurry and incubated at room temperature for another 50 minutes. The solid was collected by centrifuge and washed with water twice. The supernatants were collected for the determination of the amount of immobilized enzymes in PCN-888. The uptake amount was determined by the bicinchoninic acid (BCA) method.[193]

3.2.5 Activation of PCN-888

Freshly prepared PCN-888 was washed with DMF for three times. The sample was evacuated with supercritical CO_2 in a Tousimis Samdri PVT-3D critical point dryer. Briefly, the DMF-containing sample was placed in the chamber and DMF was completely exchanged with liquid CO_2. After that the chamber containing the sample and liquid CO_2 was heated up around 40 °C and kept under the supercritical condition (typically 1300 psi) for 30 minutes. The CO_2 was slowly vented from the chamber at around 40 °C,

yielding porous material. The yellow solid was further activated by heating at 150°C for two hours.

3.2.6 The measurement of kinetic parameters of PCN-888-en/PCN-888-enR

ABTS and glucose are dissolved in 1mL 50 mM pH = 7 tris-HCl buffer solution to yield desired concentration of ABTS (10 mM) and glucose (0.6-9 mM) solution. MOF powder is added in the solution and the system is monitored by UV-vis spectrometer at 403 nm spontaneously. The measurement is stopped when the adsorption reaches plateau.

3.2.7 The measurement of kinetic parameters of free enzymes

The procedure is similar with that of MOF nanoreactors instead of the glucose concentration range (1-9 mM), GOx concentration (0.0141 μM,) and HRP concentration (0.05057 μM).

3.3 Results and Discussion

PCN-888 was obtained by a solvothermal reaction with $AlCl_3$ and a heptazine based tritopic ligand (HTB) at 135 °C. PCN-888 is isoreticular to PCN-333, which was shown earlier by our group.[134] High-resolution synchrotron powder X-ray diffraction (PXRD) collected at 17-BM, Argonne National Laboratory shows that PCN-888 is cubic with an exceptionally large unit cell length $a \approx 143$ Å (Figure III-1). PCN-333 crystallizes in the space group $Fd\bar{3}m$, therefore, the same space group was chosen to describe the isoreticular PCN-888. The corresponding structural model of PCN-888, with a formula of $[C_{54}H_{24}N_{14}O_{16}Al_3]$, was simulated based on the reported PCN-333 structure using Material Studio 6.0. Rietveld refinement was performed to examine the validity of the

structure model, which converged to an acceptable R_{wp} value of 0.0349, an R_{exp} of 0.0583 and an R_p of 0.0181 (Figure III-2).

The basic secondary building block of PCN-888 is a super tetrahedron, which consists of an aluminum trimeric cluster $Al_3(\mu_3\text{-}O)(OH)(H_2O)_2$ at the four vertices and HTB ligand located at the four faces, in a vertex sharing manner. The HTB ligands experience geodesic bending to form a domed structure in the framework, giving rise to a hierarchical porous structure with three types of mesoporous cages. Besides the super tetrahedral cage mentioned above, there are two additional hierarchal mesoporous cages in the PCN-888 structure. A smaller dodecahedral cage is composed of 20 super tetrahedra connected by vertex sharing with a pentagonal window of 2.5 nm. A larger hexacaidecahedral (hexagonal-truncated trapezohedral) cage is surrounded by 28 super tetrahedra with not only the 2.5 nm pentagonal windows, but also hexagonal windows of 3.6 nm. The large cages lie in a honeycomb-like arrangement in the [111] projection. The

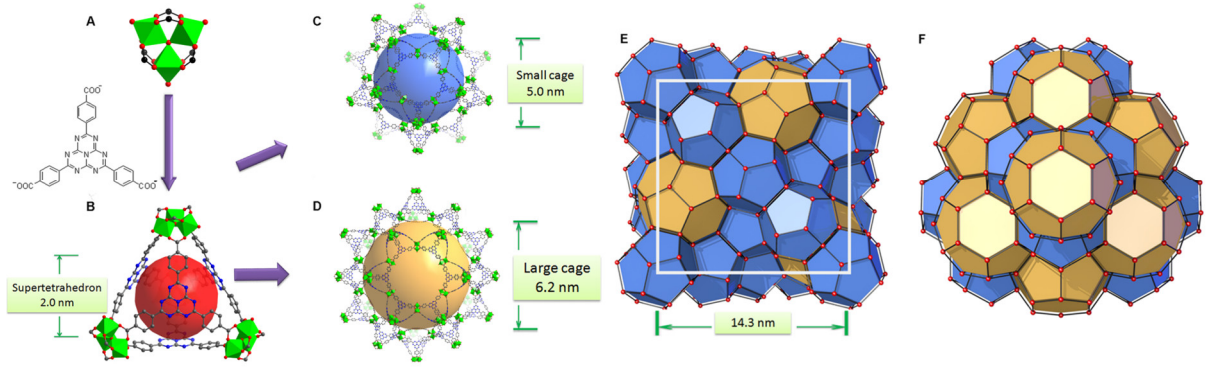

Figure III-1. Structure and topology of PCN-888. (A) The trimeric cluster and the HTB ligand to construct (B) a super tetrahedron; (C) the small cage and (D) large cage of PCN-888 composed of the super tetrahedron in a vertex sharing manner; (E) **mtn** topology with a cell diameter of 14.3 nm; (F) large cages in a honeycomb-like arrangement viewed from the [111] direction.

diameter of the inscribed sphere is 2.0 nm for the super tetrahedron cage, 5.0 nm for the dodecahedral cage and 6.2 nm for the hexacaidecahedral cage. The porosity of PCN-888 was determined by Ar adsorption at 87 K and N_2 adsorption at 77 K. It has a total Ar uptake of 3250 cm^3 g^{-1} and N_2 uptake of 2770 cm^3 g^{-1} (Figure III-2). The Brunauer–Emmett–Teller surface area is over 3700 m^2 g^{-1}. The two steep increases at $p/p_0 = 0.44$ and 0.56 on the adsorption branch of the Ar isotherms correspond to the filling of the

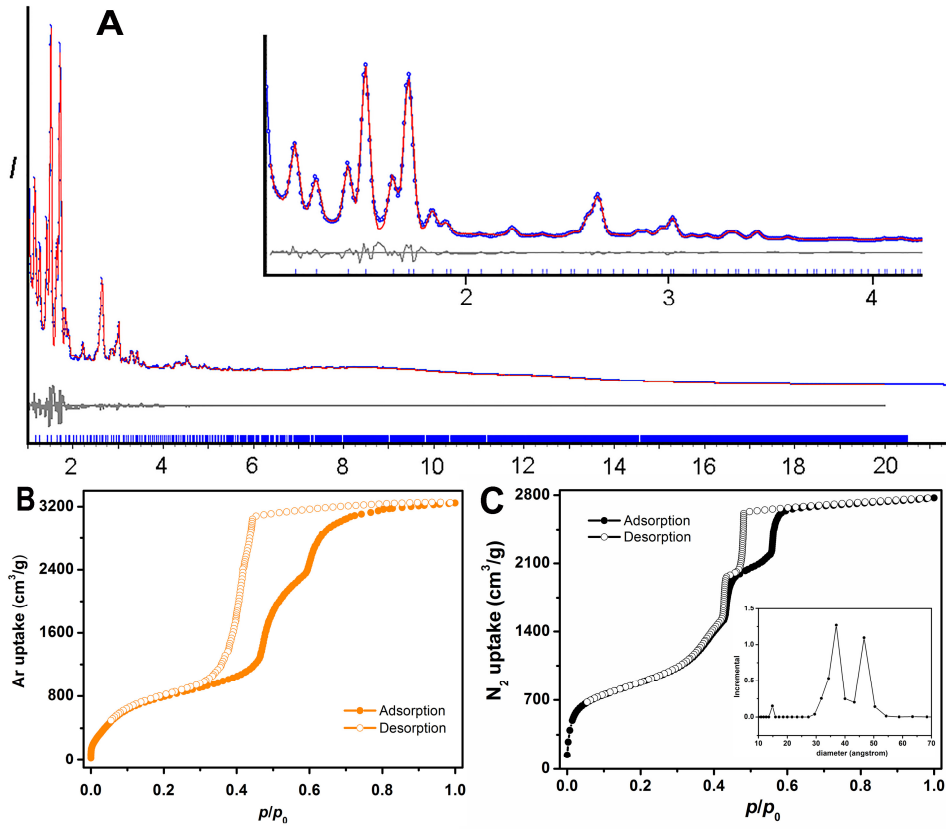

Figure III-2. Structure and porosity analysis of PCN-888. (A) Rietveld refinement patterns of PCN-888 using synchrotron PXRD data ($\lambda = 0.72768$ Å): observed (blue), calculated (red), and difference (grey) profiles are shown; the tick marks below the curves indicate Bragg positions. The X-ray diffraction pattern between 1.1° and 4.2° is magnified in the inset. The full pattern shows a precise match between the experimental PXRD data and those simulated from the proposed structure. (B) Ar isotherms of PCN-888 measured at 87 K. (C) N_2 isotherms of PCN-888 measured at 77 K. Pore size distribution obtained from the N_2 isotherm is displayed in the inset.

dodecahedral and the hexacaidecahedral cages of PCN-888, respectively. The experimental pore volume is 4.0 cm^3 g^{-1}. Such a high porosity is among the most porous materials reported in the literature and the hierarchical structure indicates that it is appropriate for constructing an enzymatic nanoreactor with an ultrahigh enzyme loading and low leaching.[134, 154, 185, 192]

Only one molecule of GOx (6.0 × 5.2 × 7.7 nm) can fit in the largest cage (6.2 nm) of PCN-888, while HRP (4.0 × 4.4 × 6.8 nm) can be accommodated in both the medium (5.0 nm) and large cages. Therefore, a stepwise encapsulation with the order → GOx → HRP is necessary to precisely control the distribution of GOx and HRP exclusively in the largest and medium cages, respectively. With the above order, PCN-888 demonstrated a GOx uptake capacity of 1.0 g g^{-1} and HRP uptake capacity of 2.0 g g^{-1}. The total enzyme encapsulation capacity was 300 wt%, which is the highest among all MOFs.[132, 134, 138, 188,

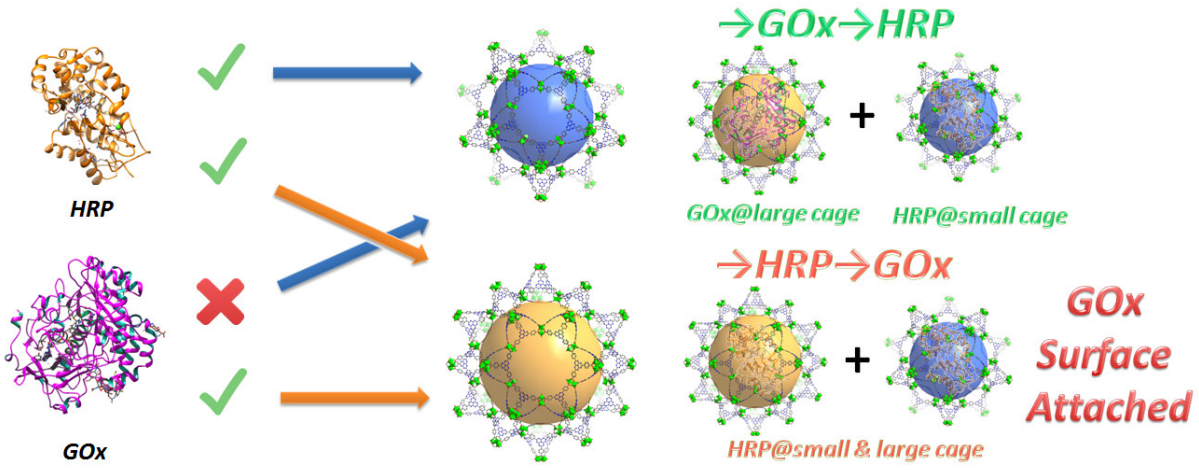

Figure III-3. Graphic representation of the results of the stepwise encapsulation of GOx and HRP with different orders.

[189, 194] In the following discussion the nanoreactor generated with the →GOx → HRP order is named PCN-888-en.

The porosity of PCN-888-en has dramatically decreased due to the residence of enzymes in pores. The total N_2 uptake of PCN-888-en was reduced to 400 $cm^3\ g^{-1}$ whereas the BET surface area dropped to 147 $m^2\ g^{-1}$. The pore size distribution analysis revealed that the pore size of PCN-888-en is predominantly around 1.4 nm, which corresponds to the cavity of the smallest pore (super tetrahedron), whereas the contributions from the two mesoporous cages of 5.0 nm and 6.2 nm in pristine PCN-888 disappeared. Consequently, we can conclude that the enzymes are residing in the mesoporous cages of PCN-888, while the smallest pore is left empty, which may provide a pathway for the diffusion of substrates into the framework. N_2 isotherms of GOx@PCN-888 and HRP@PCN-888 were also collected to prove the size selective incorporation of enzymes by different cages. The contribution from the medium cage was present on the

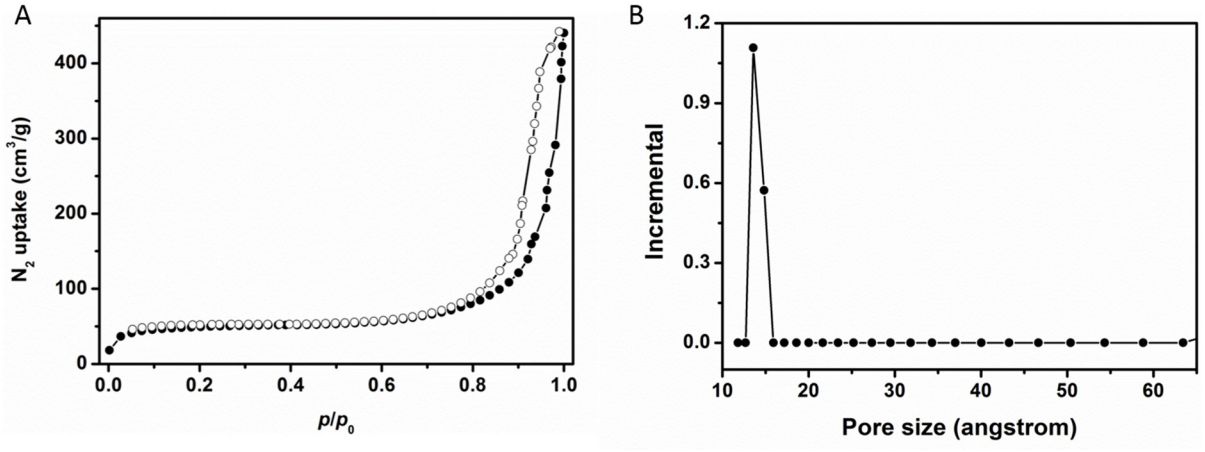

Figure III-4. N_2 isotherm of PCN-888-en (A) and the pore size distribution (B) derived from N_2 isotherm.

pore size analysis pattern of GOx@PCN-888 while the mesoporous porosity was fully occupied in the case of HRP@PCN-888.

When the order of enzyme encapsulation was reversed to →HRP → GOx, the HRP uptake was higher (2.5 g g ^{1}) whereas the GOx uptake was greatly compromised (0.07 g g ^{1}). The reversed order leads to only a surface attachment of GOx, as can be revealed from the negligible uptake amount, indicating that bi-enzyme coupling is not achieved. The nanoreactor generated with the order →HRP → GOx is named PCN-888-enR.

Table III-1. Kinetic parameters of GOx-HRP in free states, PCN-888-en and PCN-888-enR in the tandem reaction.

	K_m/mM	V_{max}/mM · s^{-1}	k_{cat}/s^{-1}
Free	9.44	1.02×10^{-3}	7.253×10^{4}
PCN-888-en	9.67	1.96×10^{-3}	2.411×10^{4}
PCN-888-enR	11.71	1.50×10^{-6}	7.946×10^{1}

GOx catalyzes the reaction between glucose and molecular oxygen, generating gluconolactone and hydrogen peroxide. Hydrogen peroxide is consumed in the conversion of ABTS to $ABTS^{\cdot+}$, catalyzed by HRP. The absolute reaction kinetics for this tandem reaction was obtained by monitoring the formation of $ABTS^{\cdot+}$ at 403 nm by UV-vis spectroscopy, instead of H_2O_2, since the rate of reaction catalyzed by GOx is slower

than that of HRP.[180] The catalytic performance of PCN-888-en was first examined. The apparent reaction rate (k_{cat}), substrate affinity (K_m) and maximum conversion rate (v_{max}) of PCN-888-en have proved the well maintained catalytic activities of the encapsulated enzymes in PCN-888. The design of only one enzyme residing in each pre-designed cage effectively prevents enzyme aggregation. Moreover, since large and medium cages are stacked in an ABAB layer fashion, the diffusion of substrates and intermediates has a very low barrier and short path, which facilitates the conversion of substrates. The catalytic performance of PCN-888-enR was also studied. It demonstrated a much worse catalytic performance than PCN-888-en, as displayed in Table III-1. This can be attributed to the much lower GOx loading in the material and larger diffusion barrier between GOx and HRP that are not adjacent to each other.

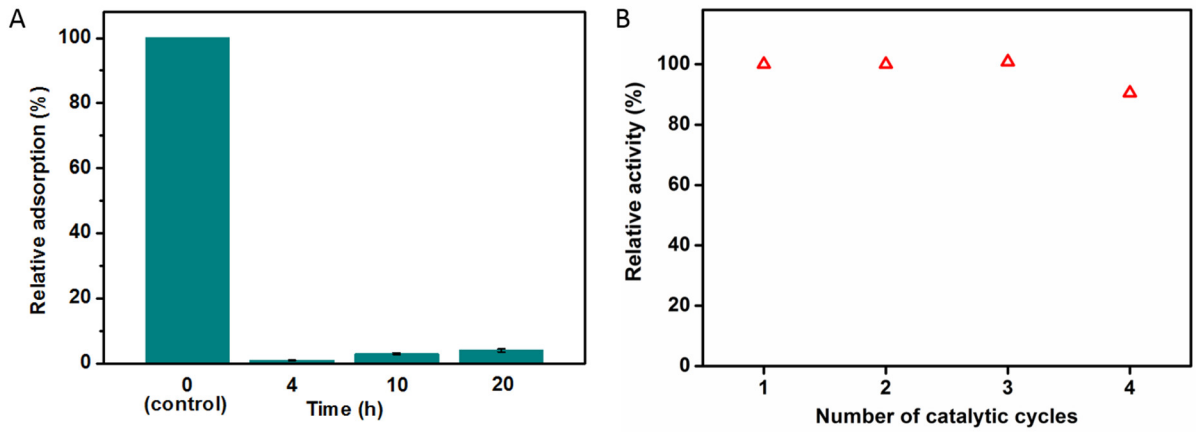

Figure III-5. (A) Leaching test of PCN-888 nanoreactor at 30, 60 and 120 minutes. The amount of leaching enzymes were determined by Thermo Scientific Pierce™ BCA protein assay. The 100% standard solution at 0 minute was composed of 0.14 μM GOx and 1.1 μM HRP in water and room temperature. (B) Reusability of PCN-888-en.

In comparison with many enzyme loaded silica materials, such as macroporous silica foams (MSF), immobilized enzymes always suffer activity loss, due to the partial protein unfolding or geometry disruption induced by the strong electrostatic interaction between the positively charged protein and negatively charged silica, however, PCN-888 is electrical neutral so the above mentioned issue no longer exists. For the enzyme loaded polymersomes, the encapsulated enzymes inevitably suffer from activity loss since organic solvents, such as tetrahydrofuran (THF), are always utilized in the enzyme encapsulation procedure. Moreover, the rate of reaction catalyzed by PCN-888-en is much faster than that of many polymersomes, in which the conversion of substrates can hardly reach a maximum rate within several hours, which is probably attributed to the higher enzyme encapsulation capacity of PCN-888 and the empty 2.0 nm cage of PCN-888 that greatly facilitate diffusion, in contrast to the poorly permeable polymersome membranes.[179]

The leaching of enzymes from PCN-888 was revealed to be negligible, indicating that PCN-888 can provide strong interactions between the cage and the immobilized moieties. As a result, the activity of PCN-888-en remained almost the same within four catalytic cycles, indicating its promising performance in multiple-cycle uses (Figure III-6). In a previous report, Ma and coworkers have demonstrated the presence of $\pi \quad \pi$ interactions between the immobilized enzyme and the conjugated ligands in a mesoporous cageMOF.[195] The HTB ligand in PCN-888 can form a large conjugated system between the heptazine core and terminal benzene rings, which should lead to a strong interaction with the immobilized enzymes. At the same time, the small window size of the cages also physically prevents the leaching of the enzymes from the framework, although the

enzyme has to somehow make its way into the cage, one possible way being unfolding and refolding.[195] In contrast, enzyme leaching of mesoporous silica materials, such as SBA-15, has proved to be significant even after one cycle, resulting in a severe reduction of the catalytic activity.[134]

The stability of enzymes in a cellular environment is extremely important for the widespread biomedical applications of enzymatic nanoreactors.[174] Digestion by a protease, such as trypsin, is a major deactivation pathway of enzymes *in vivo*.[140] PCN-888-en has retained almost all of its activity after treatment with trypsin at 37 °C for 60 minutes, whereas the free enzymes lost two thirds of their activity after the same treatment (Figure III-6). The protective effect of PCN-888 can be attributed to the small window openings of the enzyme-encapsulated cages, which makes the barrier of the immobilized enzymes approaching the active sites of trypsin extremely high.

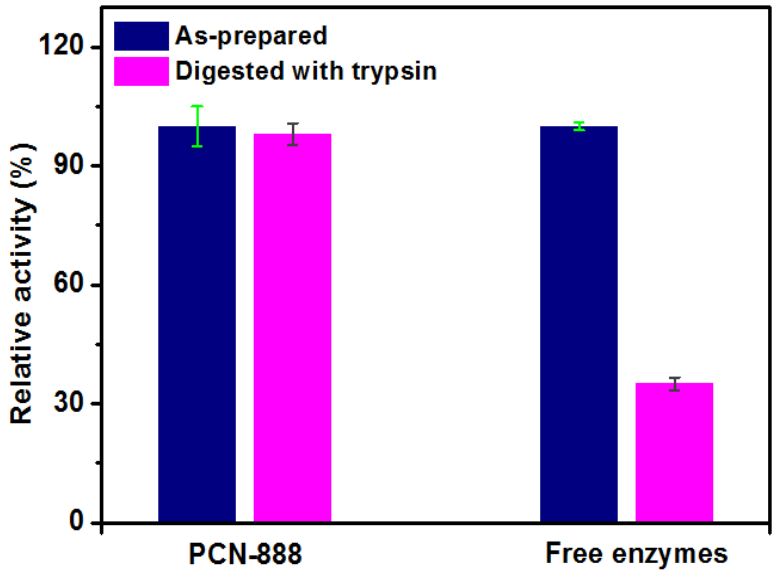

Figure III-6. Stability of PCN-888 nanoreactor compared with free enzymes incubated in an aqueous solution containing 1 mg/mL trypsin at 37 °C for 1 hour.

3.4 Conclusion

In summary, a novel hierarchical MOF, PCN-888, which possesses three types of mesoporous cages, is designed and synthesized for bi-enzyme coupling with a precise control of the enzyme distribution all over the material. The largest cage and the medium cage can only accommodate one molecule of GOx and HRP, respectively, indicating that a stepwise encapsulation procedure with a specific order (GOx first, then HRP) is a key operation to achieve the coupling. Control experiments demonstrate that bi-enzyme coupling failed to be established with a reversed encapsulation order. The high catalytic efficiency of the PCN-888 nanoreactor, good cycling performance as well as the protective effect of PCN-888 on the immobilized enzymes against trypsin digestion indicates that cageMOF tandem nanoreactors have the potential to be applied in more complex systems.

CHAPTER IV

HIGH EFFICIENCY AND LONG-TERM INTRACELLULAR ACTIVITY OF AN ENZYMATIC NANOFACTORY BASED ON METAL-ORGANIC FRAMEWORKS[4]

4.1 Introduction

The modulation of protein function in live cells is valuable in biotechnology and medicine.[196] Rescuing enzymatic activity can for instance provide therapeutic benefits for the many diseases associated with defective enzymes.[197] A general approach used to restore protein function involves genetic manipulation, whereby introduction of a gene into cells replaces its defective counterpart and insures the production of its protein product otherwise lacking. However, genetic manipulations are often problematic as they may inadvertently alter the genome of cells and lead to new diseases, including cancer.[198-202] To circumvent this issue, directly using protein supplementation may be preferable. However, proteins, in part due to their relative large size and hydrophilicity, do not readily penetrate cells. Proteins also have relatively short extra- or intra-cellular half-lives. If not produced directly inside a cell, proteins may therefore not reach the location where their activity is required, and, additionally, not produce a pro-longed effect because of their rapid degradation.

Addressing the problems associated with protein replacement has been the focus of intense research. Several techniques have been developed to enhance the cellular delivery of these macromolecules, for instance, protein PEGylation or encapsulation in liposomes, micelles or polymersomes, to improve transport properties and increase protein half-

[4] Reproduced with permission from "High efficiency and long-term intracellular activity of an enzymatic nanofactory based on metal-organic frameworks" by Lian, X.; Erazo-Oliveras, A.; Pellois, J.-P.; Zhou, H.-C. *Nature Commun.,* **2017**, *8*, No. 2075, copyright 2017 by Springer Nature.

lives.[149, 203-212] Another key idea is to increase protein stability by protecting these macromolecules from proteolytic degradation using encapsulation agents. In addition, encapsulation can help prevent immunological responses that may occur from exogenously introduced proteins.[204, 205, 213] These strategies have been successful in enhancing protein retention time in the circulatory system and in reducing undesired accumulation in the liver.[213-215] However, other challenges remain. For instance, encapsulated enzymes are often quiescent until they are released from their carrier and, because release is often inefficient, only a small fraction of the total available enzymatic activity is displayed at one time.[205] Surface modifications with chemical moieties such as PEG can also significantly alter protein structure and reduce activity.[216, 217] Overall, developing technologies that protect proteins from degradation while maintaining optimal protein function is presently highly desirable.

A possible solution to the problems currently associated with protein formulation may lie in the recently developed structures known as metal-organic frameworks (MOFs). MOFs are an emerging type of porous materials constructed from metal containing clusters and organic linkers. Due to the high porosity as well as structural and functional tunability, MOFs hold promises in a variety of applications, including gas storage/separation, catalysis, and sensing.[39, 47, 153, 218-221] Recently, enzymes have been loaded into the cavities of MOFs and immobilized enzymes tested thus far (e.g. Horseradish Peroxidase (HRP), Cytochrome C (Cyt c), etc.) have displayed robust *in vitro* activities.[132, 188, 222, 223] This indicates that proteins can fold properly in the cavities of MOFs and remain functionally active. MOF-immobilized enzymes have also shown extraordinary stabilities under denaturing conditions such as extreme heat, high or low

pH, and in the presence of organic solvents.[224, 225] Moreover, the cage formed by MOFs acts as a barrier against proteases, such as trypsin, and protects encapsulated proteins from proteolytic degradation.[141, 226]

The properties displayed *in vitro* by MOF-enzyme nanofactories are highly attractive. Although the biocompatibility of some MOF materials have been investigated in a number of reports, whether MOF-enzyme composites may serve as efficient nanofactories in living cells remains untested.[223, 227-236] Herein, we aimed to test the hypothesis that intracellular MOF nanofactories are capable of supporting an enzymatic activity beneficial to living cells for an extended period of time. To test this hypothesis, we chose PCN-333(Al) as a MOF platform due to its ultrahigh enzyme encapsulation capacity, facile fluorescence modification, and excellent chemical robustness in aqueous solutions. As a proof-of-concept study, we established that PCN-333 based nanofactories containing the antioxidant enzymes, superoxide dismutase (SOD) and catalase (CAT), protect cells from severe oxidative stress, a process involved in a large number of pathological states.[237-240] Remarkably, this protective effect was maintained for a minimum of a week despite the localization of the MOFs inside lysosomes, one of the most degradative environments in living cells.[241]

4.2 Experimental Section

4.2.1 Materials and Instrumentation

Aluminum chloride hexahydrate, N-bromosuccinimide (NBS), benzoyl peroxide (BPO), ethylenediamine, triethylamine, trifluoroborane etherate, N-hydroxysuccinimide, N-(3-Dimethylaminopropyl)-N′-ethylcarbodiimide (EDC), N,N-dimethylformamide

(DMF), tetrahydrofuran (THF), potassium carbonate, hydrochloric acid and sodium hydroxide were purchased from VWR. Carbon tetrachloride, superoxide dismutase (SOD), catalase (CAT), SOD assay, horseradish peroxide (HRP) and Amplex Red were purchased from Sigma Aldrich. Dulbecco's minimum essential medium (DMEM), 2-[4-(2-hydroxyethyl)piperazin-1-yl]ethanesulfonic acid (HEPES), Leibovitz's L-15 medium without cysteine (non-reducing L-15, nrL-15), 10% fetal bovine serum (FBS) and 1× penicillin/streptomycin (P/S), Hoechst 33342, Lyso Tracker red, SYTOX Blue and SYTOX Green were purchased from Thermo Fisher Scientific. TATB and m-BTB were prepared based on the previous report.[242] dfTAT used in this paper was resistant to peptide hydrolase and was prepared according to previous method.[243] pH 5.0 buffer is 50 mM sodium citrate buffer. pH 7.4 buffer is 50 mM HEPES buffer.

Synthetic manipulations that required an inert atmosphere (where noted) were carried out under nitrogen using standard Schlenk techniques. Powder X-ray diffraction (PXRD) was carried out on a Bruker D8-Focus Bragg-Brentano X-ray powder Diffractometer equipped with a Cu sealed tube (λ = 1.54178) at 40 kV and 40 mA. N_2 sorption isotherms at 77 K were measured by using a Micrometritics ASAP 2420 system with high-purity grade (99.999%) of gases. UV-Vis spectra were recorded on Shimadzu UV-2450 spectrophotometer. Fluorescence spectra were recorded on a Hitachi F-4600 spectrometer (Hitachi Co. Ltd., Japan) with Xe lamp as the excitation source at room temperature. ICP analysis was conducted on PerkinElmer NexION 300D instrument. Dynamic light scattering and Zeta potential were measured at 25 °C on a Zetasizer Nano ZS ZEN3600 analyser (Malvern Instrument Ltd, UK). Confocal laser scanning microscopy (CLSM) imaging was performed on an inverted epifluorescence microscope

(Model IX81, Olympus) was equipped with a heating stage maintained at 37 °C. Images were collected using a Rolera-MGI Plus back-illuminated electron-multiplying charge coupled device (EMCCD) camera (Qimaging). Images were acquired using bright-field imaging and three standard fluorescence filter sets: DAPI (excitation (Ex) = 350 ± 10 nm/emission (Em) = 440 ± 20 nm), RFP (Ex = 560 ± 20 nm/Em = 630 ± 35 nm) and FITC (Ex = 488 ± 10 nm/Em = 520 ± 20 nm). The images were processed with the SlideBook 4.2 software (Olympus) and ImageJ2. Inductively coupled plasma mass spectrometry (ICP-MS) was carried out on an Agilent 7700x series ICP-MS instrument. TEM images were taken on a transmission electron microscopy (JEOL JEM-2100F, Japan) operated at an acceleration voltage of 200 keV by dropping solution onto a carbon-coated copper grid.

HeLa (ATCC CCL-2), NIH3T3 (ATCC CRL-1658) and HDF (ATCC PCS-201-012) were grown in DMEM supplemented with FBS and P/S and kept at 37 °C in a humidified atmosphere containing 5% CO_2. Cell experiments are performed in quintuplicates for each condition and are repeated with three different batches of cells. Statistic tests are studied by multiple t tests method. HeLa cells are common vitro model for oxidative stress studies.[244-246]

4.2.2 Synthesis of BTB-Green

Step 1. Synthesis of dimethyl 2'-(bromomethyl)-5'-(4-(methoxycarbonyl)phenyl)-[1,1':3',1''-terphenyl]-4,4''-dicarboxylate (compound 1)

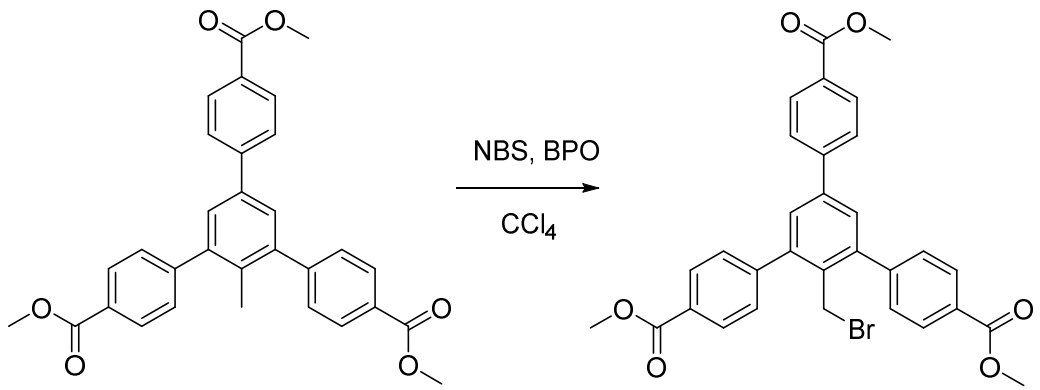

m-BTB **1**

3.68 g m-BTB, 1.35 g NBS and 50 mg BPO was dispersed in 45 mL CCl_4 and refluxed at 80^{o}C for 12 h. The precipitate was filtered and the filtrate was dried under vacuum. Compound **1** was obtained as light yellow solid. Yield: 100%.

Step 2. Synthesis of dimethyl 2'-(((2-aminoethyl)amino)methyl)-5'-(4-(methoxycarbonyl)phenyl)-[1,1':3',1''-terphenyl]-4,4''-dicarboxylate (Compound 2)

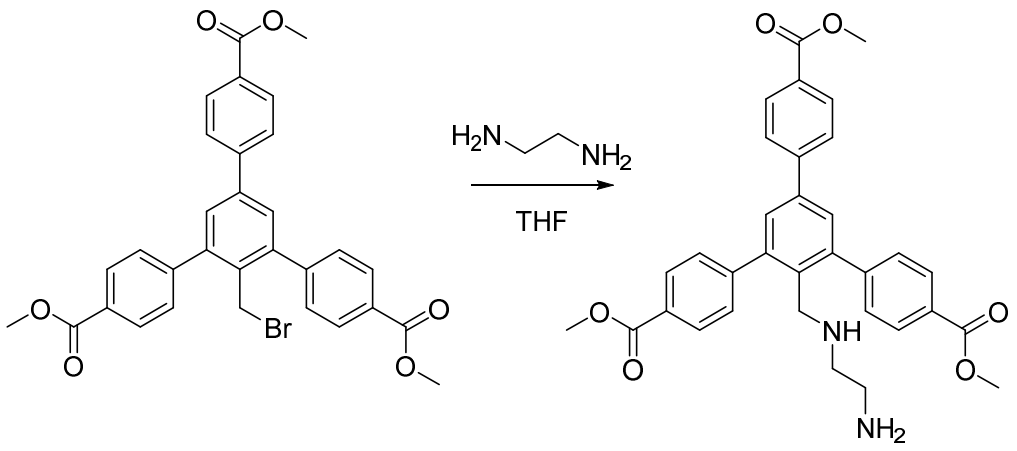

1 **2**

1.6 g compound **1** was dissolved in 60 mL THF. 1 mL ethylenediamine was added and the mixture was stirred under room temperature for 6 h. Saturated $NaHCO_3$ solution was added and the aqueous phase was extracted with CH_2Cl_2 for 3 times. The combined organic phase was dried over $MgSO_4$ and the solvent was removed under vacuum. Compound **2** was obtained as light yellow solid.

Step 3. Synthesis of 2'-(((2-aminoethyl)amino)methyl)-5'-(4-carboxyphenyl)-[1,1':3',1''-terphenyl]-4,4''-dicarboxylic acid (Compound 3)

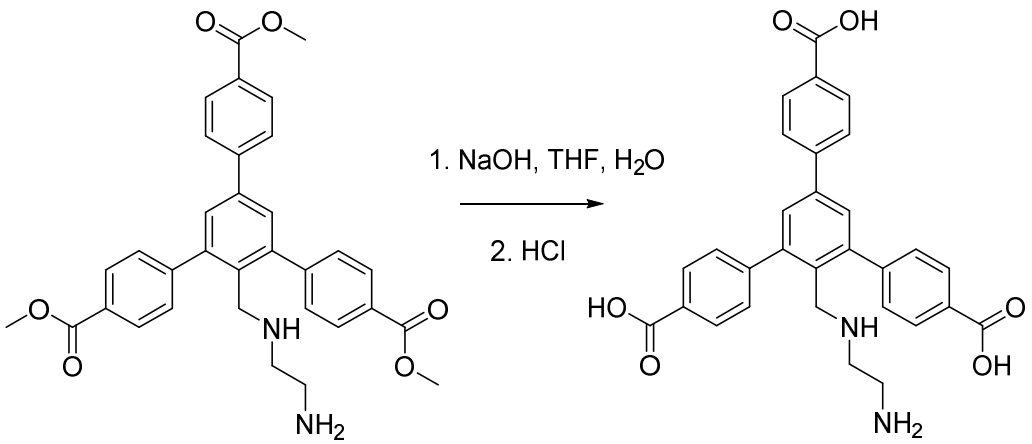

2 **3**

1.8 g compound **2** was dissolved in THF and 20 mL 2 M NaOH solution was added. The mixture was refluxed for 6 h after which THF was removed under vacuum. 6 M HCl was added until compound **3** precipitated as white solid, which was filtered and dried under vacuum.

Step 4. Synthesis of methyl 2-(4-(4,4-difluoro-1,3,5,7-tetramethyl-3a,4-dihydro-4l4-dicyclopenta[b,e]borinin-8-yl)phenoxy)acetate (Compound 2')

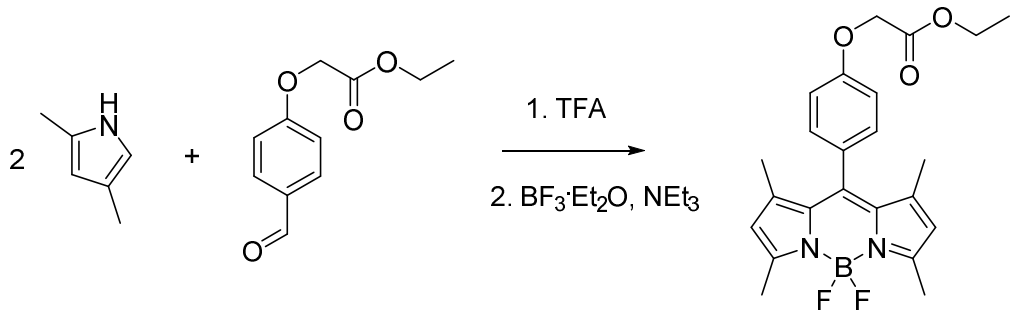

1' **2'**

0.95 g 2, 4-dimethylpyrrole and 1.04 g compound **1'** was dissolved in 150 mL THF. 3 drops of TFA was added and the mixture was stirred overnight at room temperature under darkness, after which 2 g DDQ dissolved in 50 mL THF was added and stirred for 30 minutes. 25 mL triethylamine was added to the mixture, and 31 mL BF3·Et2O was added over 30 minutes. The mixture was stirred for 6 h and compound 2' was obtained by column chromatography (CH_2Cl_2: hexanes = 1: 2) as an orange solid. Yield: 50%.

Step 5. Synthesis of 2-(4-(4,4-difluoro-1,3,5,7-tetramethyl-3a,4-dihydro-4l4-dicyclopenta[b,e]borinin-8-yl)phenoxy)acetic acid (Compound 3')

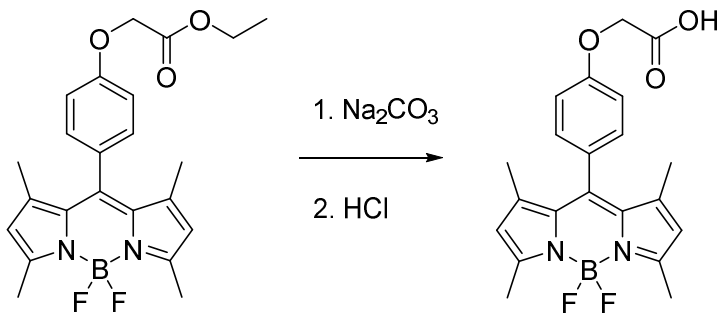

2' **3'**

0.4 g compound **2'** and 0.8 g K_2CO_3 was dissolved in a 1:1 mixture of THF and water. The solution was heated at 50ºC for 24 h, after which the solvent was removed under vacuum. Water was added to the solid and abstracted by CH_2Cl_2 for 3 times in order to remove the unreacted compound **2'**. The aqueous phase was added 1 M HCl until pH reached 7. Compound **3'** was obtained by filtration and vacuum drying as an orange solid. Yield: 99%.

Step 5. Synthesis of 2,5-dioxocyclopentyl 2-(4-(4,4-difluoro-1,3,5,7-tetramethyl-3a,4-dihydro-4l4-dicyclopenta[b,e]borinin-8-yl)phenoxy)acetate (Compound 4')

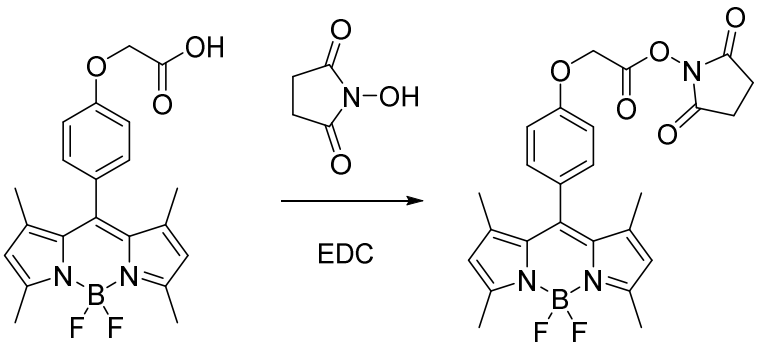

3' **4'**

350 mg compound **3'**, 200 mg N-hydroxysuccinimide and 340 mg EDC was suspended in 20 mL CH_2Cl_2 under N_2 atmosphere. The mixture was stirred at room temperature for 12 h and diluted by 200 mL 1:1 CH_2Cl_2/H_2O. The organic phase was dried and compound **4'** was obtained as an orange solid. Yield: 100%.

Step 6. Synthesis of 5'-(4-carboxyphenyl)-2'-(((2-(2-(4-(4,4-difluoro-1,3,5,7-tetramethyl-3a,4-dihydro-4l4-dicyclopenta[b,e]borinin-8-yl)phenoxy)acetamido)ethyl)amino)methyl)-[1,1':3',1''-terphenyl]-4,4''-dicarboxylic acid (BTB-Green)

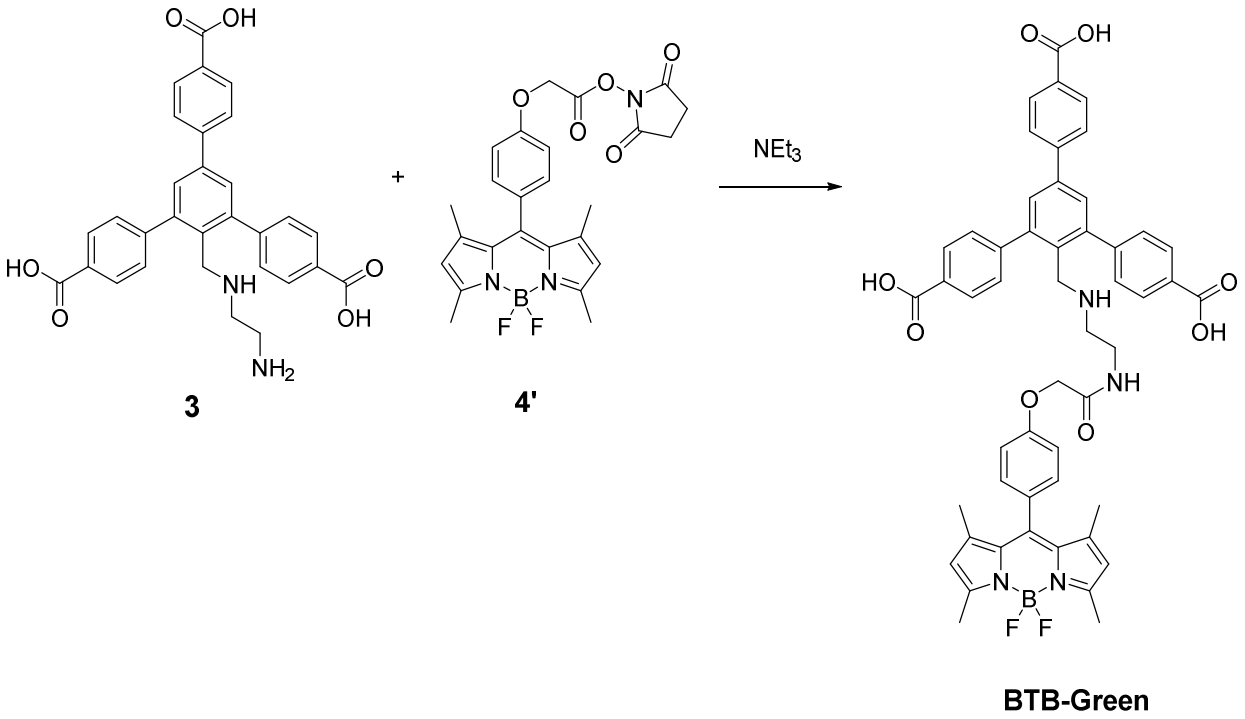

510 mg compound **3** and 495 mg compound **4'** was dissolved in 20 mL DMF and 1mL triethylamine was added. The mixture was stirred at room temperature for 12 h and diluted with 100 mL water. 1 M HCl was added until pH reached 4. **BTB-Green** was obtained by filtration and vacuum drying as an orange solid. Yield: 100%. ESI+: 891.3371.

4.2.3 Synthesis of NPCN-333

10 mL DMF solution of $AlCl_3 \cdot 6H_2O$ (1.5 mg/mL), 5 mL DMF solution of TATB (1 mg/mL), 15 mL DMF and 50 μL TFA was mixed and heated at 95ºC for 24 h. NPCN-333 was collected by centrifugation.

4.2.4 Synthesis of FNPCN-333

30 mg NPCN-333 was dispersed in 5 mL DMF in which was added 5 mL 10 mg/mL DMF solution of BTB-Green. The mixture was kept in 85ºC oven for 4 h and the solid was collected by centrifugation. The determination of the amount of metathesized ligand was conducted by digesting the obtained solid in HCl, dried under vacuum and dissolved in deuterated DMSO for NMR analysis. The ligand ratio of **BTB-Green**/TATB is 1:6.

4.2.5 Stepwise encapsulation of SOD and CAT on FNPCN-333

Stock solutions of SOD (5 mg/mL) and CAT (5 mg/mL) were prepared by dissolving SOD and CAT in deionized water, respectively. 1 mg FNPCN-333 was suspended in water in which 1 mL CAT stock solution was added. The mixture was vortexed for 20 minutes and the solid was collected by centrifugation and washed by fresh water for 3 times. The solid was re-suspended in 1 mL water and 1 mL SOD stock solution was added. The mixture was kept vortexing for 20 minutes and the solid was collected by centrifugation. SC@FNPCN-333 was washed with fresh water for 3 times before re-suspended in 0.3 mL water.

4.2.6 WST assay for determining SOD activity

WST assay kit is purchased from Sigma Aldrich. 20 μL sample solution containing different concentrations of SC@FNPCN-333 is mixed with 200 μL working solution.

Then 20 μL WST solution (1mL WST stock solution diluted by 19 mL working solution) is added and well mixed. Finally, 20 μL xanthine oxidase (XOD) solution (15 μL XOD stock solution diluted with 2.5 mL working solution) is added and the solution is incubated at 37°C for 30 minutes. The reading at 450 nm is collected by UV-vis spectroscopy.

4.2.7 Amplex Red-HRP assay for determining CAT activity

20 μL sample solution containing different concentrations of SC@FNPCN-333 is mixed with 200 μL hydrogen peroxide PBS solution (final concentration is 40 μM) and incubates at 37°C for 30 minutes. Then 20 μL HRP solution (0.4 U/mL) and 20 μL Amplex Red solution (100 μM) is added and incubates at 37°C for another 30 minutes. Fluorescence is collected with excitation wavelength of 540 nm and emission wavelength of 590 nm.

4.2.8 Cell internalization of SC@FNPCN-333 and CLSM imaging

HeLa cells were seeded in an 8 well plate and allowed to adhere overnight. Then the culture media was replaced by 200 μL fresh nrL-15 media containing SC@FNPCN-333 with different concentrations at 37°C for 15-480 minutes in darkness. The cells used for CLSM imaging was cultured in 75 μg/mL SC@FNPCN-333 for 2 h. Representatively, for the CLSM imaging, media containing SC@FNPCN-333 was removed and cells were washed with fresh nrL-15 for 3 times before they were stained with Hoechst 33342 (5 μg/mL), Lyso Tracker red (10 μg/mL) and SYTOX Blue (5 μg/mL). The cells were then incubated for 5 minutes before they were imaged. Co-incubation of SC@FNPCN-333 and D-dfTAT (20 μM) was conducted in the same manner. The only difference lied in the cell staining step. The cells were only stained with SYTOX Blue.

4.2.9 Cell lysis protocol

Cells are cultured in a 48 well plate and treated before the culture medium is removed. Cells are washed with fresh PBS for three times and five representative images are obtained by a confocal microscopy to count the cell number in the plate. Then the cells are digested by 200 μL concentrated nitric acid overnight. Each sample is measured three times by ICP-MS.

4.2.10 Intracellular Al content measurement at day 7

Cells (80-90% confluency) is cultured with 75 μg/mL SC@FNPCN-333 in nrL-15 for 2 h. Then the cells are washed with frest nrL-15 for three times and cultured with fresh DMEM. Cells are trypsinized and re-plated at day 1, 3, and 5. At day 7 the culture medium is removed and the cells are treatment with concentrated nitric acid overnight. The sample is measured three times by ICP-MS. Original Al content value: 104.1 ± 2.8 ng Al/10^5 cells, mean ± s.d.

4.2.11 *In cellulo* antioxidative activity evaluation of SC@FNPCN-333

HeLa cells were seeded in a 48 well plate and allowed to adhere overnight. For the positive control groups, cell culture media was replaced by 200 μL fresh DMEM media containing PQ with concentrations from 0.5 mM to 10 mM. The cells were cultured at 37ºC for 24 h, then the cells were washed with fresh PBS buffer for 3 times before charged with fresh nrL-15 buffer. The cells were stained with Hoechst 33342 (5 μg/mL) and SYTOX Green (5 μg/mL). To evaluate the antioxidative activity of SC@FNPCN-333, cells were treated with 75 μg/mL SC@FNPCN-333 for 2 h before charged with PQ solutions for 24 h. The washing and staining operations were the same as positive controls. Hoechst 33342 was excited for 500 ms and SYTOX Green was excited for 300

ms. 5 images were taken in each well. Each treatment condition was replicated for 3 wells.

4.2.12 Real-time ROS monitoring in living cells

Cells are cultured in a 48 well plate and are treated with SC@FNPCN-333 for 2 h in nrL-15. Then the medium is removed and the cells are washed with fresh nrL-15 for three times. Then the cells are incubated with nrL-15 containing 500 μM pyocianin and 5 μM superoxide detection dye for 30 minutes before imaged by a confocal microscope.

4.2.13 Theoretical estimation of enzyme loading in NPCN-333

In each unit cell of PCN-333, there are eight of A-cages (5.5 nm) and 16 of B-cages (4.2 nm). The volume of each unit cell = $(126\ Å)^3 = 2.0 \times 10^{-18}\ cm^3$. The density of PCN-333(Al) = $0.23\ g/cm^3$. So the mass of each unit cell = $\rho \times V = 0.46 \times 10^{-18}$ g. Therefore, the total number of unit cells per gram of PCN-333(Al) is: $1/(0.46 \times 10^{-18}) = 2.2 \times 10^{18}$. And the A-cage in each gram of PCN-333(Al) = $2.2 \times 10^{18} \times 8 = 1.7 \times 10^{19} = 2.9 \times 10^{-5}$ mol. B-cage in each gram of PCN-333(Al) = $3.4 \times 10^{19} = 5.8 \times 10^{-5}$ mol. For SOD, M_W = 16.3 kDa, so the maximum loading is $16300 \times 5.8 \times 10^{-5} = 0.92$ g/g. For CAT, M_W = 64 kDa, so the maximum loading is $60000 \times 2.9 \times 10^{-5} = 1.74$ g/g.

4.2.14 Theoretical estimation of enzyme loading in FNPCN-333

In each unit cell of PCN-333, there are eight of A-cages (5.5 nm) and 16 of B-cages (4.2 nm). The volume of each unit cell = $(126\ Å)^3 = 2.0 \times 10^{-18}\ cm^3$. The density of FNPCN-333(Al) = $0.26\ g/cm^3$. So the mass of each unit cell = $\rho \times V = 0.52 \times 10^{-18}$ g. Therefore, the total number of unit cells per gram of PCN-333(Al) is: $1/(0.52 \times 10^{-18}) = 1.95 \times 10^{18}$. And the A-cage in each gram of PCN-333(Al) = $1.95 \times 10^{18} \times 8 = 1.5 \times 10^{19} = 2.6 \times 10^{-5}$ mol. B-cage in each gram of PCN-333(Al) = $3.0 \times 10^{19} = 5.2 \times 10^{-5}$ mol. For

SOD, M_W = 16.3 kDa, so the maximum loading is $16300 \times 5.2 \times 10^{-5} = 0.82$ g/g. For CAT, M_W = 64 kDa, so the maximum loading is $60000 \times 2.6 \times 10^{-5} = 1.56$ g/g.

4.2.15 Colocalization coefficient estimation

For cellular colocalization experiments, the Manders' overlap coefficient R (measures how interdependent the red and green channels are) and colocalization coefficient M1 (measures the percentage of above-background pixels in the red channel that overlap with the above-background pixels in the green channel) were calculated using ImageJ (NIH).

4.3 Results

4.3.1 Preparation and characterization of PCN-333 nanoparticles

The basic secondary building unit of PCN-333 is a supertetrahedron, which consists of an aluminum trimeric cluster at the four vertices and TATB ligands on the faces, in a vertex sharing manner (Figure IV-1). The supertetrahedron is the secondary building block for two mesoporous cavities: a smaller dodecahedral cage composed of 20 supertetrahedra connected by vertex sharing with exclusive pentagonal windows and a larger hexacaidecahedral (hexagonal-truncated trapezohedral) cage surrounded by 28 supertetrahedra with both pentagonal and hexagonal windows. The cavity size of supertetrahedral, dodecahedral and hexacaidecahedral cage is 1.1, 4.2 and 5.5 nm. Nanoscale PCN-333 (NPCN-333) was synthesized in the condition similar to that of microscale PCN-333, with differences lying in the concentration of starting material and the amount of modulating reagents. Transmission electron microscopy (TEM) images indicated that NPCN-333 particles possessed spherical shape with an average diameter of

100 nm (Figure IV-1). This diameter was coincident with that measured by dynamic light scattering (DLS). The as-synthesized particles demonstrated high crystallinity as determined by powder X-ray diffraction (PXRD). The pattern was isostructural to PCN-333, although the peaks were broadened due to the reduced particle size. N_2 isotherm at 77K revealed that the NPCN-333 was highly porous with hierarchical porosity. The surface area was 2793 m^2 g^{-1} and the void volume was 2.94 cm^3 g^{-1}. FNPCN-333, a

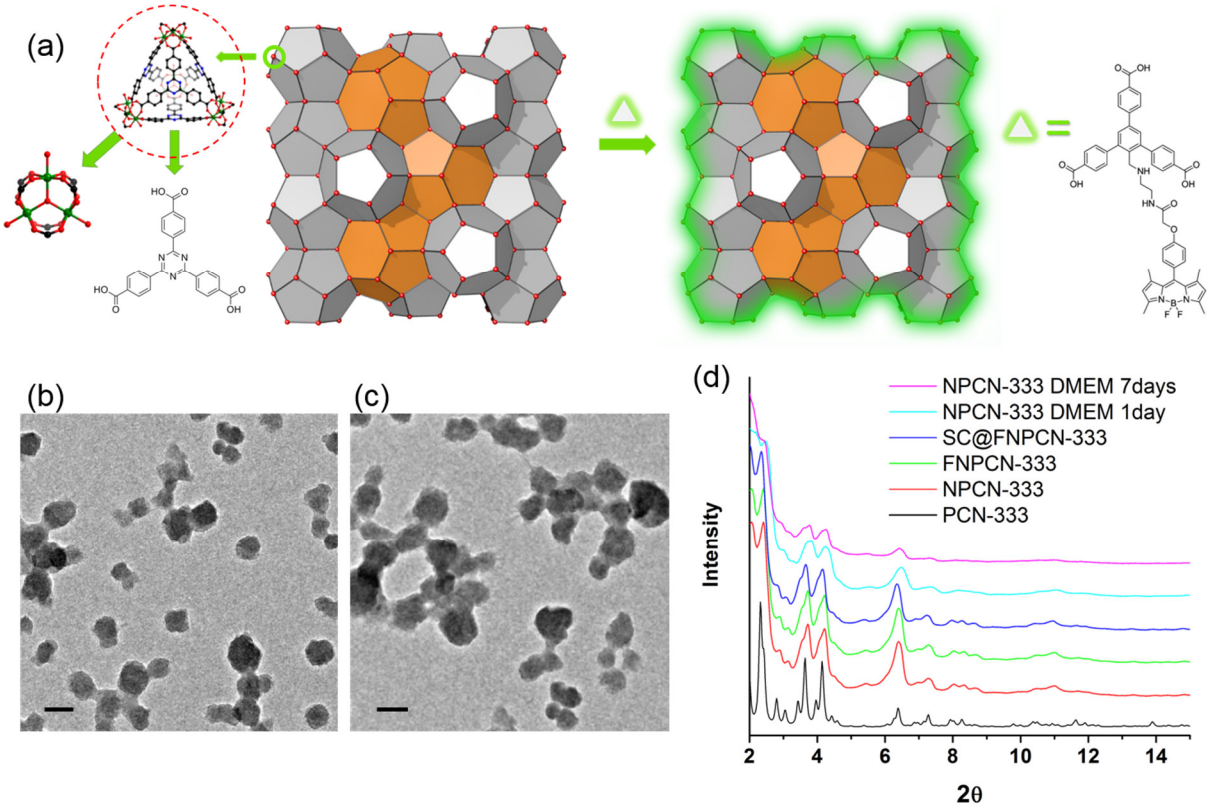

Figure IV-1. Structure and characterization of PCN-333 nanoparticles. (a) PCN-333 is composed of trimeric clusters and TATB ligands, which self-assemble into supertetrahedra (highlighted in red dashed circle). The supertetrahedra are connected with each other in a vertex-sharing manner. A green fluorophore is anchored on NPCN-333 via ligand metathesis. (b) TEM image of NPCN-333. Scale bar: 100 nm. (c) TEM image of FNPCN-333. Scale bar: 100 nm. (d) Powder X-ray diffraction patterns (2θ from 2 to 15 degree) of microscale PCN-333 (black); NPCN-333 (red); FNPCN-333 (green); SC@FNPCN-333 (blue); NPCN-333 soaked in DMEM for 1 day (cyan); NPCN-333 soaked in DMEM for 7 days (magenta).

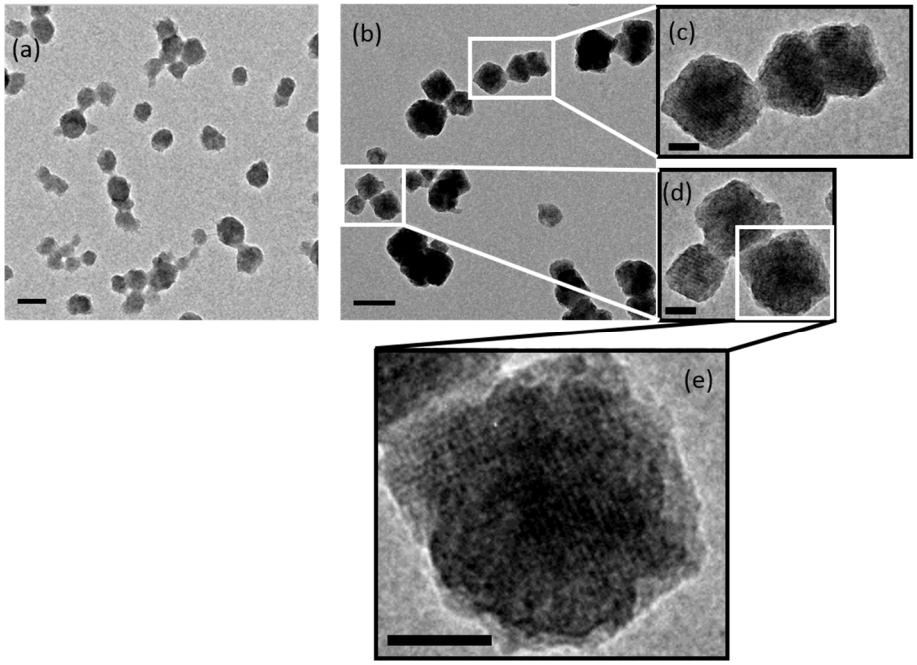

Figure IV-2. TEM images of SC@FNPCN-333 (a) and NPCN-333 after soaking in DMEM for 7 days (b). The zoomed in images show the fringes on the crystals. Scale bar: 100 nm (a), 200 nm (b), 50 nm (c-e).

fluorescent version of NPCN-333 prepared for live cell fluorescence microscopy experiments, was prepared via ligand metathesis of NPCN-333 with a BTB ligand functionalized with the fluorophore BODIPY. FNPCN-333 displays particle size, distribution, and porosity properties similar to those of NPCN-333 (surface area 2428 m^2 g^{-1}, void volume 2.30 cm^3 g^{-1}) (Figure IV-2). The presence of BTB-Green on the framework backbone is also confirmed by the relatively larger distribution of microporosity in FNPCN-333 than that of NPCN-333. However, unlike NPCN-333, FNPCN-333 is fluorescent with a maximal emission at 509 nm in water. As previously reported, PCN-333 is stable in aqueous solutions over a pH range of 3 to 9. When particle size decreased, the chemical stability was not compromised. The well-maintained

crystallinity of FNPCN-333 was confirmed by the unchanged PXRD pattern as well as the fringes on the crystals after soaking in the cell culture media for up to 7 days.

4.3.2 Enzyme encapsulation and protection by FNPCN-333

An early examination of the molecular dimensions of SOD (2.8*3.5*4.2 nm^3, 16.3 kDa)[247] and CAT (4.9*4.4*5.6 nm^3, 60 kDa)[248] indicated that these proteins could potentially fit in the 4.0 and 5.5 nm cavities of FNPCN-333, respectively. To test this idea, the two enzymes were incorporated into FNPCN-333 in a stepwise manner.[141] First,

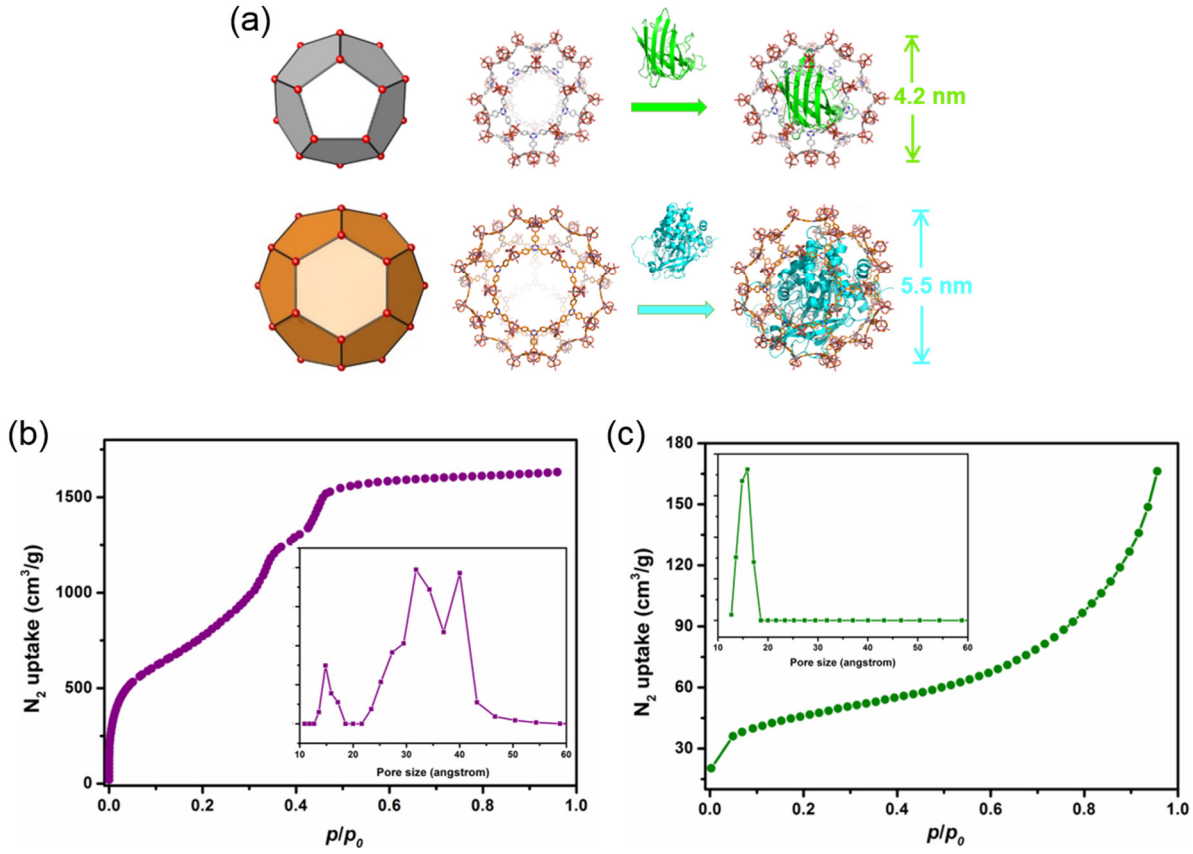

Figure IV-3. Enzyme encapsulation on FNPCN-333. (a) Schematic representation illustrating the relative size of the cavities present in FNPCN-333 and of the enzymes SOD and CAT (from PDB 1CBJ and 5GKN). The medium (grey) and large (orange) cavities of FNPCN-333 accommodate SOD (green) and CAT (cyan), respectively. (b)(c) N_2 isotherms of FNPCN-333 (b) and SC@FNPCN-333 (c) at 77K. Inlets show pore size distribution diagram derived from N_2 isotherm.

FNPCN-333 was incubated with CAT so as to occupy the larger MOF cavities. After addition of CAT, FNPCN-333 was incubated with SOD to load the smaller cavities that would not accommodate CAT. Based on BCA analysis, the encapsulation capacity of FNPCN-333 for SOD and CAT was 0.80 and 1.26 g g^{-1}, respectively. This is comparable to the calculated values of maximal encapsulation capacity (0.92 and 1.74 g g^{-1}) and is indicative of a high loading efficiency. Consistent with this notion, N_2 isotherm analysis shows that enzyme encapsulation leads to complete disappearance of the two mesoporous cavities. In contrast, the microporous cavities that are too small in volume to accommodate the protein molecules remain detectable. The crystallinity of the resulting bi-enzymatic nanofactory, named SC@FNPCN-333, was well maintained, as indicated by PXRD patterns. Thermal gravimetric analysis (TGA) further confirms high enzyme loading of FNPCN-333.

In order to determine whether encapsulated SOD and CAT are biologically functional, the water-soluble tetrazolium (WST) and horseradish peroxidase (HRP)-Amplex Red assays were performed. In the WST assay, the activity of SOD is detected by spectroscopically measuring the superoxide-mediated reduction of WST (pale yellow) to the formazan dye (dark yellow). In the HRP-Amplex Red assay, the fluorescent dye resorufin is produced upon oxidation of Amplex Red with hydrogen peroxide, a reaction catalyzed by HRP. By catalyzing the decomposition of hydrogen hydroxide, CAT inhibits the generation of resorufin. As shown in Fig. 2b, the superoxide detoxifying activity of SC@FNPCN-333 was comparable to that of free SOD. Similarly, the peroxide scavenging activity of SC@FNPCN-333 was comparable to that of free CAT (Figure IV-

4). Notably, SC@FNPCN-333 displayed persistent CAT and SOD enzymatic activities after soaking in the cell culture media (DMEM) for 7 days.

Resistance of the enzymatic nanofactory towards cellular degradation, from factors such as proteases and acidic pH, is crucial for its long-term performance in living cells.

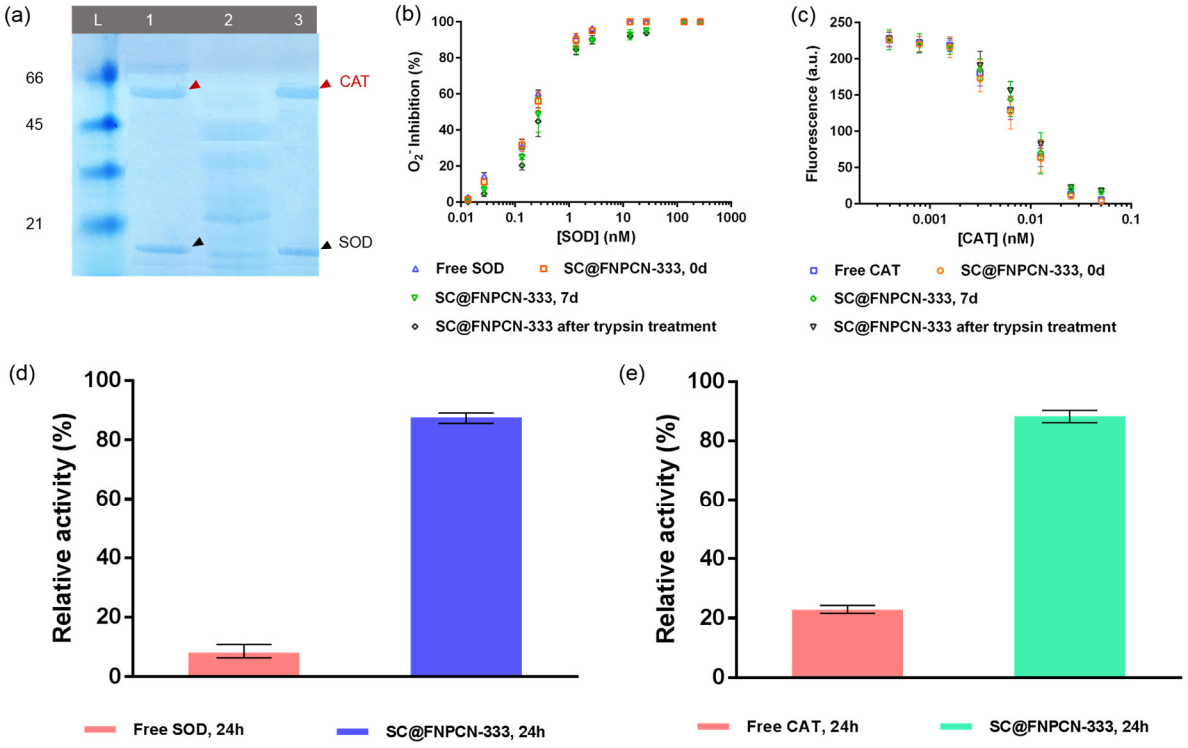

Figure IV-4. *In vitro* determination of enzymatic activities and resistance to perturbations. (a) SDS-PAGE analysis of SC@FNPCN-33 after exposure to the protease trypsin. L: protein ladder. Lane 1: free SOD (highlighted with black arrow) and CAT (highlighted with red arrow). Lane 2: Free SOD and CAT after treatment with trypsin for 1 h. Lane 3: SC@FNPCN-333 treated with trypsin for 1 h (analyzed after dissolution of MOF in HCl). (b) Relative enzymatic activities of several SOD formulations, as determined by the superoxide inhibition assay: free SOD (blue), freshly prepared SC@FNPCN-333 (orange), SC@FNPCN-333 stored for 7 days (green), SC@FNPCN-333 treated with trypsin for 2 h (black). n = 3, mean ± s.d. (c) Relative enzymatic activities of several CAT formulations, as measured by the inhibition of H_2O_2-mediated production of the fluorophore resorufin: free CAT (blue), freshly prepared SC@FNPCN-333 (orange), SC@FNPCN-333 stored for 7 days (green), SC@FNPCN-333 treated with trypsin for 2 h (black). n = 3, mean ± s.d. (d)(e) Relative SOD (d) and CAT (e) activities of free enzyme and SC@FNPCN-333 after soaking in pH 5.0 buffer for 24 h. n = 3, mean ± s.d.

To test whether NPCN-333 could provide a protective environment for SOD and CAT, SC@FNPCN-333 was first exposed *in vitro* for 2 h to the protease trypsin. SC@FNPCN-333 was subsequently treated with HCl so as to dissolve the MOF and release encapsulated proteins, including potential trypsin-digested enzyme fragments. The resulting supernatants were analyzed by SDS-PAGE. Trypsin readily digests SOD and CAT in their free form, as illustrated by the presence of small molecular weight bands (Figure IV-4). In contrast, bands corresponding to intact SOD and CAT are predominantly present for SC@FNPCN-333. In addition, SC@FNPCN-333 maintained its enzymatic activities after trypsin treatment, as indicated by the WST and HRP-Amplex Red assays. In order to test whether the nanofactories resist exposure to an acidic milieu, SOD, CAT and SC@FNPCN-333 were incubated at pH 5 (this pH mimics the luminal pH of late endosomes and lysosomes, organelles inside which MOF can accumulate, as shown below). Enzymatic activities were measured at 0.5 and 24 h and compared to those obtained at pH 7.4. After 0.5 h incubation, the acidic pH led to a moderate loss in activity for the free enzymes and for SC@FNPCN-333 (approximately 15 to 25% for SC@FNPCN-33 and CAT, 35% for SOD). After 24 h incubation, the activities of SOD and CAT at pH 5 were reduced to only 10 or 20% of those obtained at pH 7.4, presumably because of slow unfolding of the proteins. In contrast, the activities of SC@FNPCN-333 at pH 5 were unchanged during the course of the experiment (>80% relative activity at 1 and 24 h). Together, these experiments indicate that FNPCN-333 provides a platform for high enzymatic activity, protection from proteases, and resistance under a broad pH range. These encouraging data also set the stage for *in cellulo* testing.

4.3.4 Cellular uptake of SC@FNPCN-333

In order to exert optimal enzymatic activities, exogenously administered enzyme nanofactories should ideally reach the intracellular locations occupied by their endogenous counterparts. SOD is localized in the cytosolic space and mitochondria of

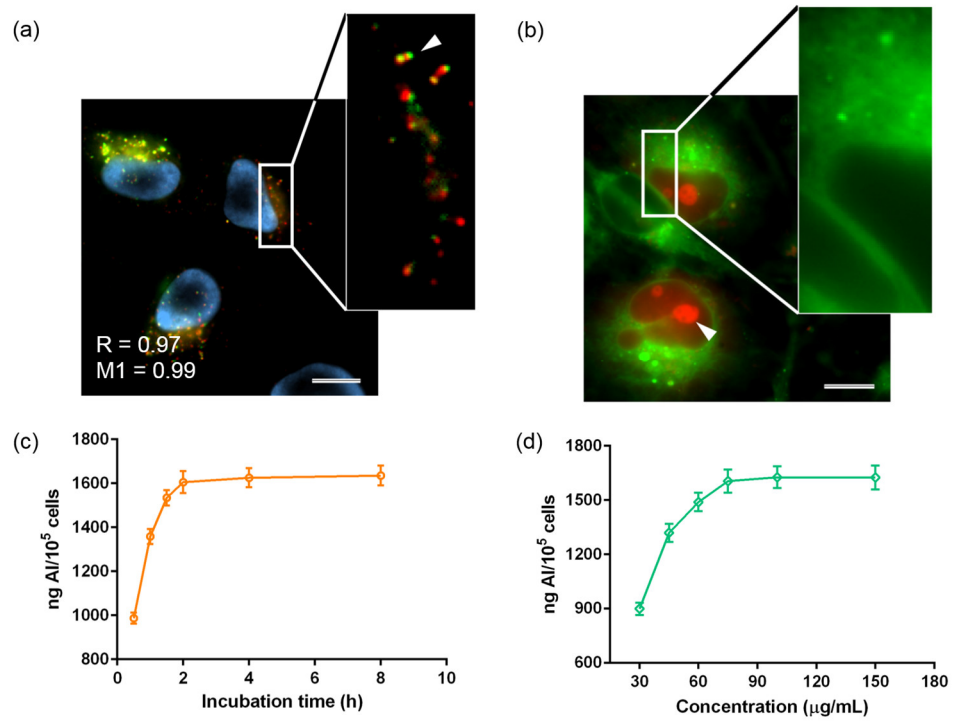

Figure IV-5. Cellular internalization of SC@FNPCN-333 by HeLa cells. (a) 100X microscopy images of SC@FNPCN-333 (75 μg mL^{-1}) incubated with HeLa cells for 2 h, then stained with the nuclear marker Hoechst 33342 and LysoTracker red. Cell nuclei, SC@FNPCN-333 and LysoTracker red labeled acidic organelles (i.e. late endosomes and lysosomes) are pseudo-colored in cyan, green and red, respectively. The arrow in the enlarged green/red overlay image illustrates the colocalization of puncta containing both SC@FNPCN-333 and LysoTracker red. Pearson's correlation coefficient R and Mander's correlation coefficient M1 is indicated. Scale bar: 10 μm. (b) 100X microscopy images of SC@FNPCN-333 co-incubated with the cytosolic delivery agent dfTAT for 2 h. The image is an overlay of SC@FNPCN-333 (pseudocolored green) and dfTAT (pseudocolored red). The arrow points to a dfTAT-stained nucleolus, indicative of effective cytosolic penetration of the delivery reagent. The enlarged image illustrates the green fluorescence of SC@FNPCN-333 in the cytosolic space and, by contrast, a dark area suggestive of the exclusion of SC@FNPCN-333 from the cell nucleus. Scale bar: 10 μm. (c) ICP-MS analysis of Al content in HeLa cells incubated with SC@FNPCN-333 (75 μg mL^{-1}) for varying time points. n = 3, mean ± s.d. (d) ICP-MS analysis of Al content in HeLa cells incubated with varying concentrations of SC@FNPCN-333 for 2 h. n = 3, mean ± s.d.

human cells while CAT is typically localized in peroxisomes.[249, 250] On one hand, given the size and biophysical properties of MOF, we did not anticipate that SC@FNPCN-333 would spontaneously penetrate into the cytosolic space of cells and reach these intracellular destinations. On the other hand, 100 nm particles are small enough to allow for cellular uptake by endocytosis. We therefore envisioned that endosomal entrapment of SC@FNPCN-333 should be possible. Furthermore, we have recently developed dfTAT, a delivery reagent that causes leakage of late endosomes and permits the release of endocytosed cargos into the cytosolic space of cells.[243, 251, 252] To test whether SC@FNPCN-333 endosomal or cytosolic localization could be achieved, SC@FNPCN-333 was incubated with HeLa cells for 2 h, with or without dfTAT. When administered alone to live cells, SC@FNPCN-333 displayed an intracellular punctate fluorescence distribution, as observed by microscopy. Colocalization of SC@FNPCN-333 with LysoTracker red, a late endosome and lysosome marker,[253] confirmed entrapment of the enzyme nanofactories within these endocytic organelles (L.E./LYS, Figure IV-5). Consistent with these results, incubation of SC@FNPCN-333 with HeLa cells at 4 ^{o}C, a condition that inhibits energy-dependent endocytic uptake, or in the presence of amiloride, an inhibitor of macropinocytosis, led to a dramatic reduction in the number of intracellular SC@FNPCN-333-positive puncta and to a reduction of co-localization with LysoTracker red. When administered in the presence of dfTAT, SC@FNPCN-333 presented a homogeneously diffuse fluorescence distribution, indicative of localization in the cytosolic area, albeit was accompanied by a residual punctate distribution indicative of incomplete endosomal escape. Moreover, consistent with the notion that the size of SC@FNPCN-333 exceeds the nuclear pore complex size threshold for passive diffusion,

the cytosolic green fluorescence distribution of SC@FNPCN-333 was excluded from

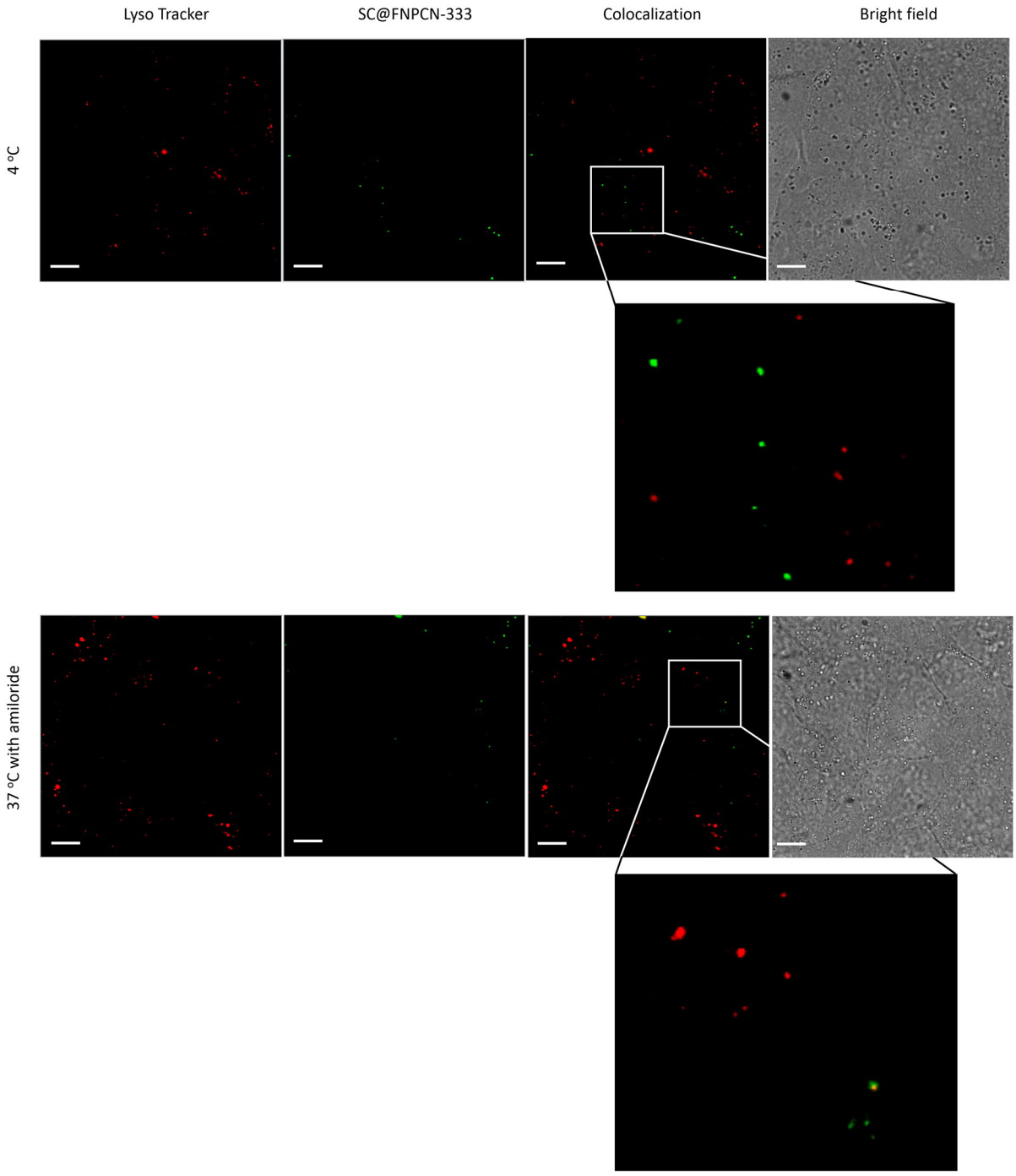

Figure IV-6. Effect of low temperature (4 °C) and endocytosis inhibitor (amiloride) on the cellular internalization of SC@FNPCN-333 by HeLa cells. Zoom-in images are provided. 4 °C colocalization coefficient: 0.34 (Pearson's), 0.30 (Mander's). 37°C with amiloride colocalization coefficient: 0.61 (Pearson's), 0.58 (Mander's). Scale bar: 10 µm.

nuclei (Figure IV-5). By extension, this staining supports the notion that the diffuse fluorescence observed from SC@FNPCN-333 is indeed cytosolic (in other words, artifactual out-of-focus extracellular signals would not be selectively excluded from nuclei). Overall, these results indicate that the intracellular accumulation of enzymes nanofactories can be achieved and that their intracellular distribution can be modulated. Notably, the cytotoxicity of SC@FNPCN-333, evaluated using a SYTOX Blue exclusion assay, was negligible, in the presence and absence of dfTAT. In particular, cell viability was more than 97% at 0 or 24 h post-incubation, a result identical to that obtained with untreated cells.

In order to optimize MOF cellular uptake and given that the two cellular delivery approaches used above are dependent on endocytosis, we next tested the dependence of MOF endocytic uptake on time and concentration. To quantify the endocytic uptake of SC@FNPCN-333, the aluminum (Al) content of cells incubated with SC@FNPCN-333 was measured by ICP-MS. For instance, cells were incubated with 75 μg mL^{-1} SC@FNPCN-333, harvested at different time points, and lysates were prepared for analysis. As shown in Figure IV-5, Al levels dramatically increased after 30 minutes incubation and, after 2 h incubation, reached a plateau corresponding to 89.2 ± 3.7 nmol nanoparticle per 10^5 cells. Alternatively, cells were incubated with varying amounts of SC@FNPCN-333 and analyzed after 2 h incubation. In this case, internalization initially increased with SC@FNPCN-333 concentration but reached a plateau at 75 μg mL^{-1}. Together, these results indicate that incubation of cells with 75 μg mL^{-1} SC@FNPCN-333 for 2 h leads to maximal cellular uptake. We therefore chose these conditions for subsequent studies.

4.3.5 *In cellulo* activity of SC@FNPCN-333

To address whether SC@FNPCN-333 can protect cells from ROS-induced toxicity, we established an assay in which cells are exposed to oxidative stress. In particular, we treated cells with paraquat (PQ), a redox-active herbicide previously linked to various human diseases, including organ failure and Parkinson's disease.[254] As expected, cells treated with varying concentrations of PQ (0.5-10 mM) for 24 hours showed reduced cell viability when compared to untreated cells (Figure IV-7). Pretreating cells with FNPCN-333 (75 μg mL^{-1}, 2h) did neither increase nor decrease cell viability, indicating that MOF alone do not interfere with the toxicity of PQ. In contrast, when cells were pre-treated with SC@FNPCN-333 (75 μg mL^{-1}, 2h; this condition leads to L.E./LYS

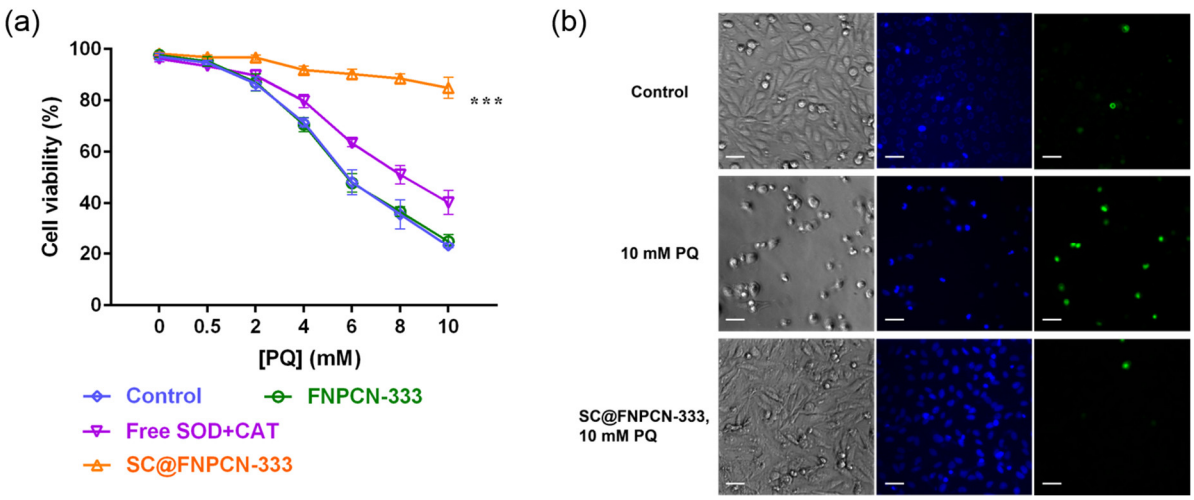

Figure IV-7. Protection of HeLa cells from oxidative stress by SC@FNPCN-333. (a) Viability of cells treated with the oxidant paraquat (PQ) for 24 h. Blue: control. Green: cells pre-treated with FNPCN-333. Orange: cells pre-treated with SC@FNPCN-333 (75 μg mL^{-1}) for 2 h. Magenta: cells pre-treated with SOD (60 μg mL^{-1}) and CAT (94.5 μg mL^{-1}) for 2 h. n = 5, mean ± s.d. *** represents $P \leq 0.001$. (b) CLSM images of HeLa cells as control, treated with 10 mM PQ for 24 h, pre-treated with SC@FNPCN-333 then treated with 10 mM PQ for 24 h. Left panel: bright field images; middle panel: cell nucleus stained with Hoechst 33342; right panel: dead cell nucleus stained with SYTOX Green. Scale bar: 100 μm.

accumulation), cell viability was restored to a high degree, with more than 85% of cells surviving the most cytotoxic PQ treatment. In comparison, pretreating cells with either free enzymes, or with MOF loaded with only SOD or CAT (S@FNPCN-333 or C@FNPCN-333) led to only a minor improvement in cell viability. Moreover, a mixture of S@FNPCN-333 and C@FNPCN-333 did not perform as well as SC@FNPCN-333,

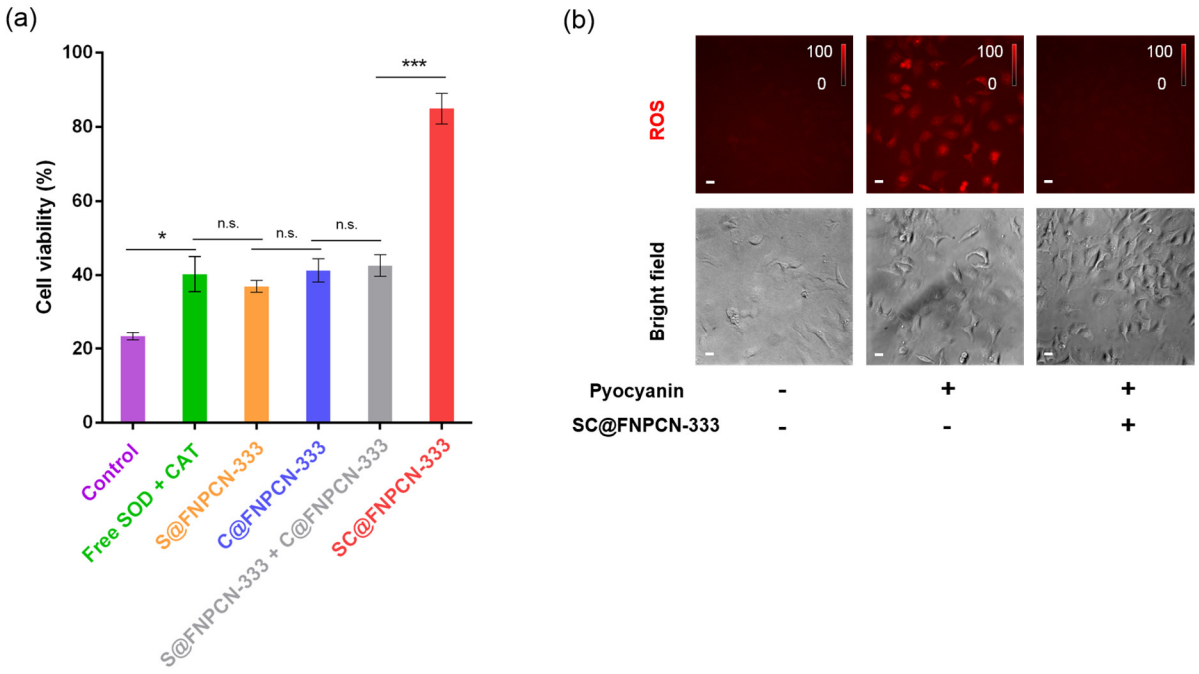

Figure IV-8. Protection of HeLa cells from oxidative stress by SC@FNPCN-333. (a) Viability of cells treated with PQ (10 mM) for 24 h following pre-treatments with various enzyme formulations. Purple: control of cells with no pretreatment. Green: cells pre-treated with SOD (60 μg mL^{-1}) and CAT (94.5 μg mL^{-1}) for 2 h. Orange: cells pre-treated with S@FNPCN-333 (75 μg mL^{-1}) for 2 h. Blue: cells pre-treated with C@FNPCN-333 (75 μg mL^{-1}) for 2 h. Light grey: cells pre-treated with S@FNPCN-333 (75 μg mL^{-1}) and C@FNPCN-333 (75 μg mL^{-1}) for 2 h. Red: cells pre-treated with SC@FNPCN-333 (75 μg mL^{-1}) for 2 h. n = 5, mean ± s.d. * and *** represent $P<0.05$ and $P\leq0.001$, respectively. (b) *In cellulo* ROS detoxification by SC@FNPCN-333. Presence of superoxide, which generates an oxidized and red fluorescent form of SDR, was detected by fluorescence microscopy. Fluorescence microscopy images (20X magnification) of SDR are pseudocolored red. Images were acquired and processed using identical conditions. Intensity bars show the relative fluorescence intensities of the 3 images (normalized to a highest signal of 100). The experiment was replicated for three times and representative images are displayed. Scale bar: 10 μm.

pointing to a beneficial effect of enzyme proximity obtained from co-encapsulation. In order to validate that SC@FNPCN-333 exerts a protective effect by mediating ROS detoxification, the impact of the enzymes nanofactory on ROS levels was assessed by microscopy. Cells were incubated with pyocyanin, a bacterial toxin that produces superoxide, and a fluorescent Superoxide Detection Reagent (SDR). Microscopy imaging shows that, the fluorescence of SDR, which is proportional to the superoxide concentration in cells, increased in the presence of pyocyanin. However, upon pretreatment with SC@FNPCN-333, the SDR signal was restored to basal level (Figure IV-8). When the cellular uptake of SC@FNPCN-333 was inhibited by either low temperature incubation (4 ^{o}C) or amiloride, viability against PQ was barely improved compared to cells not pre-treated withSC@FNPCN-333. Together, these results confirm that SC@FNPCN-333 protects cells from ROS-induced toxicity by eliminating ROS species. Finally, similar PQ-protection results were obtained in the presence of dfTAT, indicating that differences in intracellular localization (cytosolic versus endocytic) does not significantly impact the ROS detoxifying capacity of the enzyme nanofactories. Given that L.E./LYS are extremely degradative and potentially more damaging than the cytosolic space, we next tested the long-term performance of the enzymes nanofactories in this environment for maximal stringency.

To maximize their application and usefulness, enzyme nanofactories should have a persistent effect inside cells. To test whether SC@FNPCN-333 could sustain its protecting effect beyond 24 h, cells pre-incubated with SC@FNPCN-333 were cultured with fresh DMEM buffer for up to a week. PQ-induced toxicity was evaluated at day 2 and day 7. As shown in Figure IV-9, treating cells with free SOD and CAT, which

provided only a weak protective effect at day 0, failed to rescue cells from PQ-induced cytotoxicity at day 1. In contrast, the rescuing effect of SC@NPCN-333 at day 2 was similar to that obtained at day 1. Moreover, this effect, although partially diminished, remained significant at day 7. This long-term persistence is consistent with the stability of the MOF material detected *in vitro*, where little protein leaching out of the MOF is observed over 7 days in an acidic milieu. Notably, ICP-MS analysis shows that the intracellular aluminium content present at day 7 was approximately 6% of that of cells at day 0 (1600 ng Al per 10^5 cells are detected after incubation of 75 g mL^{-1} of SC@FNPCN-333 at day 0, 104 ng Al per 10^5 cells at day 7). This is therefore indicative of a decline in overall MOF concentration of present in cells overtime, as would be expected from the dilution that take place during each cell division during one week of

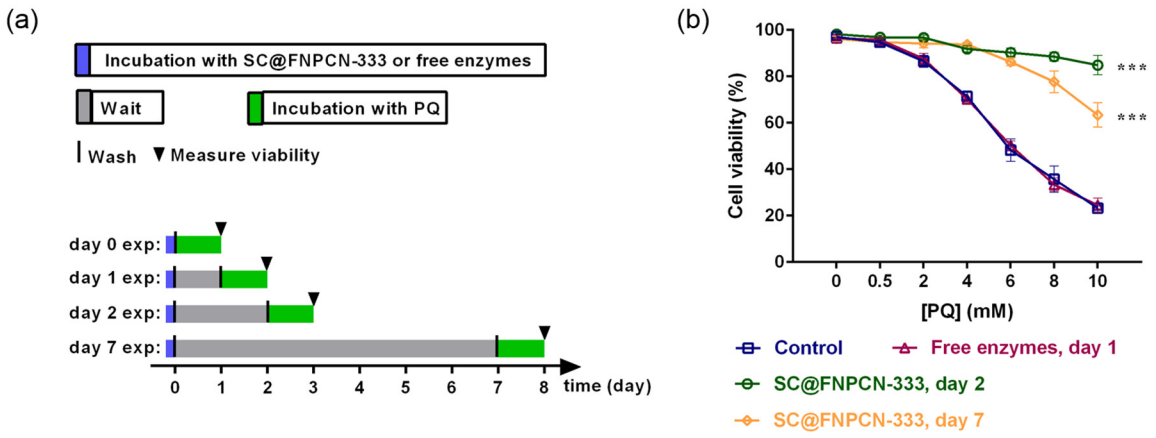

Figure IV-9. Long-term protection of HeLa cells from oxidative stress by SC@FNPCN-333. (a) Timeline of the experiment. Cells were pretreated with SC@FNPCN-333 (75 µg mL^{-1}, 2 h), washed and cultured for several days (grey time period in scheme). Cells were then treated with PQ (24h incubation) and cell viability was quantified. (b) Outcome of the experiment. Dark blue: control of cells not pretreated with SC@FNPCN-333. Dark magenta: cells pre-treated with SOD (60 µg mL^{-1}) and CAT (94.5 µg mL^{-1}), PQ-protection assessed 24 h post-treatment. Green: cells pre-treated with SC@FNPCN-333 (75 µg mL^{-1}), PQ-protection assessed 48 h post-treatment. Orange: cells pre-treated with SC@FNPCN-333 (75 µg mL^{-1}), PQ-protection assessed 168 h post-treatment. n = 5, mean ± s.d. *** represents $P \leq 0.001$.

cell culture. However, titration experiments confirmed that lower doses of SC@FNPCN-333 could maintain high protection activities in cells. In particular, while incubation of cells at 1 g mL^{-1} SC@FNPCN-333 provides no protective effect, incubation with 2.5 g mL^{-1} SC@FNPCN-333 leads to approximately 100 ng Al per 10^5 cells and 70% cell viability after PQ treatment (a condition similar to that obtained at day 7 after incubation of 75 g mL^{-1} SC@FNPCN-333). Overall, these results indicate that the prolonged effect of SC@FNPCN-333 is imparted by the chemical stability of the material as well as its sustained enzymatic activity even at low intracellular concentrations.

4.4 Summary and Discussion

This report establishes that enzymatic nanofactories based on MOF can sustain intracellular enzymatic activities for an extended period of time. The proteins encapsulated within the MOF structure are enzymatically active, indicating that proper enzyme folding is achieved and maintained within the MOF and that soluble substrates and products can diffuse in and out of the MOF-enzyme nanofactories. The MOF act as a nanocage that protects encapsulated enzymes from proteases and the acidic environment inside L.E./LYS. The mechanism of protease-resistance presumably involves restricting the access of a protease to its protein substrate, in this case CAT and SOD. In particular, while trypsin may be small enough to enter an empty MOF cavity, it is unlikely that it would be able to do so if the cavity is already loaded with SOD or CAT. Alternatively, the MOF environment may stabilize the folding/structure of encapsulated enzymes. This would also contribute to improving protease resistance (unstructured proteins are more readily proteolized than folded proteins) and could explain how the MOF prevents pH-

induced unfolding and loss of activity. Overall, these features provide a material that persists in the lumen of L.E./LYS, a highly degradative cellular milieu that combines a high density of proteases and acidic pH. Based on our *in vitro* and *in cellulo* data, it is likely that free enzymes are rapidly degraded in these organelles. It is also likely that it is the slow leaching of enzymes from the MOF structure that contribute to the gradual loss of activity detected in live cells.

It is notable that the proximity of SOD and CAT in the enzymatic nanofactory enhances the protective effect against PQ induced oxidative stress. SOD catalyzes the disproportionation of superoxide and generates H_2O_2 and oxygen, while H_2O_2 is consumed by CAT, yielding water and oxygen. Since the two reactions catalyzed by SOD and CAT may occur in a cascade manner, it is likely that SOD-generated H_2O_2 is degraded by CAT before this ROS diffuses away from the nanofactory. Conversely, in the case of MOF nanoparticles carrying only one enzyme, the H_2O_2 generated by S@FNPCN-333 may be more likely to diffuse away from C@FNPCN-333 before detoxification can occur. The ROS that escapes the nanofactories may then reach the cytosolic area and cause oxidative damage, inducing increased toxicity, as observed.
In contrast to the proximity effect, altering the localization of SC@FNPCN-333 (endocytic vs. cytosolic) did not result in significant difference in protecting cells from PQ induced oxidative stress. On one hand, this is surprising as one may expect cytosolic SC@FNPCN-333 to come into contact with more diffusing ROS than SC@FNPCN-333 trapped inside endocytic organelles. On the other hand, it is interesting to note that endosomes redox active and that they contain proteins capable of mediating the transport of ROS across bilayers.[255-257] It is therefore possible that a significant portion of PQ-

generated superoxide reaches the lumen of endocytic organelles. Under such scenario, endocytic and cytosolic SC@FNPCN-333 would show similar activities by detoxifying cells from the damaging effects of superoxide, before or after in penetrates endosomes, respectively.

Given the multiple criteria that have to be taken into account to generate optimal nanofactories, it is difficult to predict which enzymes may be compatible with MOF encapsulation. Several aspects of a MOF-based strategy however point to a potentially broad applicability. For instance, the diameter of the MOF cavities is tunable, providing opportunities for the encapsulation of enzymes of various sizes. It is also possible to encapsulate a cocktail of enzymes, something that can lead to synergistic effects as demonstrated by the fact that SC@FNPCN-333 clearly outperforms the combination of S@FNPCN-333 and C@FNPCN-333. Additionally, the size and surface of the MOF can also be modified. This in turn could facilitate development of nanofactories that reside inside cells for even longer periods of time. Moreover, the compatibility of MOF nanofactories with dfTAT mediated cytosolic delivery highlights that these materials have access to the cytosolic space of live cells. While it did not lead to improvements in the context of SC@FNPCN-333, this is presumably important for the future development of nanofactories that would involve substrates that are confined within the cytosolic space, as is the case for numerous molecules associated with different metabolic pathways.

A side by side comparison between the nanofactories presented in this study and other reported enzyme protection techniques is difficult.[258-260] This is in part because the enzymes encapsulated often vary, persistence in cells is often not documented, and because each technique has a different set of advantages and disadvantages. Nonetheless,

we propose that *in vitro* performances of the nanofactories achieved in this proof-of-concept study are extremely encouraging. Moreover, MOFs provide specific benefits over other encapsulation materials. For instance, liposomes, the most common enzyme carrier system, protect enzymes from degradation effectively. However, the lipid bilayer of liposomes forms a barrier between enzyme and substrate. Enzyme protection therefore comes at the cost of a severe reduction in enzymatic activity, unless complex strategies are implemented to permit substrate diffusion or controlled enzyme release. In contrast, MOF-encapsulated enzymes remain accessible to substrate without the need of enzyme release from the carrier. As a matter of fact, the activity of encapsulated enzymes is comparable to that of the enzymes in their free form. MOF encapsulation, and protection from proteolytic degradation, therefore does not compromise enzymatic activity. This is turn allows for simple design and nanparticle synthesis (i.e. no need for release strategies).

While the biocompatibility of MOF, *in cellulo* and *in vivo*, certainly needs to be further tested, these results point to various potential biotechnological approaches. For instance, by varying the enzymes encapsulated within the MOF structures, nanofactories such as those described herein may replace defective metabolic activities and contribute to enzyme replacement therapies. Moreover, we envision that MOF-enzyme nanofactories may find applications in cell biology and *ex vivo* cell engineering. For instance, SC@FNPCN-333 may be readily useful for cultures of cells prone to oxidative stress (e.g. primary cells). MOF-enzyme nanofactories may also be useful as organelle mimetics that confer cells novel properties, including resistance to various stresses.[261-265] We also

envision that MOF-enzyme nanofactories, if combined with reporter assays, could allow the probing of metabolic activities in cell cultures over extended periods of time.

CHAPTER V

LONG-PERSISTENT ENZYME-MOF NANOREACTOR ACTIVATES NON-TOXIC PARACETAMOL FOR CANCER THERAPY[5]

5.1 Introduction

Chemotherapeutics typically interfere with mitosis and demonstrate maximum toxicity towards rapidly-dividing cells.[266] However, chemotherapy drugs are poorly selective and often result in severe adverse effects that include kidney damage, bone marrow suppression, nerve damage, hair loss, low blood count, and inflammation.[267-269] In addition, resistance to chemotherapy occurs in certain cancer cell lines, thereby declining the efficiency of treatment.[270-272] One strategy to approach these problems is to employ prodrugs, compounds that are innocuous until metabolized to give cytotoxic products in a tumor microenvironment.[273-276] However, this approach involves a new challenge, the identification of activation mechanisms specific to cancer cells. To date, enzymes overexpressed in tumor cells have been used to activate prodrug.[275, 277] Nevertheless, because these targeting enzymes may also present in normal cells, albeit at lower levels, many of these prodrug therapies retained poor selectivity and demonstrated minimal success. [278, 279] To circumvent this, an alternative strategy involves delivering exogenous "activating" enzymes into cancer cells. Tumor specific accumulation of the enzyme "activator" is achieved by conjugation to tumor directing antibodies or immunoliposomes.[280-283] While potentially useful, the biggest drawback is that externally-administered enzymes are highly vulnerable to degradation in the bloodstream.[284, 285]

---

[5]Reproduced with permission from "Long-Persistent Enzyme-MOF Nanoreactor Activates Non-toxic Paracetamol for Cancer Therapy" by Lian, X.; Huang, Y.; Zhu, Y.; Fang, Y.; Zhao, R.; Joseph, E.; Li, J.; Pellois, J.-P.; Zhou, H.-C. *Angew. Chem. Int. Ed.,* **2018**, *57*, 5725-5730, copyright 2018 by John & Wiley Sons.

Thus the feasibility of this strategy remains unclear and strategies that can improve the biocompatibility of externally-administered enzymes are needed.

Herein we demonstrate that enzymatic nanoreactors based on metal-organic frameworks (MOFs) can be potent prodrug activators. MOFs are an emerging platform that demonstrates potential for a number of biotechnological applications, including sensing, imaging, drug delivery and enzyme encapsulation.[129, 141, 220, 286-297] Encapsulated enzymes demonstrate well-preserved catalytic activities.[129] Encapsulated enzymes also show enhanced stability under protein denaturation conditions, such as organic solvents, extreme pH environments, or high temperatures.[138, 139, 298] Moreover, MOFs efficiently protect encapsulated enzymes from proteolytic degradation, presumably by preventing access of proteases to the protein substrate.[141, 299] Notably, the porous nature of MOFs allows for facile substrate diffusion and product release, a feature typically superior to

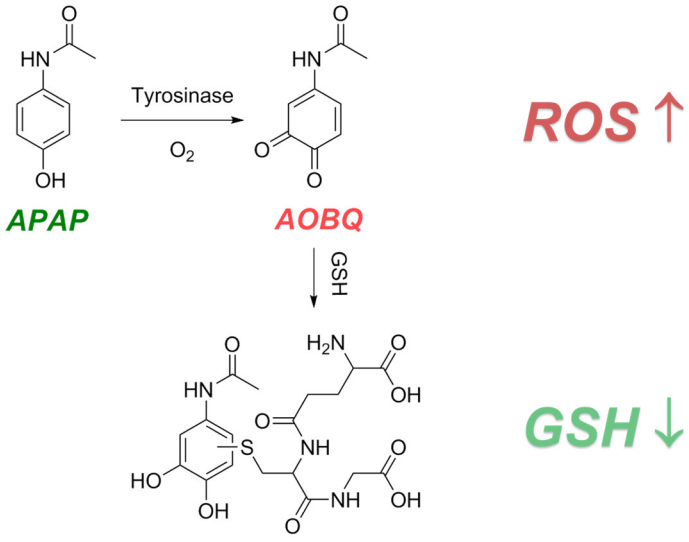

Scheme V-1. Nontoxic prodrug APAP oxidation is catalyzed by tyrosinase, yielding cytotoxic AOBQ, which induces ROS generation and GSH depletion.

other well-established carriers.[300] In this work, we selected PCN-333(Al) as the enzyme carrier owing to its high enzyme encapsulation capacity, facile modification with fluorophores, and chemical robustness in cellular environment.[289] To achieve tumor specific prodrug activation, tyrosinase (TYR), which is uniquely localized in melanocytes and melanoma cells, is chosen as the activating enzyme.[301] Paracetamol (APAP), the active ingredient of Tylenol, is used as the nontoxic prodrug.[302] Both *in cellulo* and *in vivo* experiments establish that APAP along with enzyme-MOF nanoreactor induced significant cytotoxicity in drug-resistant cancer cells and led to tumor regression. Mechanistically, cytotoxicity arises from 4-acetamido-*o*-benzoquinone (AOBQ), the enzymatic conversion product of APAP, and from subsequent reactive oxygen species (ROS) generation and glutathione (GSH) depletion.

5.2 Experimental Section

5.2.1 Material and Instrumentation

Aluminum chloride hexahydrate, *N*-bromosuccinimide (NBS), benzoyl peroxide (BPO), ethylenediamine, triethylamine, trifluoroborane etherate, *N*-hydroxysuccinimide, *N*-(3-Dimethylaminopropyl)-*N'*-ethylcarbodiimide (EDC), *N,N*-dimethylformamide (DMF), tetrahydrofuran (THF), potassium carbonate, hydrochloric acid and sodium hydroxide were purchased from VWR. Carbon tetrachloride, 3-(4,5-dimethylthiazol-2-yl)-2,5-diphenyltetrazolium bromide (MTT) and tyrosinase (TYR) were purchased from Sigma Aldrich. Dulbecco's minimum essential medium (DMEM), Roswell Park Memorial Institute (RPMI) 1640 Medium, 2-[4-(2-hydroxyethyl)piperazin-1-yl]ethanesulfonic acid (HEPES), Leibovitz's L-15 medium without cysteine (non-

reducing L-15, nrL-15), 10% fetal bovine serum (FBS) and 1× penicillin/streptomycin (P/S), Lyso Tracker red, Annexin V-FITC/Propidium Iodide (PI) apoptosis assay kit and real-time superoxide fluorescent assay kit were purchased from Thermo Fisher Scientific. Superoxide detecting reagent was purchased from Enzo life science. Glutathione (GSH) colorimetric assay kit was purchased from BioVision.

Synthetic manipulations that required an inert atmosphere (where noted) were carried out under nitrogen using standard Schlenk techniques. Powder X-ray diffraction (PXRD) was carried out on a Bruker D8-Focus Bragg-Brentano X-ray powder Diffractometer equipped with a Cu sealed tube (λ = 1.54178) at 40 kV and 40 mA. N2 sorption isotherms at 77 K were measured by using a Micrometritics ASAP 2420 system with high-purity grade (99.999%) of gases. UV-Vis spectra were recorded on Shimadzu UV-2450 spectrophotometer. Fluorescence spectra were recorded on a Hitachi F- 4600 spectrometer (Hitachi Co. Ltd., Japan) with Xe lamp as the excitation source at room temperature. Dynamic light scattering and Zeta potential were measured at 25 °C on a Zetasizer Nano ZS ZEN3600 analyser (Malvern Instrument Ltd, UK). Confocal laser scanning microscopy (CLSM) imaging was performed on an inverted epifluorescence microscope (Model IX81, Olympus) was equipped with a heating stage maintained at 37 °C. Images were collected using a Rolera-MGI Plus back-illuminated electron-multiplying charge coupled device (EMCCD) camera (Qimaging). Images were acquired using bright-field imaging and three standard fluorescence filter sets: DAPI (excitation (E_x) = 350 ± 10 nm/emission (E_m) = 440 ± 20 nm), RFP (E_x = 560 ± 20 nm/E_m = 630 ± 35 nm) and FITC (E_x = 488 ± 10 nm/E_m = 520 ± 20 nm). The fluorescence intensities of different cells were measured with the SlideBook 4.2 software (Olympus). For

fluorescence measurement using the flow cytometer, cells were trypsinized and resuspended in nrL-15 medium. Cells were analyzed using a BD Accuri C6 flow cytometer equipped with the FL2 filter (excitation = 488 nm/emission = 533 ± 30 nm). All data were acquired at a flow rate of 66 μl/min with detection of a minimum of 40,000 events. The data was processed using Flowjo software.

HeLa (ATCC CCL-2) were grown in DMEM supplemented with FBS and P/S and kept at 37 °C in a humidified atmosphere containing 5% CO_2. SKOV3-TR (ATCC HTB-77) and H1299 (ATCC CRL-5803) were grown in RMPI 1640 supplemented with FBS and P/S and kept at 37 °C in a humidified atmosphere containing 5% CO_2. Cell experiments are performed in quintuplicates for each condition, and are repeated with three different batches of cells. Statistic tests are studied by multiple t tests method.

Female BALB/c nude mice (5–6 weeks) were purchased from Vital River Laboratories (Beijing, China). All animal experiments were performed in accordance with the Guide for the Care and Use of Laboratory Animals, and were approved by the Experimental Animal Ethics Committee in Beijing. Mice were subcutaneously injected with HeLa cells (3×10^7 /mL, 200 μL) at the flank. After the tumor volume reached ~50 mm^3, the mice were randomly divided to 5 groups, with five mice in each group. The tumor-bearing mice in the 5 groups were treated with PBS, APAP, TYR@NPCN-333, TYR@NPCN-333 – APAP, and TYR@NPCN-333 – APAP + GSH, respectively every day via intratumor injection (100 μL). Tumor volume were measured every day and calculated by Tumor volume = (length × $width^2$)/2. On day 7, mice were euthanized. The tumor tissues of each mice were collected and finally fixed in formalin. Hematoxylin and eosin (H&E) staining of the tissues was performed according to standard protocol.

5.2.2 Synthesis of NPCN-333

10 mL DMF solution of $AlCl_3 \cdot 6H_2O$ (1.5 mg/mL), 5 mL DMF solution of TATB (1 mg/mL), 15 mL DMF and 50 μL TFA was mixed and heated at 95ºC for 24 h. NPCN-333 was collected by centrifugation.

5.2.3 Synthesis of FNPCN-333

30 mg NPCN-333 was dispersed in 5 mL DMF in which was added 5 mL 10 mg/mL DMF solution of BTB-Green. The mixture was kept in 85ºC oven for 4 h and the solid was collected by centrifugation. The precipitated solid was washed with fresh DMF for 3 times and resuspended in fresh DMF.

5.2.4 Encapsulation of TYR on NPCN-333

Stock solutions of TYR (3 mg/mL) was prepared by dissolving TYR in deionized water. 1 mg NPCN-333 was suspended in water in which 1 mL TYR stock solution was added. The mixture was vortexed for 20 minutes and the solid was collected by centrifugation and washed by fresh water for 3 times.

5.2.5 Theoretical estimation of enzyme loading in NPCN-333

In each unit cell of PCN-333, there are eight of A-cages (5.5 nm) and 16 of B-cages (4.2 nm). The volume of each unit cell = $(126\ Å)^3 = 2.0 \times 10^{-18}\ cm^3$. The density of PCN-333(Al) = $0.23\ g/cm^3$. So the mass of each unit cell = $\rho \times V = 0.46 \times 10^{-18}$ g. Therefore, the total number of unit cells per gram of PCN-333(Al) is: $1/(0.46 \times 10^{-18}) = 2.2 \times 10^{18}$. And the A-cage in each gram of PCN-333(Al) = $2.2 \times 10^{18} \times 8 = 1.7 \times 10^{19} = 2.9 \times 10^{-5}$ mol. For TYR, M_W = 43 kDa, so the maximum loading is $43000 \times 2.9 \times 10^{-5} = 1.075$ g/g.

5.2.6 Enzymatic activity study

In 50 mM pH 6.8 Tris-HCl buffer at ambient temperature containing various concentrations of APAP (0.2 – 2mM), free TYR or TYR@NPCN-333 was added and a final concentration of 60 μg/mL TYR was obtained. The readings at 450 nm were collected every two minutes and were plotted to determine the conversion rate at each substrate concentration. Then the results were fit by Michaelis-Menten model and k_{cat} was calculated by $v_{max}/[E_0]$. E_0 stands for the concentration of enzyme.

5.2.7 Long-term persistence of enzymatic activity of TYR@NPCN-333

Free TYR and TYR@NPCN-333 was incubated with SKOV3-TR for 6 h on day 0, respectively. The cells were then cultured with fresh RPMI 1640 medium for several days. The culture medium was replaced with medium containing APAP on day 1 (free TYR) or on day 3 (TYR@NPCN-333) and cultured for 24 h. Cell viability was measured by MTT assay.

5.2.8 Cell internalization of TYR@FNPCN-333 and CLSM imaging

SKOV3-TR cells were seeded in an 8 well plate and allowed to grow for 24-48 h. Then the culture media was replaced by 200 μL fresh nrL-15 media containing 75 μg/mL TYR@FNPCN-333 at 37ºC for 6 h in darkness. Culture media was removed and the cells were washed with fresh nrL-15 media for 3 times. Lyso Tracker red was added before the cells were subjected to microscope.

5.2.9 MTT assay for viability determination

Cells were seeded in 96 well plate and subjected to certain treatments. Then culture media was removed and the cells were washed with fresh PBS buffer for 3 times. 100 μL fresh RPMI 1640 buffer was added to each well followed by the addition of MTT

stock solution. The final MTT concentration is 0.5 mg/mL. The plate was incubated at 37°C for 4 h. 100 μL SDS-HCl (10 mM) stock solution was added to each well and the plate was incubated at 37°C for another 12 h. The solution in each well was mixed and the absorbance at 560 nm was collected on a plate reader.

5.2.10 Annexin V-FITC/PI assay for determining the apoptotic status of cells by flow cytometry

Cells were seeded in 48 well plate and subjected to certain treatments. Then the cells were trypsinized and washed with cold PBS buffer for three times collected by centrifugation. Cells were treated with 5% annexin V-FITC and 100 μg/mL PI in binding buffer for 15 minutes at room temperature before subjected to flow cytometry for analysis.

5.2.11 Intracellular ROS monitoring

Cells were seeded in 48 well plate and subjected to certain treatments. Then the culture media was removed and the cells were cultured in fresh RPMI 1640 media containing 20 μM superoxide detecting reagent for 15 minutes. The cells were then imaged using a confocal microscope.

5.2.12 Intracellular GSH concentration measurement

This measurement is followed by the protocol from BioVision. Cells were seeded in 6-well plate (1-1.5 × 10^6 cells per well) and were allowed to adhere overnight. The cells were treated by desired methods. Collect the cells by centrifugation at 700 × g for 5 minutes at 4°C. Remove the supernatant. Wash the cells with ice cold PBS. Lyse the cells in 80 μL ice cold glutathione buffer. Incubated on ice for 10 minutes. Add 20 μL 5%

sulfosalicylic acid (SSA) solution, centrifuge and remove the pellet. Use the supernatant for glutathione assay.

Prepare NADPH generation solution by mixing 20 µL NADPH generating mix, 20 µL glutathione reductase and 120 µL glutathione reaction buffer in a 96-well plate and wait for 10 minutes at room temperature. Add 20 µL GSH standard solution or sample solution and incubate the plate for 5-10 minutes. Add 20 µL of DNTB solution and incubate for another 5-10 minutes. Read the absorbance at 405 nm using a microplate reader. Determine concentrations of GSH in the sample solutions using the standard curve.

5.3 Results and Discussion

PCN-333 is composed of trimeric-oxo cluster and a planar triangular ligand, 4,4′,4″-s-triazine-2,4,6-triyl-tribenzoic acid (TATB), which self-assembles into a supertetrahedron (STH) with metal clusters on the corner and TATB on the face (Figure V-1). A 1.5 nm cavity is present in the STH. Two types of mesoporous cavities with diameters of 4.2 and 5.5 nm are composed of STHs through vertex sharing. PCN-333

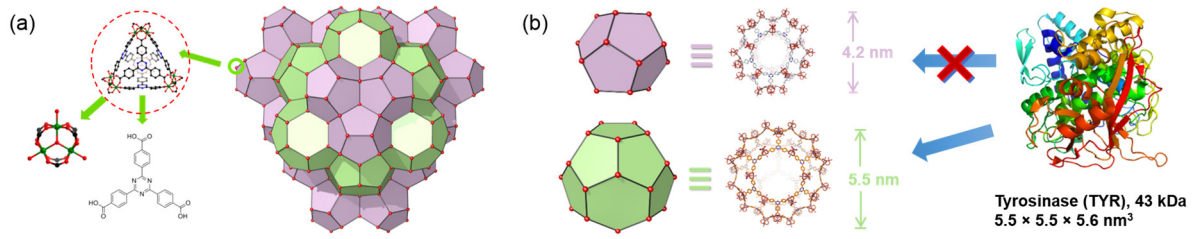

Figure V-1. Structure of PCN-333. (a) NPCN-333 is composed of aluminum trimeric cluster and TATB ligand, which self-assembles into supertetrahedrons as the secondary building block of NPCN-333. (b) Two types of mesoporous cavities in NPCN-333: 4.2 nm dodecahedral cage (light purple) and 5.5 nm hexacaidecahedral cage (light green). Based on the size of tyrosinase, it can only be accommodated in the 5.5 nm cage.

nanoparticles (NPCN-333) were prepared by solvothermal reaction of $AlCl_3$ and TATB in DMF at 95°C. The particle size determined by transmission electron microscopy (TEM) was around 100 nm (Figure V-2). A fluorescent version of NPCN-333 was prepared via a ligand metathesis reaction with a BTB ligand functionalized with a green fluorescent BODIPY fluorophore. The well-maintained crystallinity of NPCN-333 after enzyme loading and after soaking in cell culture medium Roswell Park Memorial Institute 1640

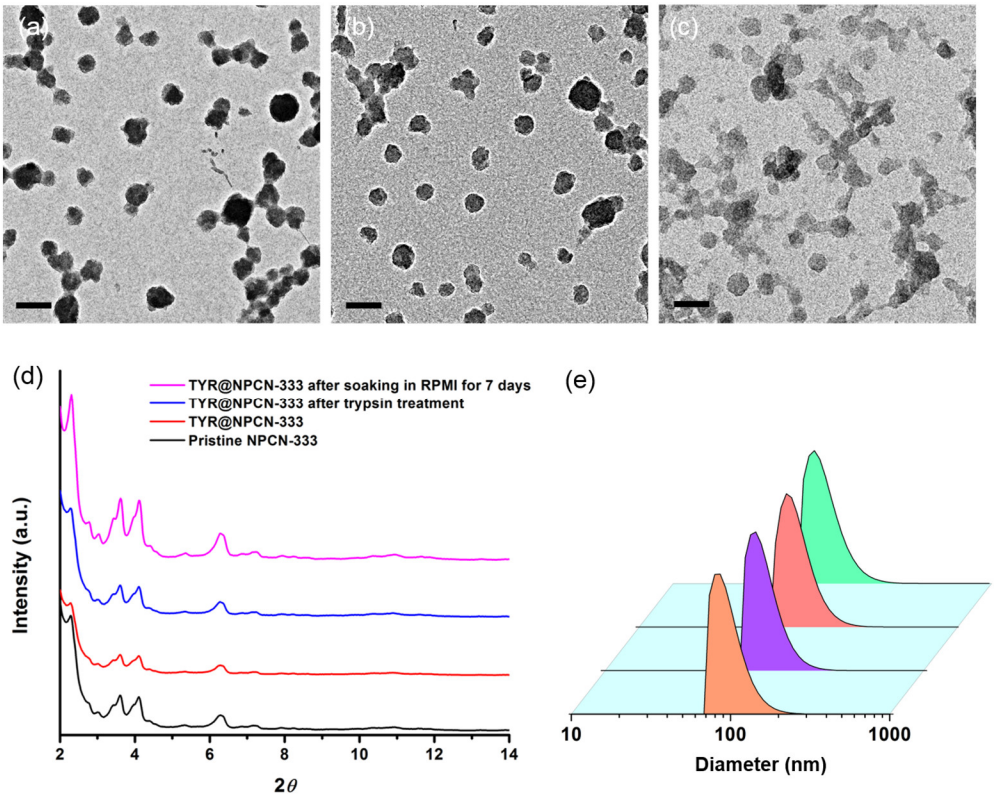

Figure V-2. Structural characterization of NPCN-333. TEM images of NPCN-333 (a), TYR@NPCN-333 (b), and TYR@NPCN-333 after soaking in RPMI-1640 for 7 days (c). Scale bar: 200 nm. (d) Powder X-ray diffraction (PXRD) patterns of pristine NPCN-333 (black), TYR@NPCN-333 (red), TYR@NPCN-333 after trypsin treatment (blue), and TYR@NPCN-333 after soaking in RPMI 1640 media for 7 days (magenta). (e) Particle size distribution measured by dynamic light scattering (DLS): (from front to back) pristine NPCN-333, TYR@NPCN-333, TYR@NPCN-333 after trypsin treatment, and TYR@NPCN-333 after soaking in RPMI 1640 media for 7 days.

(RPMI 1640) for up to 7 days was confirmed by the TEM images and by the nearly unchanged PXRD pattern (Figure V-2). The monodispersity of NPCN-333 immersed in RPMI 1640 over an extended period of time was verified by the particle size distribution diagram derived from dynamic light scattering (DLS) data collected on day 0 and day 7 (Figure V-2).

One molecule of TYR contains a single 43 kDa polypeptide with dimension of 5.5 × 5.5 × 5.6 nm^3.[303] Therefore TYR may be accommodated in the 5.5 nm cavity, but presumably not in the 1.5 and 4.2 nm cavity. After incubating TYR with NPCN-333 slurry for 20 minutes, the enzyme loading capacity was estimated to be 0.80 g/g according to BCA method, which is in consistent with the theoretical value (1.08 g/g). The distribution of TYR in the material was studied by N_2 isotherm at 77K. The pore size distribution diagram of TYR encapsulated NPCN-333 (TYR@NPCN-333) clearly showed the presence of a microporous cavity around 1.5 nm and a mesoporous cavity at around 4 nm. Notably, the 5 nm cavity disappeared, consistent with the cavity being occupied by TYR. Thermal gravimetric analysis (TGA) also indicated the high loading of TYR in NPCN-333.

TYR catalyzes the oxidation of APAP to an *o*-quinone compound, 4-acetamido-*o*-benzoquinone (AOBQ), which absorbs at 450 nm. The enzymatic activities of free TYR and TYR@NPCN-333 nanoreactor in 50 mM Tris-HCl buffer (pH 6.8) at ambient temperature, was monitored by UV-vis spectrometry. TYR@NPCN-333 nanoreactor followed Michaelis-Menten kinetics and showed a k_{cat} value of 0.377 s^{-1} and a K_m value of 1.119 mM. In comparison, the free enzyme displayed a k_{cat} of 0.405 s^{-1} and a K_m of

1.338 mM. The catalytic efficiencies, k_{cat}/K_m, were 0.302 $s^{-1}mM^{-1}$ for free TYR vs. 0.337 $s^{-1}mM^{-1}$ for TYR@NPCN-333.

Resistance of enzyme-MOF nanoreactor towards degradation is critical for practical applications in living biosystems. To elucidate whether NPCN-333 could protect encapsulated TYR, free TYR and TYR@NPCN-333 were incubated with trypsin solution for 2 hours at 37°C. Then, the enzyme was released by dissolving TYR@NPCN-333 with HCl and the supernatant was subjected to SDS-PAGE analysis. Free TYR was readily digested by trypsin as illustrated by the presence of small molecular weight bands. In contrast, bands corresponding to intact TYR were predominantly present for TYR@NPCN-333. Additionally, the enzymatic activity of TYR@NPCN-333 was almost unchanged after trypsin treatment (Figure V-3). Moreover, in order to study whether MOF protect encapsulated enzymes in an acidic medium, free TYR and TYR@NPCN-333 were incubated in pH 5 buffer, and enzymatic activities were measured at 2 h and 12 h. While a 2 h incubation only resulted in a 15% activity loss on free enzyme, 75% of the

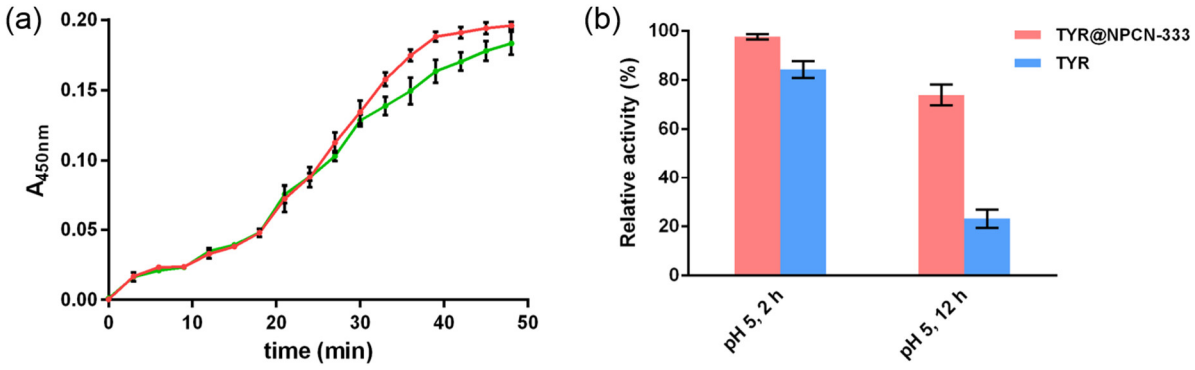

Figure V-3. Long-persistent enzymatic activity of TYR@NPCN-333 under perturbations. (a) AOBQ generation catalyzed by TYR@NPCN-333 before (red) and after (green) trypsin digestion. (b) Relative enzymatic activities (compared with activities in pH 5 at 0 h) of TYR@NPCN-333 and free TYR after incubating in pH 5 solution for 2 h and 12 h.

original activity was lost after 12 h incubation. In contrast, TYR@NPCN-333 maintained over 75% activity after 12 h incubation at pH 5 (Figure V-3).

In vitro results indicated that TYR@NPCN-333 is enzymatically active and relatively resistant to perturbations. Cell-based experiments were therefore conducted to examine whether TYR@NPCN-333 could activate APAP in cancer cells. To test the performance of TYR@NPCN-333, we chose SKOV3-TR, an ovarian adenocarcinoma cell that is resistant to cisplatin, tumor necrosis factor, diphtheria toxin, adriamycin, and taxane.[304-306] First, the cellular internalization of the enzyme-MOF nanoreactor was established using confocal microscopy. A fluorescent particle, TYR@FNPCN-333, was used to monitor cellular trafficking. After incubation with cells, TYR@FNPCN-333

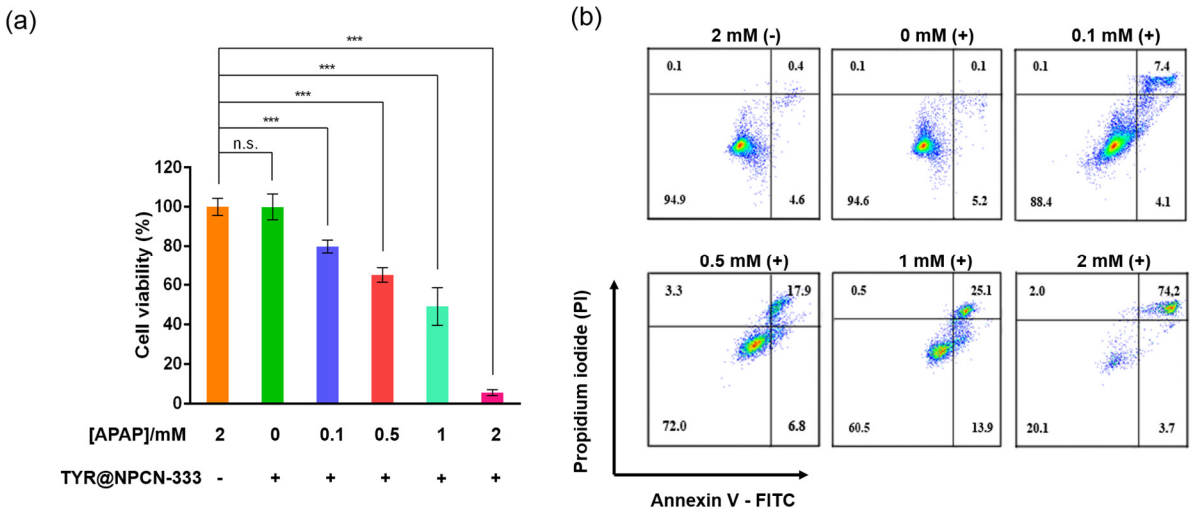

Figure V-4. Cytotoxicity of TYR@NPCN-333 – APAP. (a) Cell proliferation of SKOV3-TR cells upon different treatments measured by MTT assay. The experiment was performed in quintuplicate in 96 well plates (n = 5), mean ± s.d., *** represents $p \leq 0.001$, multiple t test. (b) Cell viability of SKOV3-TR cells stained with annexin V-FITC/propidium iodide (PI) and measured by flow cytometry after different treatments. Cells with (+) or without (-) 6 h TYR@NPCN-333 pretreatment was incubated with 0—2 mM APAP for 2 h. The experiment was performed three times and representative results from one test are displayed.

displayed an intracellular punctate distribution around the nucleic area that colocalizes with LysoTracker, a marker for late endosomes and lysosomes.[307] This indicates that the nanoreactor accumulated within endocytic organelles. Next, the cytotoxicity induced by TYR@NPCN-333 was quantified by the MTT assay. The prodrug, or the enzyme-MOF nanoreactor, did not display any noticeable cytotoxicity (Figure V-4). In contrast, cells that were pretreated with TYR@NPCN-333 for 6 h, and then subsequently exposed to increasing concentrations of APAP (0.1 to 2 mM) displayed a correlated decrease in viability. In complementary assays, the cytotoxicity of the TYR@NPCN-333 – APAP combination was assessed by flow cytometry. After different treatments, cells were stained with annexin V-FITC, a fluorescent marker of surface exposed phosphatidyl serine, and with propidium iodide (PI), a DNA stain that detects the permeabilization of the plasma membrane. As observed previously, neither APAP nor TYR@NPCN-333

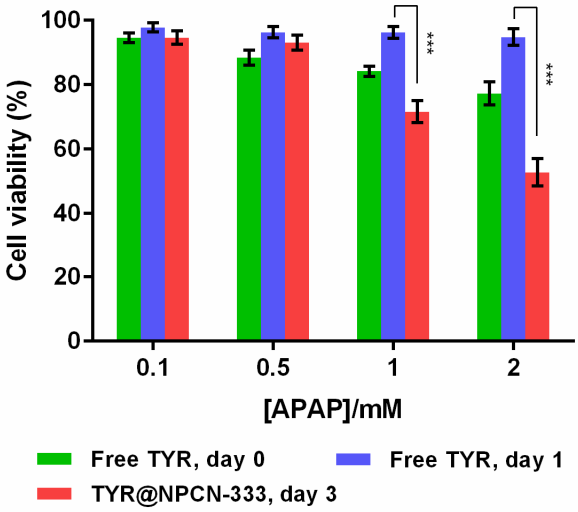

Figure V-5. Long-term persistence of enzymatic activity of TYR@NPCN-333. The experiment was performed in quintuplicate in 96 well plates (n = 5), mean ± s.d., *** represents $p \leq 0.001$, multiple t test.

caused an increase in annexin V or PI staining, indicating that these conditions are not toxic to cells (Figure V-4). However, cells pretreated with TYR@NPCN-333 and exposed to APAP displayed dual labeling, which is indicative of cell death.

Because activating enzymes must be administered before treatment with a prodrug, it is important to ensure that their activity can be maintained over a prolonged period of time.[308] To study how the enzyme-MOF nanoreactor performs in this respect, SKOV3-TR cells pretreated with TYR@NPCN-333 for 6 h were cultured in fresh media for several days. MTT assay revealed that a 2 mM APAP treatment on day 3 could lead to 50% cell proliferation inhibition (Figure V-5). On the contrary, free TYR showed slight inhibition effect (<20%) on cells after APAP treatment on day 0. However, the activity of free TYR totally disappeared from day 1. Besides, similar cytotoxicity was observed in other cancer cell lines, including non-small lung carcinoma cell H1299 and cervical carcinoma cell HeLa.

Next, we sought to characterize how TYR@NPCN-333 – APAP induces toxicity. When used as the sole therapeutic, neither TYR@NPCN-333 nor APAP display cytotoxicity. We hypothesized that the cytotoxicity observed was a result of the *in situ* generation of AOBQ as an enzymatic product. Based on the property of *p*-quinone compounds, we suspected that AOBQ would undergo single electron redox reactions and induce the generation of reactive oxygen species (ROS) in cells.[309-312] Real-time monitoring of superoxide (O_2^-) concentration using a superoxide detection reagent in SKOV3-TR cells upon different treatments was performed to test this hypothesis. The intensity of red fluorescence is proportional to the concentration of intracellular O_2^-. Cells treated with TYR@NPCN-333 – APAP displayed elevated levels of O_2^- whereas the O_2^-

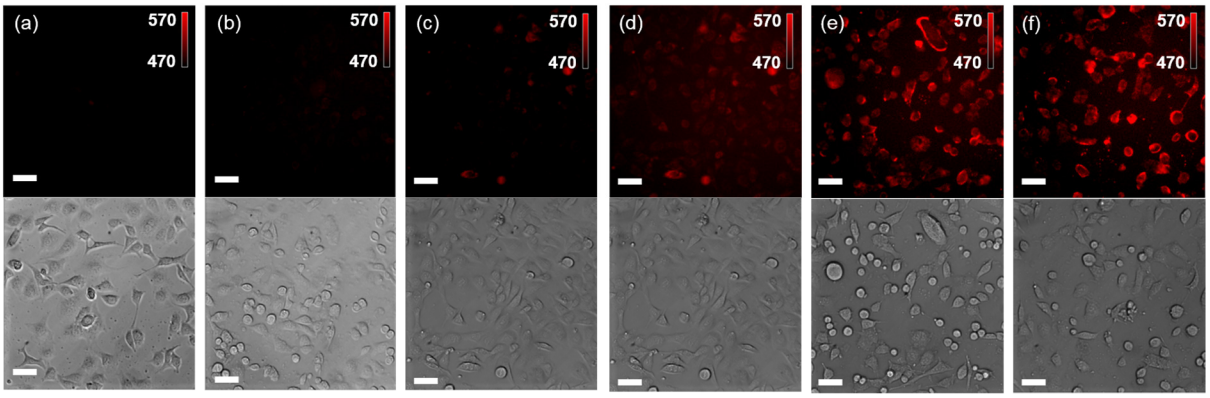

Figure V-6. Real-time monitoring of intracellular superoxide generation. (a) 2 mM APAP 2 h. (b)-(f) Cells were pretreated with TYR@NPCN-333 for 6 h, then incubated with (b) 0 mM, (c) 0.1 mM, (d) 0.5 mM, (e) 1 mM, (f) 2 mM APAP for 2 h. The concentration of superoxide is proportional to the intensity of red fluorescence. The experiment was performed three times and representative results from one test are displayed. Scale bar: 50 μm.

level in cells treated with either TYR@NPCN-333 or APAP remained unchanged (Figure V-6).

Besides inducing ROS generation, *o*-quinone compounds are notorious for consuming glutathione (GSH) in living cells.[313, 314] Therefore we sought to measure the GSH concentration in cells upon TYR@NPCN-333 – APAP treatments. GSH reacts with DNTB (5,5'-dithio-bis-2-(nitrobenzoic acid) and produces a yellow colored compound (5-thio-2-nitrobenzoic acid), which can be quantitatively measured by UV-vis spectroscopy at 405 nm.[315] Because GSH is the most abundant non-protein thiol in eukaryotic cells, this measurement yields a good estimation on intracellular GSH concentration.[316] GSH level remained unchanged in cells treated with either TYR@NPCN-333 or APAP. However, when cells were pretreated with TYR@NPCN-333 for 6 h, treatment with APAP solution resulted in GSH depletion, which showed a strong correlation with APAP concentration (Figure V-7). Notably, after 2 mM APAP

treatment for only 2 h, intracellular GSH concentration decreased to about 50% of its original level (cells were not permeabilized at this time point, as proved by absence of PI staining). Mass spectrometry analysis of the cell lysate revealed the presence of a species with molecular weight of 492, which is in consistent with that of APAP-GSH conjugate (Figure V-7).[313] In addition, to further confirm the role of ROS generation and GSH depletion in AOBQ induced cytotoxicity, we did two control experiments in which ascorbic acid (AA) and GSH were supplemented to cell culture medium along with TYR@NPCN-333 – APAP treatment (APAP concentration was 500 μM). Compared with the negative control group, the cell viability showed 20% and 30% increase for AA and GSH supplement groups, respectively. Overall, these results have established that TYR@NPCN-333 – APAP exhibits cytotoxicity by inducing oxidative stress, as manifested by a combination of ROS induction and GSH depletion.

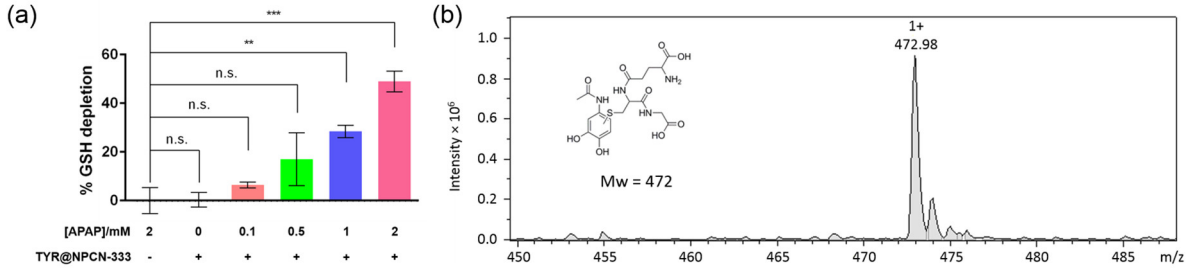

Figure V-7. GSH depletion in SKOV3-TR cells. (a) Intracellular GSH depletion upon various treatments for 2 h determined by DNTB assay. The experiment was performed in quintuplicate in 96-well plates (n = 5), mean ± s.d., ** represents p ≤0.01, *** represents p≤0.001, multiple t test. (b) Mass spectrometry of APAP-GSH adduct. The inlet molecular structure is the proposed APAP-GSH adduct.

To evaluate the antitumor efficacy of APAP in the presence of MOF nanoreactor, *in vivo* experiments were performed on a HeLa subcutaneous xenograft model. Mice were

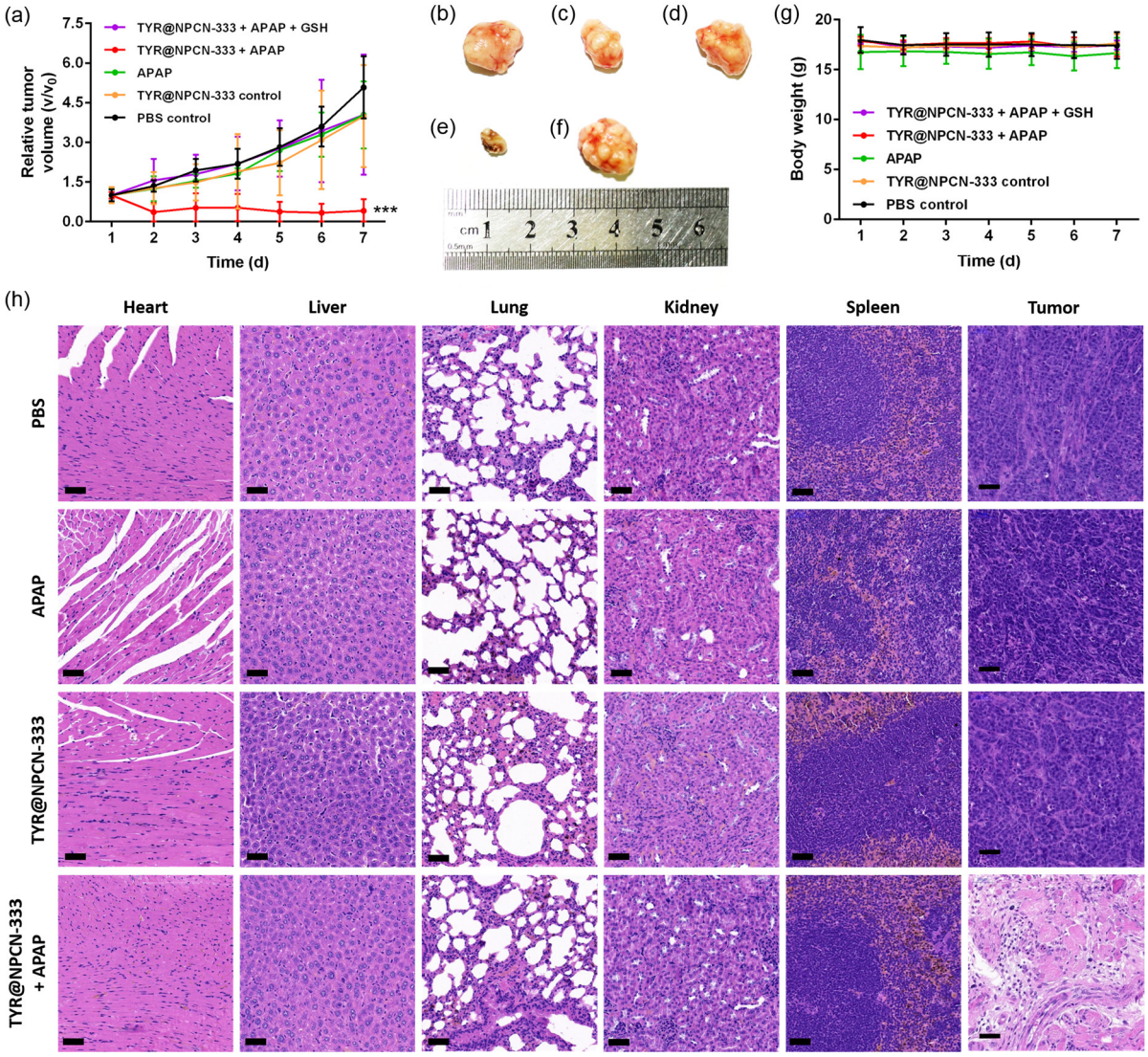

Figure V-8. *In vivo* antitumor efficiency of TYR@NPCN-333 – APAP. (a) Time-dependent relative tumor growth upon different treatments. The experiment was performed on five bilateral tumour-bearing mice (n = 5), mean ± s.d., *** represents $p \leq 0.001$, multiple t test. (b)-(f) Tumor images at day 7 upon different treatments: (b) PBS, (c) APAP, (d) TYR@NPCN-333, (e) APAP + TYR@NPCN-333, (f) APAP + TYR@NPCN-333 + GSH. The experiment was performed on five bilateral tumour-bearing mice (n = 5) and representative results from one test are displayed. (g) Body weights during 7 days upon different treatments. (h) Representative H&E-stained sections of different organs collected at day 7 upon different treatments. Scale bar: 50 μm.

treated with PBS, TYR@NPCN-333 (1.5 mg/kg), APAP (200 mg/kg), TYR@NPCN-333 (1.5 mg/kg) and APAP (200 mg/kg), respectively. Compared with PBS control, tumor regression only occurred in the group receiving TYR@NPCN-333 – APAP treatment (tumor size decreased from ~50 to ~20 mm^3), while neither the nanoreactor nor the prodrug alone induced any antitumor efficacy (Figure V-8). More importantly, in the TYR@NPCN-333 – APAP group, two out of five tumors were completely eradicated by the end of the experiment upon a single treatment. Additionally, tumor regression failed in mice treated with TYR@NPCN-333 – APAP but supplemented with GSH (700 mg/kg), further confirming that tumor regression is attributable to oxidative stress. Hematoxylin and eosin (H&E) staining of tumor tissues showed that only the group receiving TYR@NPCN-333 – APAP therapy demonstrated cell apoptosis/necrosis (Figure V-8).

5.4 Conclusion

In summary, we demonstrate that the enzyme-MOF nanoreactor can be a highly efficient activator for resistant cancer therapy coupled with a prodrug. Encapsulated enzymes are well protected by MOFs in proteolytic conditions and in acidic environment, where free enzymes would quickly lose activity. The prodrug can be efficiently activated by the enzyme-MOF nanoreactor, generating a cytotoxic compound, which inhibits cell proliferation and induces apoptosis/necrosis by promoting oxidative stress. *In vivo* experiment shows a 2.5-time regression of tumor volume after a single treatment. Overall, we envision that the enzyme-MOF nanoreactor system as a new platform for vast biomedical and biotechnological applications due to the ability to cater for intrinsic diversities in structure and functionality.

CHAPTER VI

CONCLUSION

The majority of this dissertation described the development of novel enzyme-MOF nanoreactors and their applications in cell biology and biomedical aspects. Based on a hierarchical mesoporous structure, namely PCN-333, isoreticular chemistry resulted in the successful preparation of a novel hierarchical mesoporous MOF, PCN-888, possessing extremely large cage cavitiess. Because of its hierarchical porosity, two enzymes with different sizes could be coupled as a tandem nanoreactor based on size selectivity. The relatively small window opening of the cage cavity prevented enzyme leaching and protected encapsulated enzymes from trypsin digestion.

Owing to the better chemical stability of PCN-333 than PCN-888, a fluorescent bi-enzymatic nanofactory was obtained based on PCN-333 nanoparticles. Fluorescent ligand was anchored on the framework backbone *via* ligand metathesis. This nanofactory contained two antioxidant enzymes: superoxide dismutase (SOD) and catalase (CAT). Encapsulated enzymes remained active in conditions mimicking that of lysosomes, intracellular organelles that are highly degradable and with low pH values. The nanofactory could be endocytosed by different types of cells (human cancer, human primary, mice primary), accumulated in lysosomes and could protect cells from oxidative damage for as long as seven days.

The above proof-of-concept work provided opportunity for long-persistent biomedical applications of enzyme-MOF nanoreactors. Inspired by the superior enzyme protection capability of PCN-333, tyrosinase enzyme was encapsulated on PCN-333 nanoparticles and a cancer therapeutic nanoreactor was generated. When endocytosed by

cancer cells, encapsulated tyrosinase was able to catalyse the oxidation of nontoxic prodrug paracetamol, the active ingredient of Tylenol®, generating cytotoxic *o*-quinone compound, which demonstrated anticancer efficacy in several cancer cells, including a multi-drug resistant cancer cell line (SKOV3-TR). Mechanistically, *o*-quinone induced superoxide generation and antioxidant depletion in cancer cells. The anticancer efficacy of this prodrug activation strategy was confirmed on mice model bearing human tumor xenograft. Although the current version of enzyme-MOF nanoreactor did not show tumor specific accumulation, surface modifications with tumor directing peptide will potentially generate tumor targeting nanoreactors, which may significantly reduce the side effect of the cytotoxins.

Although nanoreactors based on PCN-333 demonstrated long-term chemical stability in aqueous solutions, it is still desirable to develop more robust MOFs with even longer persistence in physiological conditions or with stability to sustain oral administration. However, the stability of many MOFs decreases along with the increase of surface area, although these MOFs are composed of high valent metal species. To address this issue, synthesizing MOFs with Cr(III) species may gain extra stability because of the kinetic inertness of Cr(III). On the other hand, inert Cr(III) species hinders both the direct synthesis of Cr(III)-MOFs and direct metal metathesis of trivalent MOF templates and Cr(III) ions. Herein a reductive labilization strategy for the facile synthesis of mesoporous Cr(III)-MOF was discovered. Using Fe(III)-MOF as the template and Cr(II) ions as the metal source, Cr(II) could reduce Fe(III) on the framework backbone, generating Fe(II) species which is much more labile than its trivalent counterpart. Then Cr(II) could replace Fe(II) on the framework and was oxidized to Cr(III) immediately

when it was exposed to air. Cr(III)-MOF demonstrated much wider pH tolerance (0~11) than the Fe(III)-MOF template (3~9) and could accommodate polyethylenimine for carbon capture.

REFERENCES

1. S. Kitagawa, R. Kitaura and S.-i. Noro, *Angew. Chem. Int. Ed.*, **2004**, *43*, 2334-2375.
2. H. Li, M. Eddaoudi, M. O'Keeffe and O. M. Yaghi, *Nature*, **1999**, *402*, 276.
3. J. Rouquerol, D. Avnir, C. W. Fairbridge, D. H. Everett, J. M. Haynes, N. Pernicone, J. D. F. Ramsay, K. S. W. Sing and K. K. Unger, in *Pure Appl. Chem.*, 1994, vol. 66, p. 1739.
4. K. Adil, Y. Belmabkhout, R. S. Pillai, A. Cadiau, P. M. Bhatt, A. H. Assen, G. Maurin and M. Eddaoudi, *Chem. Soc. Rev.*, **2017**, *46*, 3402-3430.
5. M. D. Allendorf, C. A. Bauer, R. K. Bhakta and R. J. T. Houk, *Chem. Soc. Rev.*, **2009**, *38*, 1330-1352.
6. H. Assi, G. Mouchaham, N. Steunou, T. Devic and C. Serre, *Chem. Soc. Rev.*, **2017**, *46*, 3431-3452.
7. E. Barea, C. Montoro and J. A. R. Navarro, *Chem. Soc. Rev.*, **2014**, *43*, 5419-5430.
8. N. S. Bobbitt, M. L. Mendonca, A. J. Howarth, T. Islamoglu, J. T. Hupp, O. K. Farha and R. Q. Snurr, *Chem. Soc. Rev.*, **2017**, *46*, 3357-3385.
9. D. Bradshaw, S. El-Hankari and L. Lupica-Spagnolo, *Chem. Soc. Rev.*, **2014**, *43*, 5431-5443.
10. C. K. Brozek and M. Dinca, *Chem. Soc. Rev.*, **2014**, *43*, 5456-5467.
11. J. Canivet, A. Fateeva, Y. Guo, B. Coasne and D. Farrusseng, *Chem. Soc. Rev.*, **2014**, *43*, 5594-5617.
12. N. Chaoui, M. Trunk, R. Dawson, J. Schmidt and A. Thomas, *Chem. Soc. Rev.*, **2017**, *46*, 3302-3321.
13. Y. J. Colon and R. Q. Snurr, *Chem. Soc. Rev.*, **2014**, *43*, 5735-5749.

14. A. U. Czaja, N. Trukhan and U. Muller, *Chem. Soc. Rev.*, **2009**, *38*, 1284-1293.

15. P. Deria, J. E. Mondloch, O. Karagiaridi, W. Bury, J. T. Hupp and O. K. Farha, *Chem. Soc. Rev.*, **2014**, *43*, 5896-5912.

16. T. Devic and C. Serre, *Chem. Soc. Rev.*, **2014**, *43*, 6097-6115.

17. A. Dhakshinamoorthy and H. Garcia, *Chem. Soc. Rev.*, **2014**, *43*, 5750-5765.

18. T. Duren, Y.-S. Bae and R. Q. Snurr, *Chem. Soc. Rev.*, **2009**, *38*, 1237-1247.

19. M. Eddaoudi, D. F. Sava, J. F. Eubank, K. Adil and V. Guillerm, *Chem. Soc. Rev.*, **2015**, *44*, 228-249.

20. J. D. Evans, K. E. Jelfs, G. M. Day and C. J. Doonan, *Chem. Soc. Rev.*, **2017**, *46*, 3286-3301.

21. J. D. Evans, C. J. Sumby and C. J. Doonan, *Chem. Soc. Rev.*, **2014**, *43*, 5933-5951.

22. P. Falcaro, R. Ricco, C. M. Doherty, K. Liang, A. J. Hill and M. J. Styles, *Chem. Soc. Rev.*, **2014**, *43*, 5513-5560.

23. G. Ferey and C. Serre, *Chem. Soc. Rev.*, **2009**, *38*, 1380-1399.

24. S. Furukawa, J. Reboul, S. Diring, K. Sumida and S. Kitagawa, *Chem. Soc. Rev.*, **2014**, *43*, 5700-5734.

25. W.-Y. Gao, M. Chrzanowski and S. Ma, *Chem. Soc. Rev.*, **2014**, *43*, 5841-5866.

26. V. Guillerm, D. Kim, J. F. Eubank, R. Luebke, X. Liu, K. Adil, M. S. Lah and M. Eddaoudi, *Chem. Soc. Rev.*, **2014**, *43*, 6141-6172.

27. S. S. Han, J. L. Mendoza-Cortes and W. A. Goddard Iii, *Chem. Soc. Rev.*, **2009**, *38*, 1460-1476.

28. Y. Han, J.-R. Li, Y. Xie and G. Guo, *Chem. Soc. Rev.*, **2014**, *43*, 5952-5981.

29. Y. He, B. Li, M. O'Keeffe and B. Chen, *Chem. Soc. Rev.*, **2014**, *43*, 5618-5656.

30. Y. He, W. Zhou, G. Qian and B. Chen, *Chem. Soc. Rev.*, **2014**, *43*, 5657-5678.

31. Z. Hu, B. J. Deibert and J. Li, *Chem. Soc. Rev.*, **2014**, *43*, 5815-5840.

32. T. Kitao, Y. Zhang, S. Kitagawa, B. Wang and T. Uemura, *Chem. Soc. Rev.*, **2017**, *46*, 3108-3133.

33. M. Kurmoo, *Chem. Soc. Rev.*, **2009**, *38*, 1353-1379.

34. J. Lee, O. K. Farha, J. Roberts, K. A. Scheidt, S. T. Nguyen and J. T. Hupp, *Chem. Soc. Rev.*, **2009**, *38*, 1450-1459.

35. J.-R. Li, R. J. Kuppler and H.-C. Zhou, *Chem. Soc. Rev.*, **2009**, *38*, 1477-1504.

36. Z.-J. Lin, J. Lu, M. Hong and R. Cao, *Chem. Soc. Rev.*, **2014**, *43*, 5867-5895.

37. J. Liu, L. Chen, H. Cui, J. Zhang, L. Zhang and C.-Y. Su, *Chem. Soc. Rev.*, **2014**, *43*, 6011-6061.

38. J. R. Long and O. M. Yaghi, *Chem. Soc. Rev.*, **2009**, *38*, 1213-1214.

39. W. Lu, Z. Wei, Z.-Y. Gu, T.-F. Liu, J. Park, J. Park, J. Tian, M. Zhang, Q. Zhang, T. Gentle Iii, M. Bosch and H.-C. Zhou, *Chem. Soc. Rev.*, **2014**, *43*, 5561-5593.

40. W. P. Lustig, S. Mukherjee, N. D. Rudd, A. V. Desai, J. Li and S. K. Ghosh, *Chem. Soc. Rev.*, **2017**, *46*, 3242-3285.

41. L. Ma, C. Abney and W. Lin, *Chem. Soc. Rev.*, **2009**, *38*, 1248-1256.

42. G. Maurin, C. Serre, A. Cooper and G. Ferey, *Chem. Soc. Rev.*, **2017**, *46*, 3104-3107.

43. R. Medishetty, J. K. Zareba, D. Mayer, M. Samoc and R. A. Fischer, *Chem. Soc. Rev.*, **2017**, *46*, 4976-5004.

44. G. Minguez Espallargas and E. Coronado, *Chem. Soc. Rev.*, **2018**, *47*, 533-557.

45. H. N. Miras, L. Vila-Nadal and L. Cronin, *Chem. Soc. Rev.*, **2014**, *43*, 5679-5699.

46. R. E. Morris and L. Brammer, *Chem. Soc. Rev.*, **2017**, *46*, 5444-5462.

47. L. J. Murray, M. Dinca and J. R. Long, *Chem. Soc. Rev.*, **2009**, *38*, 1294-1314.

48. M. O'Keeffe, *Chem. Soc. Rev.*, **2009**, *38*, 1215-1217.

49. J. J. Perry Iv, J. A. Perman and M. J. Zaworotko, *Chem. Soc. Rev.*, **2009**, *38*, 1400-1417.

50. S. Qiu, M. Xue and G. Zhu, *Chem. Soc. Rev.*, **2014**, *43*, 6116-6140.

51. P. Ramaswamy, N. E. Wong and G. K. H. Shimizu, *Chem. Soc. Rev.*, **2014**, *43*, 5913-5932.

52. S. M. J. Rogge, A. Bavykina, J. Hajek, H. Garcia, A. I. Olivos-Suarez, A. Sepulveda-Escribano, A. Vimont, G. Clet, P. Bazin, F. Kapteijn, M. Daturi, E. V. Ramos-Fernandez, F. X. Llabres i Xamena, V. Van Speybroeck and J. Gascon, *Chem. Soc. Rev.*, **2017**, *46*, 3134-3184.

53. M. Rubio-Martinez, C. Avci-Camur, A. W. Thornton, I. Imaz, D. Maspoch and M. R. Hill, *Chem. Soc. Rev.*, **2017**, *46*, 3453-3480.

54. A. Schneemann, V. Bon, I. Schwedler, I. Senkovska, S. Kaskel and R. A. Fischer, *Chem. Soc. Rev.*, **2014**, *43*, 6062-6096.

55. G. K. H. Shimizu, R. Vaidhyanathan and J. M. Taylor, *Chem. Soc. Rev.*, **2009**, *38*, 1430-1449.

56. A. M. Spokoyny, D. Kim, A. Sumrein and C. A. Mirkin, *Chem. Soc. Rev.*, **2009**, *38*, 1218-1227.

57. I. Stassen, N. Burtch, A. Talin, P. Falcaro, M. Allendorf and R. Ameloot, *Chem. Soc. Rev.*, **2017**, *46*, 3185-3241.

58. V. Stavila, A. A. Talin and M. D. Allendorf, *Chem. Soc. Rev.*, **2014**, *43*, 5994-6010.

59. L. Tan and B. Tan, *Chem. Soc. Rev.*, **2017**, *46*, 3322-3356.

60. D. J. Tranchemontagne, J. L. Mendoza-Cortes, M. O'Keeffe and O. M. Yaghi, *Chem. Soc. Rev.*, **2009**, *38*, 1257-1283.

61. T. Uemura, N. Yanai and S. Kitagawa, *Chem. Soc. Rev.*, **2009**, *38*, 1228-1236.

62. B. Van de Voorde, B. Bueken, J. Denayer and D. De Vos, *Chem. Soc. Rev.*, **2014**, *43*, 5766-5788.

63. Z. Wang and S. M. Cohen, *Chem. Soc. Rev.*, **2009**, *38*, 1315-1329.

64. D. Zacher, O. Shekhah, C. Woll and R. A. Fischer, *Chem. Soc. Rev.*, **2009**, *38*, 1418-1429.

65. J.-P. Zhang, P.-Q. Liao, H.-L. Zhou, R.-B. Lin and X.-M. Chen, *Chem. Soc. Rev.*, **2014**, *43*, 5789-5814.

66. T. Zhang and W. Lin, *Chem. Soc. Rev.*, **2014**, *43*, 5982-5993.

67. Z. Zhang and M. J. Zaworotko, *Chem. Soc. Rev.*, **2014**, *43*, 5444-5455.

68. Q.-L. Zhu and Q. Xu, *Chem. Soc. Rev.*, **2014**, *43*, 5468-5512.

69. R. G. Pearson, *J. Am. Chem. Soc.*, **1963**, *85*, 3533-3539.

70. C. Serre, F. Millange, C. Thouvenot, M. Noguès, G. Marsolier, D. Louër and G. Férey, *J. Am. Chem. Soc.*, **2002**, *124*, 13519-13526.

71. G. Férey, C. Serre, C. Mellot-Draznieks, F. Millange, S. Surblé, J. Dutour and I. Margiolaki, *Angew. Chem. Int. Ed.*, **2004**, *43*, 6296-6301.

72. G. Férey, C. Mellot-Draznieks, C. Serre, F. Millange, J. Dutour, S. Surblé and I. Margiolaki, *Science*, **2005**, *309*, 2040.

73. J. H. Cavka, S. Jakobsen, U. Olsbye, N. Guillou, C. Lamberti, S. Bordiga and K. P. Lillerud, *J. Am. Chem. Soc.*, **2008**, *130*, 13850-13851.

74. D. Feng, Z.-Y. Gu, J.-R. Li, H.-L. Jiang, Z. Wei and H.-C. Zhou, *Angew. Chem. Int. Ed.*, **2012**, *51*, 10307-10310.

75. D. Feng, W.-C. Chung, Z. Wei, Z.-Y. Gu, H.-L. Jiang, Y.-P. Chen, D. J. Darensbourg and H.-C. Zhou, *J. Am. Chem. Soc.*, **2013**, *135*, 17105-17110.

76. D. Feng, H.-L. Jiang, Y.-P. Chen, Z.-Y. Gu, Z. Wei and H.-C. Zhou, *Inorg. Chem.*, **2013**, *52*, 12661-12667.

77. H.-L. Jiang, D. Feng, K. Wang, Z.-Y. Gu, Z. Wei, Y.-P. Chen and H.-C. Zhou, *J. Am. Chem. Soc.*, **2013**, *135*, 13934-13938.

78. D. Feng, Z.-Y. Gu, Y.-P. Chen, J. Park, Z. Wei, Y. Sun, M. Bosch, S. Yuan and H.-C. Zhou, *J. Am. Chem. Soc.*, **2014**, *136*, 17714-17717.

79. *The cell: a molecular approach*, Sunderland (MA): Sinauer Associates, 2nd edn., 2000.

80. A. Schmid, J. S. Dordick, B. Hauer, A. Kiener, M. Wubbolts and B. Witholt, *Nature*, **2001**, *409*, 258-268.

81. Z. Zhou and M. Hartmann, *Top. Catal.*, **2012**, *55*, 1081-1100.

82. Z. Zhou and M. Hartmann, *Chem. Soc. Rev.*, **2013**, *42*, 3894-3912.

83. C.-P. Xu and J. W. Yun, *Enzyme Microb. Technol.*, **2004**, *35*, 33-39.

84. T. Tosa, T. Mori, N. Fuse and I. Chibata, *Enzymologia*, **1966**, *31*, 214-224.

85. K. Hernandez and R. Fernandez-Lafuente, *Enzyme Microb. Technol.*, **2011**, *48*, 107-122.

86. R. A. Sheldon, *Biochem. Soc. Trans.*, **2007**, *35*, 1583-1587.

87. P. Asuri, S. S. Karajanagi, E. Sellitto, D.-Y. Kim, R. S. Kane and J. S. Dordick, *Biotechnol. Bioeng.*, **2006**, *95*, 804-811.

88. N. Saifuddin, A. Z. Raziah and A. R. Junizah, *Journal of Chemistry*, **2013**, *2013*, 18.

89. *Enzymes in Industry: Production and Applications*, Wiley-VCH, 3rd edn., 2007.

90. T. Xie, A. Wang, L. Huang, H. Li, Z. Chen, Q. Wang and X. Yin, *African Journal of Biotechnology*, **2009**, *8*, 4724-4733.

91. N. R. Mohamad, N. H. C. Marzuki, N. A. Buang, F. Huyop and R. A. Wahab, *Biotechnology & Biotechnological Equipment*, **2015**, *29*, 205-220.

92. V. L. Sirisha, A. Jain and A. Jain, in *Adv. Food Nutr. Res.*, eds. S.-K. Kim and F. Toldrá, Academic Press, 2016, vol. 79, pp. 179-211.

93. A. J. H. Al-Adhami, J. Bryjak, B. Greb-Markiewicz and W. Peczyńska-Czoch, *Process Biochem.*, **2002**, *37*, 1387-1394.

94. S. Cynthia and D. M. Shelley, *Recent Patents on Engineering*, **2008**, *2*, 195-200.

95. M. Persson, E. Wehtje and P. Adlercreutz, *Biotechnol. Lett.*, **2000**, *22*, 1571-1575.

96. A. G. Cunha, G. Fernández-Lorente, J. V. Bevilaqua, J. Destain, L. M. C. Paiva, D. M. G. Freire, R. Fernández-Lafuente and J. M. Guisán, *Appl. Biochem. Biotechnol.*, **2008**, *146*, 49-56.

97. R. Y. Cabrera-Padilla, M. C. Lisboa, A. T. Fricks, E. Franceschi, A. S. Lima, D. P. Silva and C. M. F. Soares, *J. Ind. Microbiol. Biotechnol.*, **2012**, *39*, 289-298.

98. N. Mishra, K. Pithawala and A. Bahadur, *Appl. Biochem. Biotechnol.*, **2011**, *165*, 1568-1576.

99. J. Fu, J. Reinhold and N. W. Woodbury, *PLoS One*, **2011**, *6*, e18692.

100. R. E. Ducker, M. T. Montague and G. J. Leggett, *Biointerphases*, **2008**, *3*, 59-65.

101. D. H. Lee, C. H. Park, J. M. Yeo and S. W. Kim, *Journal of Industrial and Engineering Chemistry*, **2006**, *12*, 777-782.

102. L. Huang and Z.-M. Cheng, *Chem. Eng. J.*, **2008**, *144*, 103-109.

103. Q. Zhao, Y. Hou, G.-H. Gong, M.-A. Yu, L. Jiang and F. Liao, *Appl. Biochem. Biotechnol.*, **2010**, *160*, 2287-2299.

104. B. D. Singh, *Biotechnology: Expanding Horizons*, Kalyani Publishers, 2012.

105. Q. Shen, R. Yang, X. Hua, F. Ye, W. Zhang and W. Zhao, *Process Biochem.*, **2011**, *46*, 1565-1571.

106. G.-C. Chen, I. C. Kuan, J.-R. Hong, B.-H. Tsai, S.-L. Lee and C.-Y. Yu, *Biotechnol. Lett.*, **2011**, *33*, 525-529.

107. K. R. Jegannathan, L. Jun-Yee, E.-S. Chan and P. Ravindra, *Fuel*, **2010**, *89*, 2272-2277.

108. D. Dai and L. Xia, *Appl. Biochem. Biotechnol.*, **2006**, *134*, 39-50.

109. L. Cao, in *Carrier-bound Immobilized Enzymes*, Wiley-VCH Verlag GmbH & Co. KGaA, 2006, DOI: 10.1002/3527607668.ch1, pp. 1-52.

110. M. Hartmann and X. Kostrov, *Chem. Soc. Rev.*, **2013**, *42*, 6277-6289.

111. N. Burteau, S. Burton and R. R. Crichton, *FEBS Lett.*, **1989**, *258*, 185-189.

112. M. Dezott, L. H. Innocentini-Mei and N. Durán, *J. Biotechnol.*, **1995**, *43*, 161-167.

113. E. Magnan, I. Catarino, D. Paolucci-Jeanjean, L. Preziosi-Belloy and M. P. Belleville, *J. Membr. Sci.*, **2004**, *241*, 161-166.

114. R. Sahney, B. K. Puri and S. Anand, *Anal. Chim. Acta*, **2005**, *542*, 157-161.

115. A. S. Rani, M. L. M. Das and S. Satyanarayana, *J. Mol. Catal. B: Enzym.*, **2000**, *10*, 471-476.

116. A. Ganesh Kumar, K. Perinbam, P. Kamatchi, N. Nagesh and G. Sekaran, *Bioresour. Technol.*, **2010**, *101*, 1377-1379.

117. Y. M. Elçin, *Biomaterials*, **1995**, *16*, 1157-1161.

118. S. S. Betigeri and S. H. Neau, *Biomaterials*, **2002**, *23*, 3627-3636.

119. M. P. Klein, C. W. Scheeren, A. S. G. Lorenzoni, J. Dupont, J. Frazzon and P. F. Hertz, *Process Biochem.*, **2011**, *46*, 1375-1379.

120. S. Chen, N. Song, X. Liao and B. Shi, *Chin. J. Biotechnol.*, **2011**, *27*, 1076-1081.

121. H.-c. Tsai and R.-a. Doong, *Biosensors Bioelectron.*, **2005**, *20*, 1796-1804.

122. R.-A. Doong and H.-C. Tsai, *Anal. Chim. Acta*, **2001**, *434*, 239-246.

123. H. Mohammadi, M. El Rhazi, A. Amine, A. M. O. Brett and C. M. A. Brett, *Analyst*, **2002**, *127*, 1088-1093.

124. G.-M. Zeng, L. Tang, G.-L. Shen, G.-H. Huang and C.-G. Niu, *Int. J. Environ. Anal. Chem.*, **2004**, *84*, 761-774.

125. M. El Kaoutit, D. Bouchta, H. Zejli, N. Izaoumen and K. R. Temsamani, *Anal. Lett.*, **2004**, *37*, 1671-1681.

126. S. Akhtar, A. A. Khan and Q. Husain, *Bioresour. Technol.*, **2005**, *96*, 1804-1811.

127. X. Wu, N. Chou, D. Lupher and L. C. Davis, *Proceedings of the 1998 Conference on Hazardous Waste Research*, **1998**, 374-382.

128. R. DiCosimo, J. McAuliffe, A. J. Poulose and G. Bohlmann, *Chem. Soc. Rev.*, **2013**, *42*, 6437-6474.

129. X. Lian, Y. Fang, E. Joseph, Q. Wang, J. Li, S. Banerjee, C. Lollar, X. Wang and H.-C. Zhou, *Chem. Soc. Rev.*, **2017**, *46*, 3386-3401.

130. Y.-H. Shih, S.-H. Lo, N.-S. Yang, B. Singco, Y.-J. Cheng, C.-Y. Wu, I. H. Chang, H.-Y. Huang and C.-H. Lin, *ChemPlusChem*, **2012**, *77*, 982-986.

131. Y. Cao, Z. Wu, T. Wang, Y. Xiao, Q. Huo and Y. Liu, *Dalton Transactions*, **2016**, *45*, 6998-7003.

132. V. Lykourinou, Y. Chen, X.-S. Wang, L. Meng, T. Hoang, L.-J. Ming, R. L. Musselman and S. Ma, *J. Am. Chem. Soc.*, **2011**, *133*, 10382-10385.

133. Y. Chen, V. Lykourinou, T. Hoang, L.-J. Ming and S. Ma, *Inorg. Chem.*, **2012**, *51*, 9156-9158.

134. D. Feng, T.-F. Liu, J. Su, M. Bosch, Z. Wei, W. Wan, D. Yuan, Y.-P. Chen, X. Wang, K. Wang, X. Lian, Z.-Y. Gu, J. Park, X. Zou and H.-C. Zhou, *Nat. Commun.*, **2015**, *6*, 5979.

135. W.-L. Liu, S.-H. Lo, B. Singco, C.-C. Yang, H.-Y. Huang and C.-H. Lin, *J. Mater. Chem. B*, **2013**, *1*, 928-932.

136. W.-L. Liu, N.-S. Yang, Y.-T. Chen, S. Lirio, C.-Y. Wu, C.-H. Lin and H.-Y. Huang, *Chem. Eur. J.*, **2015**, *21*, 115-119.

137. P. Li, S.-Y. Moon, M. A. Guelta, S. P. Harvey, J. T. Hupp and O. K. Farha, *J. Am. Chem. Soc.*, **2016**, *138*, 8052-8055.

138. K. Liang, R. Ricco, C. M. Doherty, M. J. Styles, S. Bell, N. Kirby, S. Mudie, D. Haylock, A. J. Hill, C. J. Doonan and P. Falcaro, *Nat. Commun.*, **2015**, *6*, 7240.

139. H. He, H. Han, H. Shi, Y. Tian, F. Sun, Y. Song, Q. Li and G. Zhu, *ACS Appl. Mater. Interfaces*, **2016**, *8*, 24517-24524.

140. X. Wu, J. Ge, C. Yang, M. Hou and Z. Liu, *Chem. Commun.*, **2015**, *51*, 13408-13411.

141. X. Lian, Y.-P. Chen, T.-F. Liu and H.-C. Zhou, *Chem. Sci.*, **2016**, *7*, 6969-6973.

142. I. Gill and A. Ballesteros, *J. Am. Chem. Soc.*, **1998**, *120*, 8587-8598.

143. E. S. Lee, M. J. Kwon, H. Lee and J. J. Kim, *Int. J. Pharm.*, **2007**, *331*, 27-37.

144. K. Y. Lee and S. H. Yuk, *Prog. Polym. Sci.*, **2007**, *32*, 669-697.

145. R. A. Sheldon, *Adv. Synth. Catal.*, **2007**, *349*, 1289-1307.

146. S. Hudson, J. Cooney and E. Magner, *Angew. Chem. Int. Ed.*, **2008**, *47*, 8582-8594.

147. M. Hartmann and D. Jung, *J. Mater. Chem.*, **2010**, *20*, 844-857.

148. D. I. Fried, F. J. Brieler and M. Fröba, *ChemCatChem*, **2013**, *5*, 862-884.

149. G. Jadot, A. Vaille, J. Maldonado and P. Vanelle, *Clin. Pharmacokinet.*, **1995**, *28*, 17-25.

150. C. P. Leamon and P. S. Low, *Proceedings of the National Academy of Sciences*, **1991**, *88*, 5572.

151. Y. Huang, R. Zhao, Y. Fu, Q. Zhang, S. Xiong, L. Li, R. Zhou, G. Liu and Y. Chen, *ChemBioChem*, **2011**, *12*, 1209-1215.

152. Y. K. Park, S. B. Choi, H. Kim, K. Kim, B.-H. Won, K. Choi, J.-S. Choi, W.-S. Ahn, N. Won, S. Kim, D. H. Jung, S.-H. Choi, G.-H. Kim, S.-S. Cha, Y. H. Jhon, J. K. Yang and J. Kim, *Angew. Chem.*, **2007**, *119*, 8378-8381.

153. H.-C. Zhou, J. R. Long and O. M. Yaghi, *Chem. Rev.*, **2012**, *112*, 673-674.

154. H. Deng, S. Grunder, K. E. Cordova, C. Valente, H. Furukawa, M. Hmadeh, F. Gándara, A. C. Whalley, Z. Liu, S. Asahina, H. Kazumori, M. O'Keeffe, O. Terasaki, J. F. Stoddart and O. M. Yaghi, *Science*, **2012**, *336*, 1018.

155. J. W. Yoon, Y.-K. Seo, Y. K. Hwang, J.-S. Chang, H. Leclerc, S. Wuttke, P. Bazin, A. Vimont, M. Daturi, E. Bloch, P. L. Llewellyn, C. Serre, P. Horcajada, J.-M. Grenèche, A. E. Rodrigues and G. Férey, *Angew. Chem. Int. Ed.*, **2010**, *49*, 5949-5952.

156. A. F. Cozzolino, C. K. Brozek, R. D. Palmer, J. Yano, M. Li and M. Dincă, *J. Am. Chem. Soc.*, **2014**, *136*, 3334-3337.

157. M. J. Katz, Z. J. Brown, Y. J. Colon, P. W. Siu, K. A. Scheidt, R. Q. Snurr, J. T. Hupp and O. K. Farha, *Chem. Commun.*, **2013**, *49*, 9449-9451.

158. C. Volkringer, D. Popov, T. Loiseau, G. Férey, M. Burghammer, C. Riekel, M. Haouas and F. Taulelle, *Chem. Mater.*, **2009**, *21*, 5695-5697.

159. M. Dan-Hardi, C. Serre, T. Frot, L. Rozes, G. Maurin, C. Sanchez and G. Férey, *J. Am. Chem. Soc.*, **2009**, *131*, 10857-10859.

160. P. Deria, J. E. Mondloch, E. Tylianakis, P. Ghosh, W. Bury, R. Q. Snurr, J. T. Hupp and O. K. Farha, *J. Am. Chem. Soc.*, **2013**, *135*, 16801-16804.

161. H. Furukawa, F. Gándara, Y.-B. Zhang, J. Jiang, W. L. Queen, M. R. Hudson and O. M. Yaghi, *J. Am. Chem. Soc.*, **2014**, *136*, 4369-4381.

162. M. Kim, J. F. Cahill, H. Fei, K. A. Prather and S. M. Cohen, *J. Am. Chem. Soc.*, **2012**, *134*, 18082-18088.

163. D. Feng, K. Wang, Z. Wei, Y.-P. Chen, C. M. Simon, R. K. Arvapally, R. L. Martin, M. Bosch, T.-F. Liu, S. Fordham, D. Yuan, M. A. Omary, M. Haranczyk, B. Smit and H.-C. Zhou, *Nat. Commun.*, **2014**, *5*, 5723.

164. I. J. Kang, N. A. Khan, E. Haque and S. H. Jhung, *Chem. Eur. J.*, **2011**, *17*, 6437-6442.

165. T.-F. Liu, L. Zou, D. Feng, Y.-P. Chen, S. Fordham, X. Wang, Y. Liu and H.-C. Zhou, *J. Am. Chem. Soc.*, **2014**, *136*, 7813-7816.

166. Y.-F. Niu, W. Zhao, J. Han, GeTian and X.-L. Zhao, *CrystEngComm*, **2014**, *16*, 2344-2347.

167. H. Fei, J. F. Cahill, K. A. Prather and S. M. Cohen, *Inorg. Chem.*, **2013**, *52*, 4011-4016.

168. S. Das, H. Kim and K. Kim, *J. Am. Chem. Soc.*, **2009**, *131*, 3814-3815.

169. J. Park, Y.-P. Chen, Z. Perry, J.-R. Li and H.-C. Zhou, *J. Am. Chem. Soc.*, **2014**, *136*, 16895-16901.

170. Z. Zhang, L. Wojtas, M. Eddaoudi and M. J. Zaworotko, *J. Am. Chem. Soc.*, **2013**, *135*, 5982-5985.

171. Z. Zhang, L. Zhang, L. Wojtas, P. Nugent, M. Eddaoudi and M. J. Zaworotko, *J. Am. Chem. Soc.*, **2012**, *134*, 924-927.

172. P. Atkins, *Shriver and Atkins' Inorganic Chemistry*, OUP Oxford, 2010.

173. R. B. Jordan, *Reaction Mechanisms of Inorganic and Organometallic Systems*, Oxford University Press, 2007.

174. M. C. M. van Oers, F. Rutjes and J. C. M. van Hest, *Curr. Opin. Biotechnol.*, **2014**, *28*, 10-16.

175. S. P. Colowick, N. O. Kaplan and J. M. Lowenstein, *Methods in Enzymology: Citric acid cycle / edited by John M. Lowenstein*, Academic Press, 1969.

176. J. Kay, B. S. Symposium and P. D. J. Weitzman, *Krebs' Citric Acid Cycle: Half a Century and Still Turning : [symposium]*, Biochemical Society, 1987.

177. M. Marguet, C. Bonduelle and S. Lecommandoux, *Chem. Soc. Rev.*, **2013**, *42*, 512-529.

178. X. Cao, Y. Li, Z. Zhang, J. Yu, J. Qian and S. Liu, *Analyst*, **2012**, *137*, 5785-5791.

179. D. M. Vriezema, P. M. L. Garcia, N. Sancho Oltra, N. S. Hatzakis, S. M. Kuiper, R. J. M. Nolte, A. E. Rowan and J. C. M. van Hest, *Angew. Chem. Int. Ed.*, **2007**, *46*, 7378-7382.

180. S. F. M. van Dongen, M. Nallani, J. J. L. M. Cornelissen, R. J. M. Nolte and J. C. M. van Hest, *Chem. Eur. J.*, **2009**, *15*, 1107-1114.

181. D. Avnir, T. Coradin, O. Lev and J. Livage, *J. Mater. Chem.*, **2006**, *16*, 1013-1030.

182. D. E. Discher and A. Eisenberg, *Science*, **2002**, *297*, 967.

183. K. Hirai, J. Reboul, N. Morone, J. E. Heuser, S. Furukawa and S. Kitagawa, *J. Am. Chem. Soc.*, **2014**, *136*, 14966-14973.

184. K. Lu, C. He and W. Lin, *J. Am. Chem. Soc.*, **2014**, *136*, 16712-16715.

185. W. Xuan, C. Zhu, Y. Liu and Y. Cui, *Chem. Soc. Rev.*, **2012**, *41*, 1677-1695.

186. X.-S. Wang, M. Chrzanowski, D. Yuan, B. S. Sweeting and S. Ma, *Chem. Mater.*, **2014**, *26*, 1639-1644.

187. Y. Ke, D. J. Collins, D. Sun and H.-C. Zhou, *Inorg. Chem.*, **2006**, *45*, 1897-1899.

188. Y. Chen, V. Lykourinou, C. Vetromile, T. Hoang, L.-J. Ming, R. W. Larsen and S. Ma, *J. Am. Chem. Soc.*, **2012**, *134*, 13188-13191.

189. F.-K. Shieh, S.-C. Wang, C.-I. Yen, C.-C. Wu, S. Dutta, L.-Y. Chou, J. V. Morabito, P. Hu, M.-H. Hsu, K. C. W. Wu and C.-K. Tsung, *J. Am. Chem. Soc.*, **2015**, *137*, 4276-4279.

190. G. Lu, S. Li, Z. Guo, O. K. Farha, B. G. Hauser, X. Qi, Y. Wang, X. Wang, S. Han, X. Liu, J. S. DuChene, H. Zhang, Q. Zhang, X. Chen, J. Ma, S. C. J. Loo, W. D. Wei, Y. Yang, J. T. Hupp and F. Huo, *Nat. Chem.*, **2012**, *4*, 310.

191. J.-R. Li, J. Yu, W. Lu, L.-B. Sun, J. Sculley, P. B. Balbuena and H.-C. Zhou, *Nat. Commun.*, **2013**, *4*, 1538.

192. P. Horcajada, T. Chalati, C. Serre, B. Gillet, C. Sebrie, T. Baati, J. F. Eubank, D. Heurtaux, P. Clayette, C. Kreuz, J.-S. Chang, Y. K. Hwang, V. Marsaud, P.-N. Bories, L. Cynober, S. Gil, G. Férey, P. Couvreur and R. Gref, *Nat. Mater.*, **2009**, *9*, 172.

193. P. K. Smith, R. I. Krohn, G. T. Hermanson, A. K. Mallia, F. H. Gartner, M. D. Provenzano, E. K. Fujimoto, N. M. Goeke, B. J. Olson and D. C. Klenk, *Anal. Biochem.*, **1985**, *150*, 76-85.

194. W.-L. Liu, C.-Y. Wu, C.-Y. Chen, B. Singco, C.-H. Lin and H.-Y. Huang, *Chem. Eur. J.*, **2014**, *20*, 8923-8928.

195. Y. Chen, S. Han, X. Li, Z. Zhang and S. Ma, *Inorg. Chem.*, **2014**, *53*, 10006-10008.

196. Diego S. D'Astolfo, Romina J. Pagliero, A. Pras, Wouter R. Karthaus, H. Clevers, V. Prasad, Robert J. Lebbink, H. Rehmann and N. Geijsen, *Cell*, **2015**, *161*, 674-690.

197. R. J. Desnick and E. H. Schuchman, *Nat. Rev. Genet.*, **2002**, *3*, 954-966.

198. S. O. Freytag, H. Stricker, J. Pegg, D. Paielli, D. G. Pradhan, J. Peabody, M. DePeralta-Venturina, X. Xia, S. Brown and M. Lu, *Cancer Res.*, **2003**, *63*, 7497-7506.

199. M. Lundberg and M. Johansson, *Nat Biotech*, **2001**, *19*, 713-713.

200. M. Cavazzana-Calvo, A. Thrasher and F. Mavilio, *Nature*, **2004**, *427*, 779-781.

201. C. E. Thomas, A. Ehrhardt and M. A. Kay, *Nat. Rev. Genet.*, **2003**, *4*, 346-358.

202. S. Hacein-Bey-Abina, C. Von Kalle, M. Schmidt, M. McCormack, N. Wulffraat, P. a. Leboulch, A. Lim, C. Osborne, R. Pawliuk and E. Morillon, *Science*, **2003**, *302*, 415-419.

203. D. Otzen, *Biochim. Biophys. Acta*, **2011**, *1814*, 562-591.

204. S. Jevševar, M. Kunstelj and V. G. Porekar, *Biotechnol. J.*, **2010**, *5*, 113-128.

205. P. Tanner, O. Onaca, V. Balasubramanian, W. Meier and C. G. Palivan, *Chem. Eur. J.*, **2011**, *17*, 4552-4560.

206. D. A. Christian, S. Cai, D. M. Bowen, Y. Kim, J. D. Pajerowski and D. E. Discher, *Eur. J. Pharm. Biopharm.*, **2009**, *71*, 463-474.

207. L. Sercombe, T. Veerati, F. Moheimani, S. Y. Wu, A. K. Sood and S. Hua, *Front. Pharmacol.*, **2015**, *6*, 286.

208. M. L. Immordino, F. Dosio and L. Cattel, *Int. J. Nanomedicine*, **2006**, *1*, 297-315.

209. Y.-P. Chen, C.-T. Chen, Y. Hung, C.-M. Chou, T.-P. Liu, M.-R. Liang, C.-T. Chen and C.-Y. Mou, *J. Am. Chem. Soc.*, **2013**, *135*, 1516-1523.

210. D. E. Discher, V. Ortiz, G. Srinivas, M. L. Klein, Y. Kim, D. Christian, S. Cai, P. Photos and F. Ahmed, *Prog. Polym. Sci.*, **2007**, *32*, 838-857.

211. R. A. Schwendener, *Ther. Adv. Vaccines*, **2014**, *2*, 159-182.

212. S. R. Schwarze, K. A. Hruska and S. F. Dowdy, *Trends Cell Biol.*, **2000**, *10*, 290-295.

213. D. Peer, J. M. Karp, S. Hong, O. C. Farokhzad, R. Margalit and R. Langer, *Nat. Nanotechnol.*, **2007**, *2*, 751-760.

214. R. Langer and D. A. Tirrell, *Nature*, **2004**, *428*, 487-492.

215. R. Gref, Y. Minamitake, M. Peracchia, V. Trubetskoy, V. Torchilin and R. Langer, *Science*, **1994**, *263*, 1600-1603.

216. C. S. Fishburn, *J. Pharm. Sci.*, **2008**, *97*, 4167-4183.

217. D. S. Pisal, M. P. Kosloski and S. V. Balu-Iyer, *J. Pharm. Sci.*, **2010**, *99*, 2557-2575.

218. H.-C. Zhou and S. Kitagawa, *Chem. Soc. Rev.*, **2014**, 5415-5418.

219. P. Horcajada, R. Gref, T. Baati, P. K. Allan, G. Maurin, P. Couvreur, G. Férey, R. E. Morris and C. Serre, *Chem. Rev.*, **2012**, *112*, 1232-1268.

220. L. E. Kreno, K. Leong, O. K. Farha, M. Allendorf, R. P. Van Duyne and J. T. Hupp, *Chem. Rev.*, **2012**, *112*, 1105-1125.

221. K. Sumida, D. L. Rogow, J. A. Mason, T. M. McDonald, E. D. Bloch, Z. R. Herm, T.-H. Bae and J. R. Long, *Chem. Rev.*, **2012**, *112*, 724-781.

222. F. Lyu, Y. Zhang, R. N. Zare, J. Ge and Z. Liu, *Nano Lett.*, **2014**, *14*, 5761-5765.

223. T. Hidalgo, L. Cooper, M. Gorman, T. Lozano-Fernandez, R. Simon-Vazquez, G. Mouchaham, J. Marrot, N. Guillou, C. Serre, P. Fertey, A. Gonzalez-Fernandez, T. Devic and P. Horcajada, *J. Mater. Chem. B*, **2017**, *5*, 2813-2822.

224. S.-L. Cao, D.-M. Yue, X.-H. Li, T. J. Smith, N. Li, M.-H. Zong, H. Wu, Y.-Z. Ma and W.-Y. Lou, *ACS Sustain. Chem. Eng.*, **2016**, *4*, 3586-3595.

225. H. He, H. Han, H. Shi, Y. Tian, F. Sun, Y. Song, Q. Li and G. Zhu, *ACS Appl. Mater. Interfaces*, **2016**, *8*, 24517-24524.

226. X. Wu, J. Ge, C. Yang, M. Hou and Z. Liu, *Chem. Commun.*, **2015**, *51*, 13408-13411.

227. T. Kundu, S. Mitra, P. Patra, A. Goswami, D. Díaz Díaz and R. Banerjee, *Chem. Eur. J.*, **2014**, *20*, 10514-10518.

228. Q. Hu, J. Yu, M. Liu, A. Liu, Z. Dou and Y. Yang, *J. Med. Chem.*, **2014**, *57*, 5679-5685.

229. L. Cooper, T. Hidalgo, M. Gorman, T. Lozano-Fernandez, R. Simon-Vazquez, C. Olivier, N. Guillou, C. Serre, C. Martineau, F. Taulelle, D. Damasceno-Borges, G. Maurin, A. Gonzalez-Fernandez, P. Horcajada and T. Devic, *Chem. Commun.*, **2015**, *51*, 5848-5851.

230. E. Gkaniatsou, C. Sicard, R. Ricoux, J.-P. Mahy, N. Steunou and C. Serre, *Mater. Horiz.*, **2017**, *4*, 55-63.

231. H. Su, F. Sun, J. Jia, H. He, A. Wang and G. Zhu, *Chem. Commun.*, **2015**, *51*, 5774-5777.

232. X. Zhu, J. Gu, Y. Wang, B. Li, Y. Li, W. Zhao and J. Shi, *Chem. Commun.*, **2014**, *50*, 8779-8782.

233. T. Baati, L. Njim, F. Neffati, A. Kerkeni, M. Bouttemi, R. Gref, M. F. Najjar, A. Zakhama, P. Couvreur, C. Serre and P. Horcajada, *Chem. Sci.*, **2013**, *4*, 1597-1607.

234. I. B. Vasconcelos, T. G. d. Silva, G. C. G. Militao, T. A. Soares, N. M. Rodrigues, M. O. Rodrigues, N. B. d. Costa, R. O. Freire and S. A. Junior, *RSC Adv.*, **2012**, *2*, 9437-9442.

235. À. Ruyra, A. Yazdi, J. Espín, A. Carné-Sánchez, N. Roher, J. Lorenzo, I. Imaz and D. Maspoch, *Chem. Eur. J.*, **2015**, *21*, 2508-2518.

236. F. R. S. Lucena, L. C. C. de Araújo, M. d. D. Rodrigues, T. G. da Silva, V. R. A. Pereira, G. C. G. Militão, D. A. F. Fontes, P. J. Rolim-Neto, F. F. da Silva and S. C. Nascimento, *Biomed. Pharmacother.*, **2013**, *67*, 707-713.

237. M. Schieber and Navdeep S. Chandel, *Curr. Biol.*, **2014**, *24*, R453-R462.

238. B. Uttara, A. V. Singh, P. Zamboni and R. T. Mahajan, *Curr. Neuropharmacol.*, **2009**, *7*, 65-74.

239. A. M. Pisoschi and A. Pop, *Eur. J. Med. Chem.*, **2015**, *97*, 55-74.

240. A. A. Adly, *Res. J. Immunol.*, **2010**, *3*, 129-145.

241. J. P. Luzio, P. R. Pryor and N. A. Bright, *Nat. Rev. Mol. Cell Biol.*, **2007**, *8*, 622-632.

242. D. Feng, K. Wang, Z. Wei, Y. P. Chen, C. M. Simon, R. K. Arvapally, R. L. Martin, M. Bosch, T. F. Liu, S. Fordham, D. Yuan, M. A. Omary, M. Haranczyk, B. Smit and H. C. Zhou, *Nat Commun*, **2014**, *5*, 5723.

243. K. Najjar, A. Erazo-Oliveras, D. J. Brock, T.-Y. Wang and J.-P. Pellois, *J. Biol. Chem.*, **2016**, DOI: 10.1074/jbc.M116.759837.

244. M.-S. Byun, K.-I. Jeon, J.-W. Choi, J.-Y. Shim and D.-M. Jue, *Exp. Mol. Med.*, **2002**, *34*, 332-339.

245. B. V. Chernyak, D. S. Izyumov, K. G. Lyamzaev, A. A. Pashkovskaya, O. Y. Pletjushkina, Y. N. Antonenko, D. V. Sakharov, K. W. A. Wirtz and V. P. Skulachev, *Biochim. Biophys. Acta*, **2006**, *1757*, 525-534.

246. P. Pallepati and D. A. Averill-Bates, *Biochim. Biophys. Acta*, **2011**, *1813*, 1987-1999.

247. M. A. Hough and S. S. Hasnain, *J. Mol. Biol.*, **1999**, *287*, 579-592.

248. K. Yonekura and S. Maki-Yonekura, *J. Appl. Crystallogr.*, **2016**, *49*, 1517-1523.

249. M. Schrader and H. D. Fahimi, *Biochim. Biophys. Acta*, **2006**, *1763*, 1755-1766.

250. T. Fukai and M. Ushio-Fukai, *Antioxid. Redox Signal*, **2011**, *15*, 1583-1606.

251. A. Erazo-Oliveras, K. Najjar, D. Truong, T.-Y. Wang, Dakota J. Brock, Austin R. Prater and J.-P. Pellois, *Cell Chem. Biol.*, **2016**, *23*, 598-607.

252. A. Erazo-Oliveras, K. Najjar, L. Dayani, T.-Y. Wang, G. A. Johnson and J.-P. Pellois, *Nat. Methods*, **2014**, *11*, 861-867.

253. P. M. Schmölzer, M. Höftberger and I. Foissner, *Plant Cell Physiol.*, **2011**, *52*, 1274-1288.

254. K. Raghu, V. Mahesh, P. Sasidhar, P. R. Reddy, V. Venkataramaniah and A. Agrawal, *J. Family Community Med.*, **2013**, *20*, 198-200.

255. L. Benov, *Protoplasma*, **2001**, *217*, 33-36.

256. K. Keyer, A. S. Gort and J. A. Imlay, *J. Bacteriol.*, **1995**, *177*, 6782-6790.

257. F. D. Oakley, D. Abbott, Q. Li and J. F. Engelhardt, *Antioxidants & Redox Signaling*, **2008**, *11*, 1313-1333.

258. A. Singhal, V. B. Morris, V. Labhasetwar and A. Ghorpade, *Cell Death Dis.*, **2013**, *4*, e903.

259. J. W. Maina, J. J. Richardson, R. Chandrawati, K. Kempe, M. P. van Koeverden and F. Caruso, *Langmuir*, **2015**, *31*, 7776-7781.

260. B. Y. Chu, M. A. Kobiasi, W. Zeng, D. Mainwaring and D. C. Jackson, *Procedia Vaccinol.*, **2012**, *6*, 74-79.

261. P. Tanner, S. Egli, V. Balasubramanian, O. Onaca, C. G. Palivan and W. Meier, *FEBS Lett.*, **2011**, *585*, 1699-1706.

262. P. Tanner, P. Baumann, R. Enea, O. Onaca, C. Palivan and W. Meier, *Acc. Chem. Res.*, **2011**, *44*, 1039-1049.

263. P. Tanner, V. Balasubramanian and C. G. Palivan, *Nano Lett.*, **2013**, *13*, 2875-2883.

264. M. Garni, T. Einfalt, M. Lomora, A. Car, W. Meier and C. G. Palivan, *CHIMIA International Journal for Chemistry*, **2016**, *70*, 424-427.

265. J. Liu, V. Postupalenko, S. Lörcher, D. Wu, M. Chami, W. Meier and C. G. Palivan, *Nano Lett.*, **2016**, *16*, 7128-7136.

266. P. G. Corrie, *Medicine*, **2008**, *36*, 24-28.

267. P. J. Loehrer and L. H. Einhorn, *Ann. Intern. Med.*, **1984**, *100*, 704-713.

268. N. I. Marupudi, J. E. Han, K. W. Li, V. M. Renard, B. M. Tyler and H. Brem, *Expert Opin. Drug Saf.*, **2007**, *6*, 609-621.

269. N. Milosavljevic, C. Duranton, N. Djerbi, P. H. Puech, P. Gounon, D. Lagadic-Gossmann, M. T. Dimanche-Boitrel, C. Rauch, M. Tauc, L. Counillon and M. Poët, *Cancer Res.*, **2010**, *70*, 7514-7522.

270. C. Holohan, S. Van Schaeybroeck, D. B. Longley and P. G. Johnston, *Nat. Rev. Cancer*, **2013**, *13*, 714-726.

271. F.-S. Liu, *Taiwan. J. Obstet. Gynecol.*, **2009**, *48*, 239-244.

272. K. O. Alfarouk, C.-M. Stock, S. Taylor, M. Walsh, A. K. Muddathir, D. Verduzco, A. H. H. Bashir, O. Y. Mohammed, G. O. Elhassan, S. Harguindey, S. J. Reshkin, M. E. Ibrahim and C. Rauch, *Cancer Cell Int.*, **2015**, *15*, 71.

273. S. Dhar, N. Kolishetti, S. J. Lippard and O. C. Farokhzad, *Proc. Natl. Acad. Sci. USA*, **2011**, *108*, 1850-1855.

274. M. H. Vingerhoeds, H. J. Haisma, M. van Muijen, R. B. J. van de Rijt, D. J. A. Crommelin and G. Storm, *FEBS Lett.*, **1993**, *336*, 485-490.

275. I. Giang, E. L. Boland and G. M. K. Poon, *AAPS J.*, **2014**, *16*, 899-913.

276. W. A. Denny, *Eur. J. Med. Chem.*, **2001**, *36*, 577-595.

277. M. Rooseboom, J. N. Commandeur and N. P. Vermeulen, *Pharmacol. Rev.*, **2004**, *56*, 53-102.

278. K. Y. Choi, M. Swierczewska, S. Lee and X. Chen, *Theranostics*, **2012**, *2*, 156-178.

279. B. Turk, *Nat. Rev. Drug Discov.*, **2006**, *5*, 785-799.

280. M. H. Vingerhoeds, H. J. Haisma, M. van Muijen, R. B. J. van de Rijt, D. J. A. Crommelin and G. Storm, *FEBS Lett.*, **1993**, *336*, 485-490.

281. R. J. Knox, in *Enzyme-Prodrug Strategies for Cancer Therapy*, eds. R. G. Melton and R. J. Knox, Springer US, Boston, MA, 1999, DOI: 10.1007/978-1-4615-4823-2_4, pp. 97-131.

282. K. D. Bagshawe, S. K. Sharma and R. H. J. Begent, *Expert Opin. Biol. Ther.*, **2004**, *4*, 1777-1789.

283. K. D. Bagshawe, S. K. Sharma, C. J. Springer and G. T. Rogers, *Ann. Oncol.*, **1994**, *5*, 879-891.

284. T. O. Harris, D. W. Shelver, J. F. Bohnsack and C. E. Rubens, *J. Clin. Invest.*, **2003**, *111*, 61-70.

285. D. P. Nolan, S. Rolin, J. R. Rodriguez, J. Van Den Abbeele and E. Pays, *Eur. J. Biochem.*, **2000**, *267*, 18-27.

286. H. He, H. Han, H. Shi, Y. Tian, F. Sun, Y. Song, Q. Li and G. Zhu, *ACS Appl. Mater. Interfaces*, **2016**, *8*, 24517-24524.

287. W. L. Liu, C. Y. Wu, C. Y. Chen, B. Singco, C. H. Lin and H. Y. Huang, *Chem. Eur. J.*, **2014**, *20*, 8923-8928.

288. V. Lykourinou, Y. Chen, X. S. Wang, L. Meng, T. Hoang, L. J. Ming, R. L. Musselman and S. Ma, *J. Am. Chem. Soc.*, **2011**, *133*, 10382-10385.

289. D. Feng, T. F. Liu, J. Su, M. Bosch, Z. Wei, W. Wan, D. Yuan, Y. P. Chen, X. Wang, K. Wang, X. Lian, Z. Y. Gu, J. Park, X. Zou and H. C. Zhou, *Nat. Commun.*, **2015**, *6*, 5979.

290. R. C. Huxford, J. Della Rocca and W. Lin, *Curr. Opin. Chem. Biol.*, **2010**, *14*, 262-268.

291. D. Liu, K. Lu, C. Poon and W. Lin, *Inorg. Chem.*, **2014**, *53*, 1916-1924.

292. J. Della Rocca, D. Liu and W. Lin, *Acc. Chem. Res.*, **2011**, *44*, 957-968.

293. F.-Y. Yi, D. Chen, M.-K. Wu, L. Han and H.-L. Jiang, *ChemPlusChem*, **2016**, *81*, 675-690.

294. L.-L. Tan, H. Li, Y. Zhou, Y. Zhang, X. Feng, B. Wang and Y.-W. Yang, *Small*, **2015**, *11*, 3807-3813.

295. X. Meng, B. Gui, D. Yuan, M. Zeller and C. Wang, *Sci. Adv.*, **2016**, *2*, e1600480.

296. L.-L. Tan, H. Li, Y.-C. Qiu, D.-X. Chen, X. Wang, R.-Y. Pan, Y. Wang, S. X.-A. Zhang, B. Wang and Y.-W. Yang, *Chem. Sci.*, **2015**, *6*, 1640-1644.

297. M.-X. Wu and Y.-W. Yang, *Adv. Mater.*, **2017**, *29*, 1606134-n/a.

298. S.-L. Cao, D.-M. Yue, X.-H. Li, T. J. Smith, N. Li, M.-H. Zong, H. Wu, Y.-Z. Ma and W.-Y. Lou, *ACS Sustain. Chem. Eng.*, **2016**, *4*, 3586-3595.

299. F. K. Shieh, S. C. Wang, C. I. Yen, C. C. Wu, S. Dutta, L. Y. Chou, J. V. Morabito, P. Hu, M. H. Hsu, K. C. Wu and C. K. Tsung, *J. Am. Chem. Soc.*, **2015**, *137*, 4276-4279.

300. X. Lian, A. Erazo-Oliveras, J.-P. Pellois and H.-C. Zhou, *Nat. Commun.*, **2017**, *8*.

301. J. Pawelek, A. Korner, A. Bergstrom and J. Bologna, *Nature*, **1980**, *286*, 617-619.

302. M. J. Hodgman and A. R. Garrard, *Crit. Care Clin.*, **2012**, *28*, 499-516.

303. X. Zhang, J. van Leeuwen, H. J. Wichers and W. H. Flurkey, *J. Agric. Food Chem.*, **1999**, *47*, 374-378.

304. W. Hua, T. Christianson, C. Rougeot, H. Rochefort and G. M. Clinton, *J. Steroid Biochem. Mol. Biol.*, **1995**, *55*, 279-289.

305. X.-D. Yan, M. Li, Y. Yuan, N. Mao and L.-Y. Pan, *Oncol. Rep.*, **2007**, *17*, 1163-1169.

306. H. H. Lee, V. Bellat and B. Law, *PLoS One*, **2017**, *12*, e0171044.

307. A. Pol, R. Luetterforst, M. Lindsay, S. Heino, E. Ikonen and R. G. Parton, *J. Cell Biol.*, **2001**, *152*, 1057-1070.

308. D. E. Kerr, V. M. Vrudhula, H. P. Svensson, N. O. Siemers and P. D. Senter, *Bioconj. Chem.*, **1999**, *10*, 1084-1089.

309. K. S. Raymond, A. K. Grafton and R. A. Wheeler, *J. Phys. Chem. B*, **1997**, *101*, 623-631.

310. C. Guo, W. Wang, W. Feng and P. Li, *RSC Adv.*, **2017**, *7*, 12775-12782.

311. M. Shahidzadeh and M. Ghandi, *J. Organomet. Chem.*, **2001**, *625*, 108-111.

312. P. S. Guin, S. Das and P. C. Mandal, *Int. J. Electrochem.*, **2011**, *2011*, 816202.

313. M. Y. Moridani, R. A. Moore M Fau - Bartsch, Y. Bartsch Ra Fau - Yang, S. Yang Y Fau - Heibati-Sadati and S. Heibati-Sadati, *J. Pharm. Pharm. Sci.*, **2005**, *8*, 348-360.

314. M. Y. Moridani, M. Moore, R. Bartsch, Y. Yang and S. Heibati-Sadati, *Cancer Res.*, **2005**, *65*, 1387-1387.

315. M. A. Baker, G. J. Cerniglia and A. Zaman, *Anal. Biochem.*, **1990**, *190*, 360-365.

316. X. Jiang, J. Chen, A. Bajić, C. Zhang, X. Song, S. L. Carroll, Z.-L. Cai, M. Tang, M. Xue, N. Cheng, C. P. Schaaf, F. Li, K. R. MacKenzie, A. C. M. Ferreon, F. Xia, M. C. Wang, M. Maletić-Savatić and J. Wang, *Nat. Commun.*, **2017**, *8*, 16087.

APPENDIX

This dissertation included published papers shown below:

- **Lian, X.**; Erazo-Oliveras, A.; Pellois, J.-P.; Zhou, H.-C., "High Efficiency and Long-Term Intracellular Activity of an Enzymatic Nanoreactor Based on Metal-Organic Frameworks", *Nat. Commun*., **2017**, *8*: 2075.
- **Lian, X.**; Huang, Y.; Zhu, Y.; Fang, Y.; Zhao, R.; Joseph, E.; Pellois, J.-P.; Zhou, H.-C., "Long-Persistent Enzyme-MOF Nanoreactor Activates Nontoxic Paracetamol for Cancer Therapy", *Angew. Chem. Int. Ed*., **2018**, doi: 10.1002/anie.201801378.
- **Lian, X.**; Fang, Y.; Joseph, E.; Wang, Q.; Li, J.; Banerjee, S.; Lollar, C.; Wang, X.; Zhou, H.-C., "Enzyme-MOF (metal–organic framework) Composites", Chem. *Soc. Rev.*, **2017**, *46*, 3386-3401.
- **Lian, X.**; Chen, Y.-P.; Liu, T.-F.; Zhou, H.-C., "Coupling Two Enzymes into a Tandem Nanoreactor Utilizing a Hierarchically Structured MOF", *Chem. Sci.,* **2016**, *7*, 6969-6973.
- **Lian, X.**; Feng, D.; Chen, Y.-P.; Liu. T.-F.; Wang, X; Zhou, H.–C., "The Preparation of An Ultrastable Mesoporous Cr(III)-MOF via Reductive Labilization", *Chem. Sci.*, **2015**, *6,* 7044-7048.